

Abstract

Title of Dissertation: γ -Ray Studies of Stellar Graveyards:
Fermi-LAT Observations of Supernova Remnants
and Spatially Extended Emission

Jamie Michael Cohen, Doctor of Philosophy, 2016

Dissertation directed by: Doctor Elizabeth Hays
Astroparticle Physics Laboratory, Code 661
NASA Goddard Space Flight Center

Professor M. Coleman Miller
Department of Astronomy
University of Maryland

When a massive star explodes as a supernova remnant it injects a huge amount of energy into its surroundings. The resultant expanding blast-wave is known as a supernova remnant. The shock created by the aftermath of the explosion is believed to be the primary accelerator of cosmic rays in our Galaxy. These supernova remnants are observable across the electro-magnetic spectrum. In 2008 the Fermi Gamma-Ray Space Telescope was launched into orbit and with its unprecedented gamma-ray resolution, has opened up a new window on the gamma-ray sky. In this thesis, we present new work using data from the primary instrument on the Fermi observatory, the Large Area Telescope (LAT), to study the population of supernova remnants observable by the LAT, with a focus on searching for spatially extended emission from these remnants of supernova explosions as a means for shedding light on the acceleration processes and gamma-ray emission mechanisms acting therein.

γ -Ray Studies of Stellar Graveyards:
Fermi-LAT Observations of Supernova Remnants
and Spatially Extended Emission

by

Jamie Michael Cohen

Dissertation submitted to the Faculty of the Graduate School of the
University of Maryland at College Park in partial fulfillment
of the requirements for the degree of
Doctor of Philosophy
2016

Advisory Committee:

Doctor Elizabeth Hays, Advisor
Professor M. Coleman Miller, Chair/Advisor
Professor Christopher S. Reynolds
Professor Derek C. Richardson
Professor Jordan Goodman, Dean's Representative

© Jamie Michael Cohen 2016

Preface

This thesis consists of 8 chapters including an introduction, conclusion and three background chapters on supernova remnants, γ -ray emission theory and detection methods, and a description of the relevant aspects of the *Fermi* Gamma Ray Space Telescope.

Chapters 5 and 6 are, respectively, taken in part from “The First *Fermi*-LAT Supernova Remnant Catalog” and “2FHL: The Second Catalog of Hard Fermi-LAT Sources”, both published in *The Astrophysical Journal Supplement* in 2016. Both papers are large, catalog studies involving the entire LAT collaboration. The parts of those papers included in this dissertation are the those in which I directly contributed to via analysis, writing, discussion. The text in Chapters 5 and 6 also expands on the work I did for those papers, and provides further detail on analysis not included in the papers.

Chapter 7 is the contents of a paper currently in preparation. The title of this paper is to be “*Fermi*-LAT Observations of Extended Gamma-Ray Emission in the Direction of SNR G150.3+4.5” (Cohen et al. 2016). The paper is included in entirety in this thesis, including additional supplementary material not to be included in the journal article.

To Vanessa ♡

Acknowledgements

I think anyone who has been through grad school knows that one lone grad student a dissertation does not make. I'd like to start this thesis properly by thanking my advisor Liz Hays. I can't imagine going through and getting through this PhD. journey without her.

I'm grateful to Cole Miller for serving as the head

I'd also like to thank Chris Reynolds, Derek Richardson, thank my and for having faith in my abilities to do this

What else has Liz done to help me? everything

Also, we must be cosmically tied (pun for sure!) due to the timing of both of our kids She's taught me so many things about

I'm proud to be her first graduate student

There have been a lot of people along the way who helped set me on this path and steer

Contents

List of Tables	viii
List of Figures	ix
1 Dissertation Overview	2
2 Gamma-ray Astronomy	4
2.1 γ -ray Emission Mechanisms	4
2.1.1 Synchrotron Radiation	5
2.1.2 Non-Thermal bremsstrahlung	6
2.1.3 Inverse Compton Scattering	7
2.1.4 Neutral Pion Decay Emission	8
3 The <i>Fermi</i> Gamma-Ray Space Telescope and γ-ray Data Analysis	10
3.1 Introduction	10
3.2 The Large Area Telescope	11
3.3 LAT Performance	15
3.4 <i>Fermi</i> -LAT Data Analysis Method	22
4 Supernova Remnants: Observation and Theory	26
4.1 Identification and Classification of Supernova Remnants	26
4.2 Supernova Remnant Dynamics and Evolution	29
4.3 The Supernova Remnant Cosmic Ray Connection	31
4.4 Supernova Remnants at γ -ray Energies	36
5 An Automated Method for LAT Analysis of the Galactic Supernova Remnant Population	44
5.1 Introduction	44
5.2 The pointlike Maximum-Likelihood Package and addSrcs	45
5.3 Galactic Supernova Remnants	51
5.4 Analysis Methods	51
5.5 Data Selection	52

5.6	Input Source Model Construction	54
5.7	Comparison of Source Models with 2FGL	61
5.8	Detection Method	65
5.8.1	Localization, Extension, and Spectral Curvature	69
5.8.2	Fluxes and Upper Limits	72
5.9	Catalog Results	72
5.10	GeV Supernova Remnants in a Multiwavelength Context: Discussion Summary	73
5.11	Conclusions	82
6	Extended Source Detection above 50 GeV: The 2FHL Catalog	86
6.1	Introduction	86
6.2	Analysis	88
6.2.1	Data Selection	88
6.2.2	Source Detection	88
6.3	Search for Spatially-Extended Sources	91
6.3.1	Extended Sources Previously Detected by the LAT	92
6.3.2	Newly Detected Extended Sources	93
6.4	The 2FHL Catalog	95
6.4.1	General Characteristics of 2FHL Sources	97
6.4.2	The 2FHL Galactic Source Population	98
6.4.3	Comparison with the H.E.S.S. Galactic Plane Survey	102
6.4.4	Extended Source Results	104
6.5	Summary	108
7	Fermi-LAT Observations of Extended Gamma-Ray Emission in the Direction of SNR G150.3+4.5.	112
7.1	Introduction	112
7.2	<i>Fermi</i> -LAT Observations and Analysis	114
7.2.1	Data Set and Reduction	114
7.2.2	Morphological Analysis	116
7.2.3	Spectral Analysis	120
7.3	Multiwavelength Observations and Analysis	120
7.3.1	HI Observations and Distance Estimate	120
7.3.2	X-ray Observations	122
7.4	Discussion and Results	123
7.4.1	G150: Supernova Remnant or Pulsar Wind Nebula?	123
7.4.2	G150.3+4.5 in a Supernova Remnant Context	125
7.4.3	Nonthermal Modeling	126
7.5	Conclusions	127

List of Symbols and Acronyms	135
Bibliography	138

List of Tables

5.1	Distances to SNRs	80
5.1	Distances to SNRs	83
6.1	2FHL extended sources previously detected by the <i>Fermi</i> -LAT	109
6.2	New 2FHL extended sources	109

List of Figures

3.1	<i>Fermi</i> launch images.	12
3.2	Top: Probability of photon conversion to $e^- e^+$ pair. Bottom: Photon cross section versus energy	13
3.3	LAT tower schematic	15
3.4	Diagram of the three primary LAT subsystems	16
3.5	LAT P8R2_SOURCE_V6 angular resolution	17
3.6	LAT P8R2_SOURCE_V6 effective area	18
3.7	LAT P8R2_SOURCE_V6 energy resolution	19
3.8	LAT 10 year, P8R2_SOURCE_V6 integral-flux sensitivity map	20
3.9	LAT 10 year, P8R2_SOURCE_V6 differential-flux sensitivity for four locations on the sky	21
4.1	Historical Crab nebula drawings	27
4.2	CR spectrum as measured at Earth	33
4.3	Third EGRET catalog all-sky map	36
4.4	<i>Fermi</i> -LAT counts maps from 10-100 GeV of the region around SNR W28	40
4.5	TS map of SNR RX J1713.7-39.46	41
4.6	γ -ray SEDs of SNRs W44 and IC443 obtained with the LAT	43
5.1	Histogram of the number of significant sources remaining in each of the 8 test ROI for iterations in which $\Delta(\log \mathcal{L}) < 8$	59
5.2	SNR Gamma Cygni flux, index, and extension evolution for successive <code>addSrcs</code> iterations	60
5.3	1-100GeV residual TS map for SNR W44 before running <code>addSrcs</code> and with 2FGL sources removed from the inner 3° radius.	62
5.4	1-100GeV residual TS map for SNR W44 after <code>addSrcs</code> has completed.	63
5.5	Comparison of the number of 2FGL sources with the number of newly added input model sources.	64
5.6	Same as Figure 5.5, including only input model sources lying within 0.2° of a 2FGL source.	66
5.7	Distribution of SNR radio diameters from Green's catalog	67

5.8	Radio diameter of Green’s catalog SNRs plotted against the fitted GeV diameter	74
5.9	Comparison of γ -ray and radio spectral flux densities for all SNRs and candidates.	75
5.10	Comparison of radio spectral index, α , and GeV photon index, Γ	76
5.11	GeV index compared to published index measurements from IACTs.	79
5.12	Age versus GeV spectral index	81
5.13	$1 - 100$ GeV luminosity vs. D^2 for SNRs with distance measurement.	84
6.1	Adaptively smoothed count map in the 50 GeV–2 TeV band	89
6.2	Sky map showing 2FHL source positions and classifications	96
6.3	Distribution of the spectral indices and highest photon energy	99
6.4	Adaptively smoothed count maps showing the whole Galactic plane .	100
6.5	Spectral energy distributions of four Galactic sources	105
6.6	Residual TS maps for the five new extended 2FHL sources.	111
7.1	Smoothed background subtracted residual counts map above 1 GeV for G150.3+4.5	117
7.2	G150.3+4.5 background subtracted residual TS map above 1 GeV .	129
7.3	G150.3+4.5 radially integrated counts map	130
7.4	SED of G150.3+4.5 and 3FGL J0426.7+5437	131
7.5	HI spectrum in the direction of G150.3+4.5	132
7.6	SEDS for several LAT observed SNRs	132
7.7	Luminosity versus squared diameter for several LAT SNRs.	133
7.8	Non-thermal emission model for G150.3+4.5	134

“Once there was a boy, and the boy loved stars very much.”

– Oliver Jeffers, from *How to Catch a Star*

Chapter 1

Dissertation Overview

We begin Chapter 2 of this dissertation with a brief discussion of the history of γ -ray astronomy, followed by a description of the mechanisms which lead to astrophysical γ -rays, and the sources that produce them. We conclude with a history of γ -ray observations leading up to those by the current space-borne MeV to TeV γ -ray observatory, the *Fermi* Gamma-Ray Space Telescope (hereafter, *Fermi*).

In Chapter 3, we present the *Fermi* telescope's design and primary instrument, the Large Area Telescope (LAT). We then describe the LAT's performance and capabilities.

Chapter 4 is a discussion of the astrophysical theory of supernova remnants (SNRs), connection between SNRs and cosmic rays (CRs), as well as the historical and current state of SNR observations. We conclude with a discussion of the present state of γ -ray studies of SNRs.

In Chapter 5, we present new work (published as Acero et al. (2016)) on a systematic study of the population of radio SNRs emitting GeV γ -rays, as detected by the LAT. We also present a new tool and analysis method, initially developed for this study and extended for general LAT analysis.

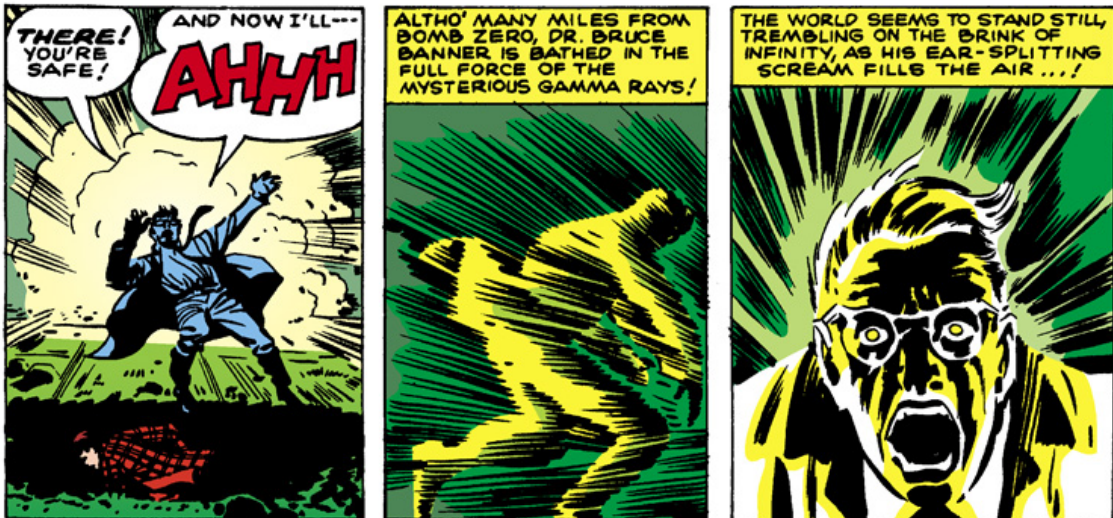
Chapter 6 is a presentation of the work published as Ackermann et al. (2016).

We applied this new analysis tool to study the all-sky population of hard Galactic γ -ray sources, from an energy of 50 GeV to 2 TeV, with a focus on detection of spatially extended sources.

In Chapter 7, we present a new study, in preparation for publication, where we performed an in-depth follow-up analysis of one of the newly discovered spatially-extended sources detected in γ -rays for the first time via our analysis in Chapter 6.

Chapter 2

Gamma-ray Astronomy



2.1 γ -ray Emission Mechanisms

The story of γ -rays from astrophysical objects is a tale of the most extreme, energetic, and violent environments in our universe. γ -rays are the highest named energy of light, starting from about an MeV and extending up, with the highest energy γ -rays detected being hundreds of TeV. Aside from the nuclear fission, γ -rays are produced solely by charged particles being accelerated to GeV and TeV

energies and interacting with a target particle, be it other matter or photon fields. Below we summarize the various non-thermal emission mechanisms giving rise to γ -rays, namely, inverse Compton (IC) radiation, non-thermal bremsstrahlung (both of an accelerated electron, or leptonic, origin), and neutral pion decay emission (of an accelerated proton, or hadronic origin). We also described the synchrotron radiation process. While not typically observed up to γ -ray energies (with synchrotron emission from the Crab nebula being an exception Abdo et al. (2010b), with the tail of the emission extending to hundreds of MeV), synchrotron photons plays a significant role in understanding IC γ -ray emission since the processes both arise from a shared, underlying electron population. Furthermore, observations of synchrotron emission at radio and X-ray energies is vital in constraining a source's underlying charged particle population and the resultant γ -ray source spectra. We follow Houck & Allen (2006) for many of the photon emissivities given below.

2.1.1 Synchrotron Radiation

When a relativistic electron moves in a magnetic field, it experiences a force perpendicular to its velocity which causes the electron to accelerate and travel in a helical path around the magnetic field lines. This acceleration results in radiation of photons, referred to as synchrotron radiation Blumenthal & Gould (1970); Longair (2011); Pacholczyk (1970); Rybicki & Lightman (1986). The total power emitted at frequency ν from a relativistic electron (Lorentz factor, $\gamma \gg 1$) spiraling in a magnetic field, B , is given as:

$$P_{\text{emitted}}(\nu) = \frac{\sqrt{3}q^3B \sin \alpha}{m_e c^2} F(\nu/\nu_c) \quad (2.1)$$

where q is the electron's charge, m_e the electron's rest mass, c the speed of light, α the angle between the magnetic field vector and the electron's velocity vector (the

pitch angle), and the critical frequency, the frequency at which most of the power is radiated is given as:

$$\nu_c = \frac{3qB\gamma^2}{4\pi m_e c} \sin \alpha \equiv \nu_0 \gamma^2 \sin \alpha \quad (2.2)$$

and F , called the first synchrotron function, is an integral over an irregular modified Bessel function (see Rybicki & Lightman (1986)). We note that the power emitted is inversely proportional to the mass, which explains the insignificance of proton synchrotron radiation, where the rest mass of the proton is ~ 2000 times greater than that of the electron.

For an isotropic distribution of electrons we define $N(p, \alpha)$ as the number of electrons per unit solid angle and momentum with momentum p and pitch angle α . Houck & Allen (2006) show that the differential photon-emissivity spectrum (i.e. number of radiated photons per unit time per unit energy) is:

$$\frac{dn}{d\omega dt} = \frac{\sqrt{3}q^3 B}{hm_e c^2 \nu} \int N(p) R\left(\frac{\omega}{\omega_0 \gamma^2}\right) dp \quad (2.3)$$

with ω being the radiated photon energy, $N(p) = 4\pi N(p, \alpha)$ for an isotropic pitch-angle distribution, and

$$R(x) \equiv \frac{1}{2} \int_0^\pi \sin^2 \alpha F\left(\frac{x}{\sin \alpha}\right) d\alpha \quad (2.4)$$

2.1.2 Non-Thermal bremsstrahlung

Bremsstrahlung radiation occurs when charged particles (electron-electron or electron-ion in this case) pass near each other, causing the primary charge to decelerate, and emit a photon. For a differential spectrum, $N_e(p)$, corresponding to the accelerated electrons, the total emissivity is given as the sum of the electron-electron and

electron-ion bremsstrahlung. The combined differential photon-emissivity spectrum can be given as:

$$\frac{dn}{d\omega dt} = n_e \int N_e(p) v_e \frac{d\sigma_{ee}}{d\omega} dp + n_Z \int N_e(p) v_e \frac{d\sigma_{eZ}}{d\omega} dp \quad (2.5)$$

where $d\sigma_{eZ}/d\omega$ and $d\sigma_{ee}/d\omega$ are the differential interaction cross sections for each interaction (Haug 1975; Koch & Motz 1959), n_e and n_Z are the stationary electron and ion densities, and v_e is the electron velocity.

2.1.3 Inverse Compton Scattering

IC scattering refers to the process by which a high-energy electron collides with a lower-energy photon transferring energy and “upscattering” the photon to higher energies (Blumenthal & Gould 1970). The dominant seed photon field available for upscattering by a population of electrons is that of the Cosmic Microwave Background (CMB), with a temperature $T \approx 2.73$ K. Other photon fields that may be relevant are far infrared (FIR) dust emission ($T \approx 30$ K), and near infrared (NIR) stellar-light ($T \approx 3000$ K). For a thermal photon-field of number density $n(\omega_i)$, with ω_i being the incident and photon energy,

$$n(\omega_i) = \frac{1}{\pi^2 \lambda^3} \frac{\omega_i^2}{e^{\omega_i/\Theta} - 1} \quad (2.6)$$

where $\Theta = kT/(m_e c^2)$, and the Compton wavelength of the electron is $\lambda = \hbar/(m_e c)$. For a momentum distribution of relativistic electrons, $N_e(p)$, embedded in an isotropic photon-field of number density $n(\omega_i)$, the single-photon differential photon-emissivity spectrum, is given by:

$$\frac{dn}{d\omega dt} = c \int n(\omega_i) d\omega_i \int_{p_{min}}^{\infty} N_e(p) \sigma_{KN}(\gamma, \omega_i, \omega) dp \quad (2.7)$$

with ω as the upscattered photon energy, ($\omega \equiv h\nu/(m_e c^2)$), and σ_{KN} is the Klein-Nishina scattering cross section:

$$\sigma_{KN}(\gamma, \omega_i, \omega) = \frac{2\pi r_0^2}{\omega_i \gamma^2} \left[1 + q - 2q^2 + 2q \ln q + \frac{\Gamma^2 q^2 (1 - q)}{2(1 + \Gamma q)} \right] \quad (2.8)$$

and,

$$q \equiv \frac{\omega}{4\omega_i \gamma (\gamma - \omega)} \quad (2.9)$$

for $\Gamma \equiv 4\omega_i \gamma$, and the classical electron radius, $r_0 = e^2/(mc^2)$

2.1.4 Neutral Pion Decay Emission

When high-energy protons and ions collide with interstellar material, one of the products of the collision is a neutral pion. The neutral pion subsequently (and expediently; within 10^{-16} s) decays into two γ -ray photons, each of rest energy $\omega_0 = (m_\pi c^2)/2 \approx 67.5$ MeV. For a differential proton distribution $N_p(p)$, the differential photon distribution is given by:

$$\frac{dn}{d\omega dt} = n_p \int v_p N_p(p) \frac{d\sigma(p_\pi, p)}{dp} dp \quad (2.10)$$

where n_p is the density of the target protons, $d\sigma(p_\pi, p)/dp$ the differential cross section for neutral pion production for proton collisions, and v_p the non-thermal proton velocity (Aharonian & Atoyan 2000; Dermer 1986; Hillier 1984). The peak of the distribution occurs at ≈ 67.5 MeV, however the peak is broadened due to Doppler shifting of the momentum distribution of the high-energy protons. This feature shows a bilateral symmetry about the peak energy in a photon spectrum representation, but in a νF_ν representation, it appears as a hardening of the spectrum at a few hundred MeV Dermer et al. (2013); Stecker (1971). This characteristic pion-decay feature is colloquially referred to as the “pion-bump”, and is a vital instrument

in distinguishing the proton-emitting population from the often-overlapping IC and bremsstrahlung spectrum produced at γ -rays.

Chapter 3

The *Fermi* Gamma-Ray Space Telescope and γ -ray Data Analysis

3.1 Introduction

The *Fermi* Gamma-Ray Space Telescope (*Fermi* hereafter), successor to the Energetic Gamma-Ray Experiment Telescope (EGRET) instrument on the Compton Gamma-Ray Observatory (CGRO), was successfully launched into orbit around Earth on June, 11 2008. *Fermi* consists of two instruments, the LAT and the Gamma-Ray Burst Monitor (GBM). The LAT, which is the primary instrument on *Fermi*, is a pair conversion telescope designed to detect photons from 20 MeV to greater than 1 TeV Ackermann et al. (2012c, 2016); Atwood et al. (2009) Its standard mode of operation is a sky-survey mode in which it observes the entire sky every 3 hours. The secondary instrument aboard *Fermi*, the GBM, was designed to detect γ -ray bursts in a waveband overlapping that of the LAT yet complementary in that its energy extends considerably lower. Combined the LAT and GBM comprise a formidable observatory, spanning more than 8 decades in energy, and it is

currently the only instrument performing all-sky observation in this broad energy range.

3.2 The Large Area Telescope

Due the nature of interaction between γ -rays and matter, photons of γ -ray energies cannot be reflected or refracted in the same way as lower energy light can be, which restricts the design possibilities of a γ -ray telescope. Because of this limitation, *Fermi* uses the photon pair-production phenomenon to detect γ -ray photons. Photon pair production refers to the mechanism by which a photon with sufficient energy (at least twice the rest mass of an electron) can convert to an electron/positron pair. The conversion from photon to antimatter pair can only occur in the presence of a nucleus whose Coulomb field can absorb and thus conserve the momentum of the photon. Figure 3.2 top shows the probability of photon conversion for given energies, demonstrating how higher Z (and thus stronger field) nuclei, are more conducive to conversion by providing a larger interaction cross section. Figure 3.2 bottom plots the interaction cross section versus photon energy. Above 10 MeV, photon pair production (κ_{nuc}) is the clearly dominant photon interaction process Beringer et al. (2012).

The LAT instrument on board *Fermi* is composed of three subsystems, all designed to take advantage of the pair production mechanism. First and foremost, is the tracker (TKR). The LAT's TKR is a module consisting of 18 x-y paired silicon strip detectors that measure the trajectories of the pair-produced charged particles. The silicon strips are interleaved with a tungsten foil to promote γ -rays passing through the material to convert to $e^- e^+$ pairs. The LAT is made up of 16 towers (arranged in a 4x4 grid), with each tower containing the 18 interlaced silicon,



Figure 3.1: Top left: *Fermi* being loaded on to a Delta II 7920-H rocket after arriving at Cape Canaveral. Top right: Delta II rocket at Space Launch Complex 17B with *Fermi* on board. Lower Left: Dr. Elizabeth Hays at Cape Canaveral marveling at the majestic launch of the *Fermi* observatory. Lower right: *Fermi* was launched into a 550 km, low Earth orbit, on June 11 2008, at 16:05 UTC. Images courtesy of NASA and Seth Diegel.

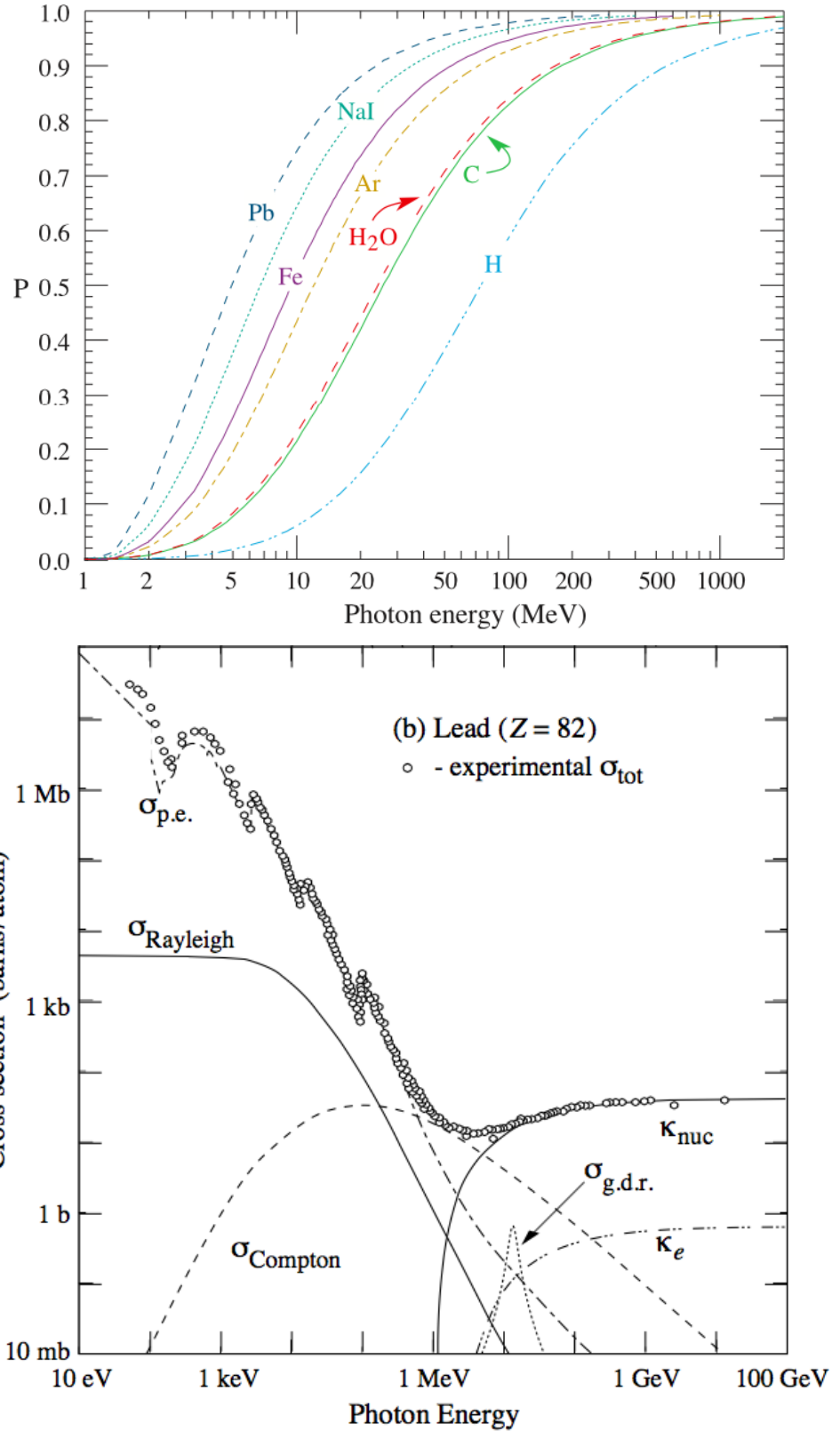


Figure 3.2: Top: Probability that a photon interacting with various nuclei will result in an $e^- e^+$ pair as a function of energy. Bottom: Photon cross section versus energy for various photon-matter interaction channels. Both figures originally from Beringer et al. (2012) as Figure 30.17 and 30.15.

tungsten planes. The top 12 layers of the TKR comprise the "front section" and are made of 3% radiation length tungsten. The next 4 layers constitute the "back section" of the TKR and are made of thicker, 18% radiation length tungsten foil. The final two TKR layers contain no tungsten and are present as a requirement of the TKR trigger which requires at least three hits in adjacent layers to trigger Ackermann et al. (2012c). The front section of the TKR was designed to minimize the separation between tungsten and silicon (i.e. the point of conversion and subsequent detection) minimizing multiple scattering effects therein, and thus optimizing the point spread function (PSF) for events converted in this section. The 6-times-thicker back layers were designed to further promote conversion, maximizing the effective area of the LAT, yet sacrificing resolution for events converting in this layer. Figure 3.3, shows a diagram of a single tower with TKR components included.

The next subsystem of the LAT is the Calorimeter (CAL). The CAL (located at the bottom of each of the 16 towers as in Figure 3.3) is comprised of 96 CsI scintillation crystals, arranged in 8 layers of 12 logs. This construction allows the CAL to **1.** measure the energy deposition of the shower of particles resulting from the incident photon's pair-produced $e^- e^+$ pair, and **2.** to perform 3D imaging of the shower, which can serve as a measurement of shower energy leakage.

The final vital component of the LAT is the anti-coincidence detector (ACD). The role of the ACD is to reject background charged particles that enter the LAT to avoid misclassifying them as photons. The design of the ACD was informed by lessons learned from the LAT's predecessor, the EGRET instrument on CGRO (Moiseev et al. 2005). In the CAL the electromagnetic shower generated by the incident photon produces secondary particles as well as X-rays. These X-rays can Compton scatter the charged particles out through the TKR and ACD (referred to as "backsplash") creating false vetoes. This backsplash was present in EGRET and

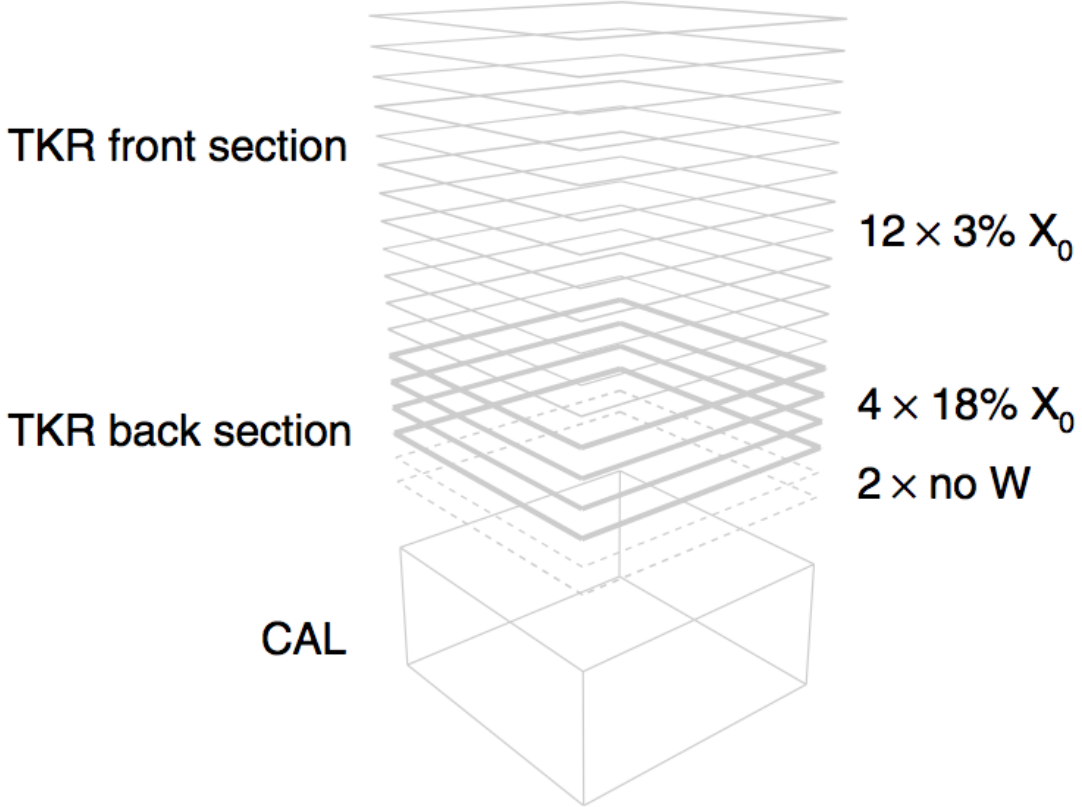


Figure 3.3: LAT tower schematic showing the different TKR layers and ending with the CAL on the bottom of the tower. Taken from Ackermann et al. (2012c)

reduced the efficiency of the instrument above 10 GeV Atwood et al. (2009). To overcome the backsplash effect, the LAT uses a segmented rather than monolithic layer for the ACD, made up of 89 scintillating tiles surrounding the towers (as in Figure 3.4).

3.3 LAT Performance

The LAT performance is dictated by the telescopes hardware and software designs (e.g. event reconstruction methods, background and event classifications). The parameterizations of the performance are referred to as the instrument response functions (IRFs). The LAT IRFs are factorized into three terms:

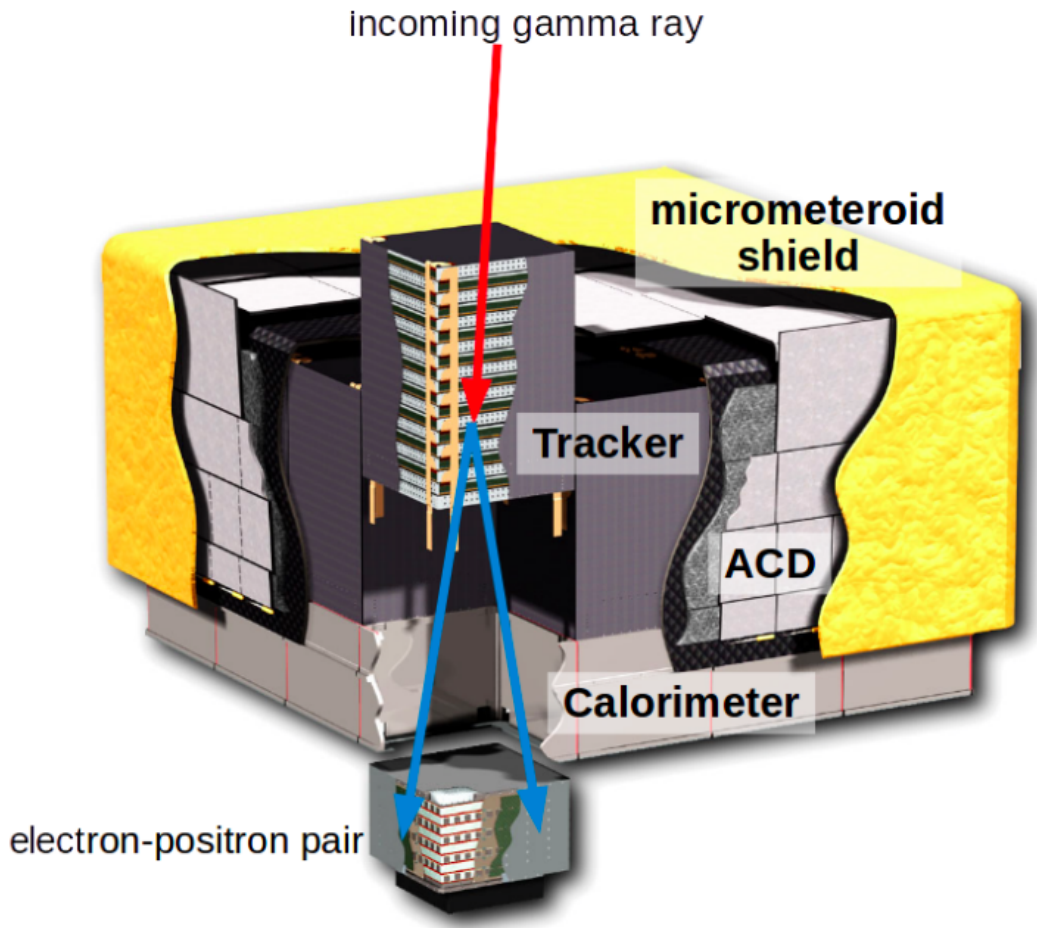


Figure 3.4: Diagram of the LAT subsystems demonstrating how an incident γ -ray can enter through the top layer of the ACD, convert to a $e^- e^+$ pair in a layer of the TKR, and finally deposit its energy in the CAL.

1. **PSF, $P(\hat{v}'; E, \hat{v})$:** Represents the angular resolution of the LAT. It is the probability density for reconstructing an incident γ -ray with position \hat{v}' if the true position is \hat{v} for given energy E . The PSF is strongly energy dependent. At low energies, this dependence is dominated by multiple scattering in the TKR causing the PSF to broaden, and at higher energies (above a few GeV) it is dominated by the strip pitch, or the distance between adjacent silicon strip centers, which limits how fine the PSF can be at high energies.

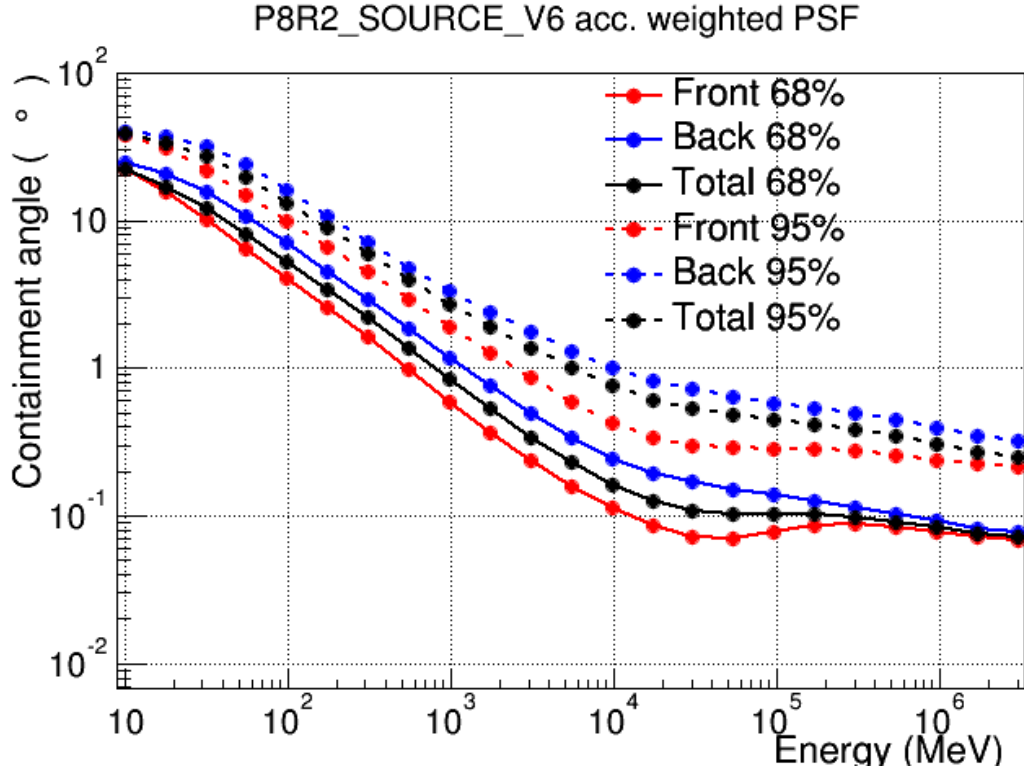


Figure 3.5: LAT angular resolution for 68% and 95% containment radius and front and back converting events as a function of energy for the P8R2_SOURCE_V6 event classification. Figure from https://www.slac.stanford.edu/exp/glast/groups/canda/lat_Performance.htm

2. **Effective Area, $A_{\text{eff}}(E, \hat{v})$:** Represents the collecting area of the LAT. It is the product of the geometric cross section of the LAT and a dimensionless term that quantifies the efficiency of the LAT's event reconstruction. It has units of area.
3. **Energy Dispersion, $D(\hat{E}'; E, \hat{v})$:** Represents the energy resolution of the LAT. It is the probability density for reconstructing an incident γ -ray with energy \hat{E}' if the true energy is \hat{E} for given direction on the sky. Energy dispersion effects are often ignored in LAT analysis above a few hundred MeV as Ackermann et al. (2012c) showed that the effects of neglecting it are of the order of a few percent.

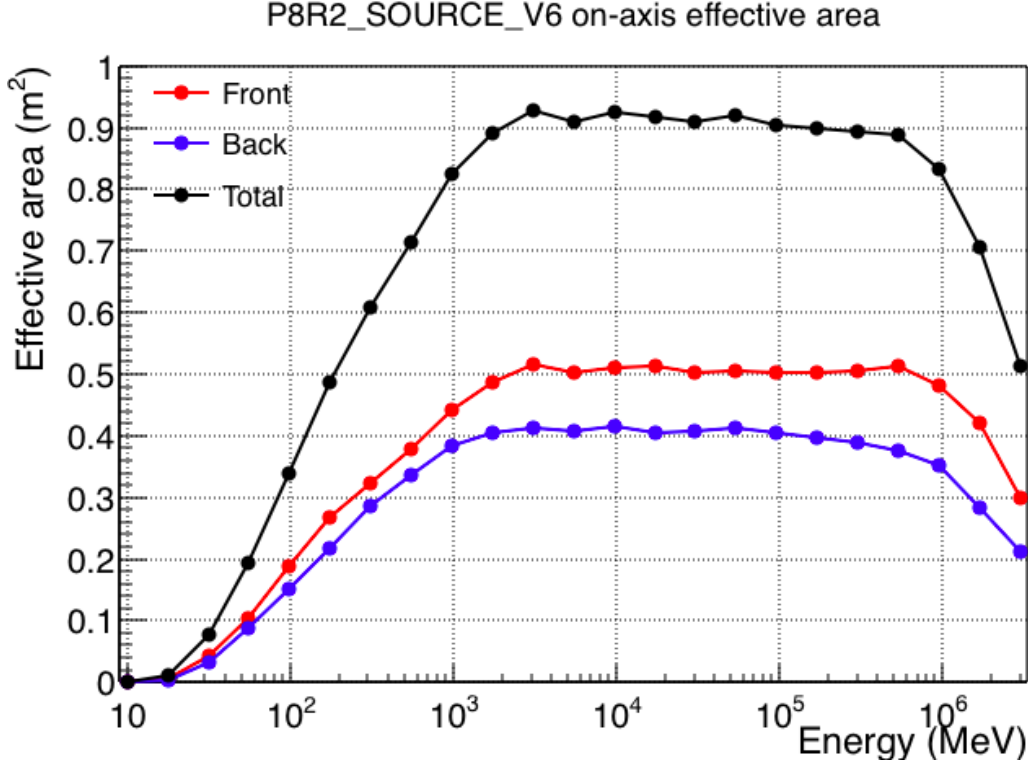


Figure 3.6: LAT effective area for front, back, and total converting events as a function of energy for the P8R2_SOURCE_V6 event classification. Figure from https://www.slac.stanford.edu/exp/glast/groups/canda/lat_Performance.htm.

In general, the LAT has a large effective area ($\sim 9500\text{cm}^2$ at a few GeV) (Figure 3.6), energy resolution of 5% (at 10 GeV) to 20% (at 100 MeV) (Figure 3.7), and a single-photon angular resolution ranging from $\sim 3.2^\circ$ at 100 MeV to $\lesssim 0.16^\circ$ for $E > 10$ GeV (Figure 3.5). With its rocking mode observation strategy (35° north of the zenith axis for one orbit, and then south for the next) and its wide field of view (FoV) of 2.4 sr, the LAT attains a nearly uniform coverage of the sky within two orbits, or 3 hours. The culmination of the LAT's performance can be summed up as its capability to detect distinct sources on the sky. Figures 3.8 and 3.9 depict the LAT's threshold for detecting emission from a point source above the structured Galactic diffuse emission ???. Figure 3.8 demonstrates what level of emission the

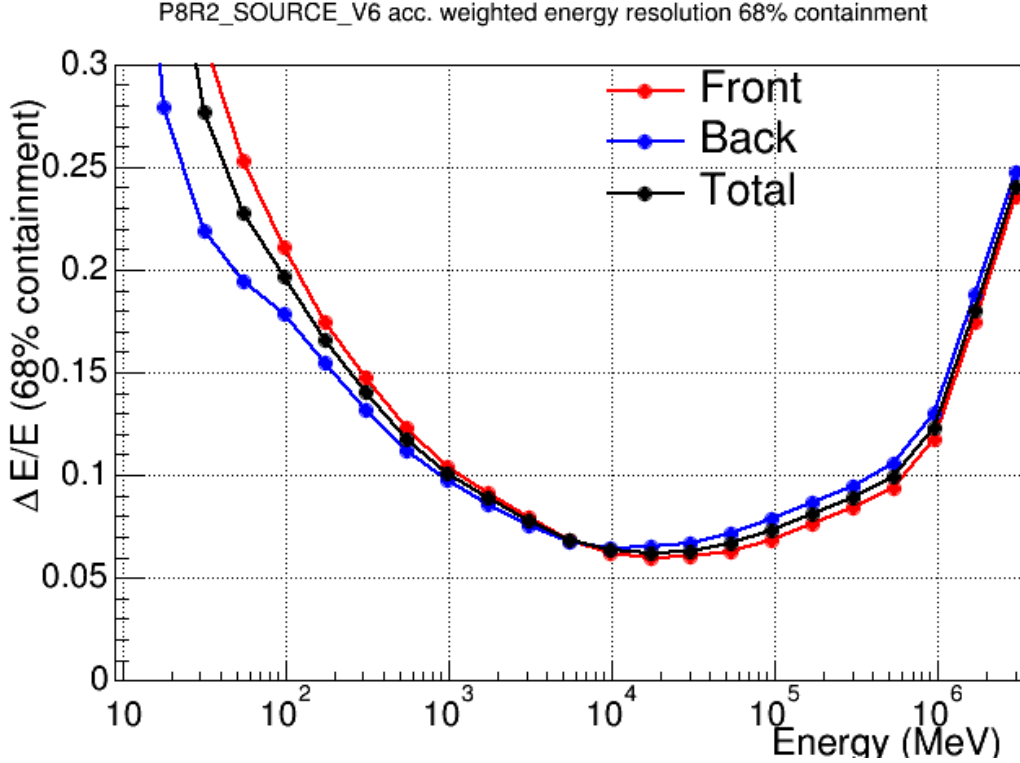


Figure 3.7: LAT energy resolution for front, back, and total converting events as a function of energy for the P8R2_SOURCE_V6 event classification. Figure from https://www.slac.stanford.edu/exp/glast/groups/canda/lat_Performance.htm.

LAT can detect when integrating over the majority of its energy range, and Figure 3.9 shows what the source detection threshold is for detecting sources in individual energy bins and at four locations on the sky. See 4.4 for a comparison of the LAT's capabilities with that of EGRET.

For a given γ -ray source model $S(E, \hat{p})$, i.e. the number of photons per unit time, energy, and solid angle at a given time, energy, and position on the sky, where \hat{p} is the direction on the sky, we can convolve the source model (times the effective area) with the dispersion components (PSF and energy dispersion) to obtain the predicted differential source counts (in counts per unit energy/time/solid angle) by integrating over the energy and time range of interest and over the solid angle in

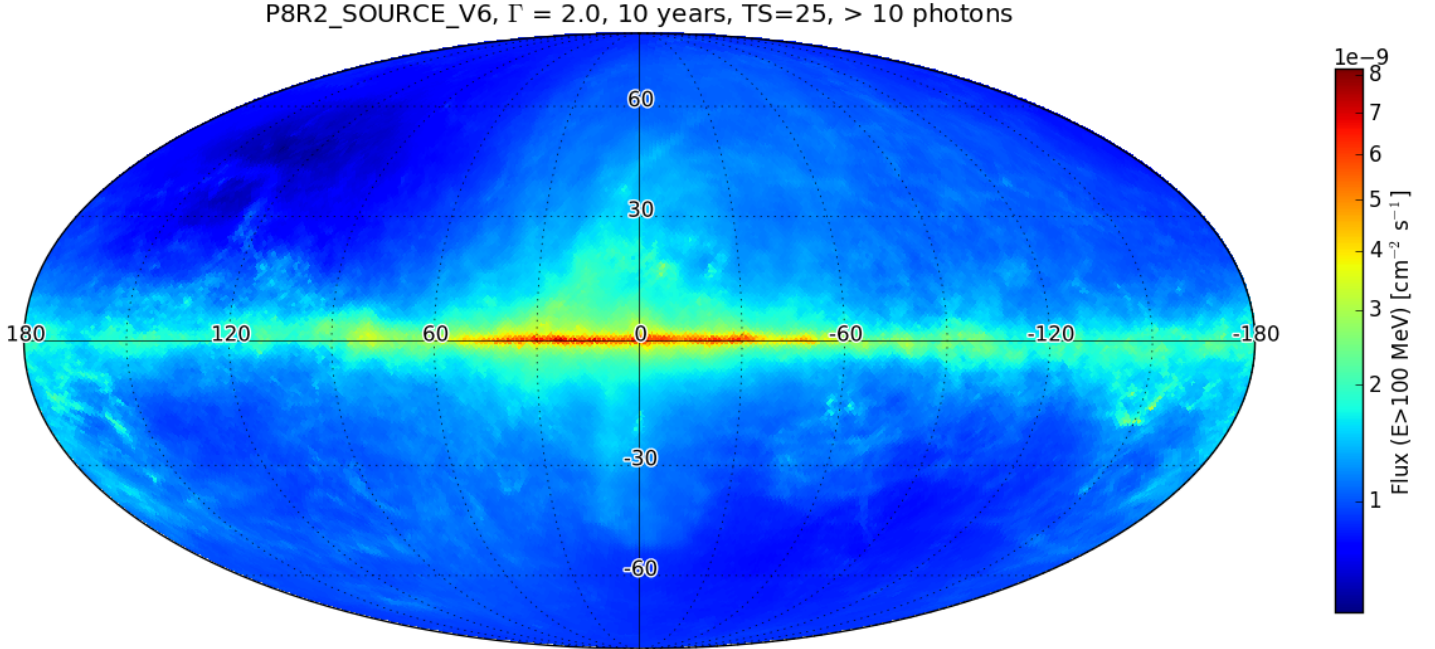


Figure 3.8: LAT 10 year, integral-flux sensitivity map for P8R2_SOURCE_V6 event classification. The all-sky map was created for energies above 100 MeV and for a point source (modeled as a power law (PL) of spectral index 2) to obtain a 5σ significance. Figure from https://www.slac.stanford.edu/exp/glast/groups/canda/lat_Performance.htm.

the LAT reference frame:

$$M(E', \hat{p}') = \int \int \int S(E, \hat{p}) A_{eff}(E, \hat{v}) \times \\ P(\hat{v}'(t, \hat{p}'); E, \hat{v}(t; \hat{p})) D(E'; E, \hat{v}(t; \hat{p})) dE d\Omega dt. \quad (3.1)$$

All the values discussed above are particular to the recent LAT event-level reconstruction update colloquially referred to as Pass 8 (Atwood et al. 2013b). Pass 8 consists of a series of improvements to the LAT's event selection process. The three primary areas of improvement are in the event reconstruction methods, background rejection, and Monte Carlo simulations of the detector using flight data. One improvement example involves the way in which the LAT reconstructs and tracks the path of an $e^- e^+$ pair back to an incident photon. Previously a track-by-track

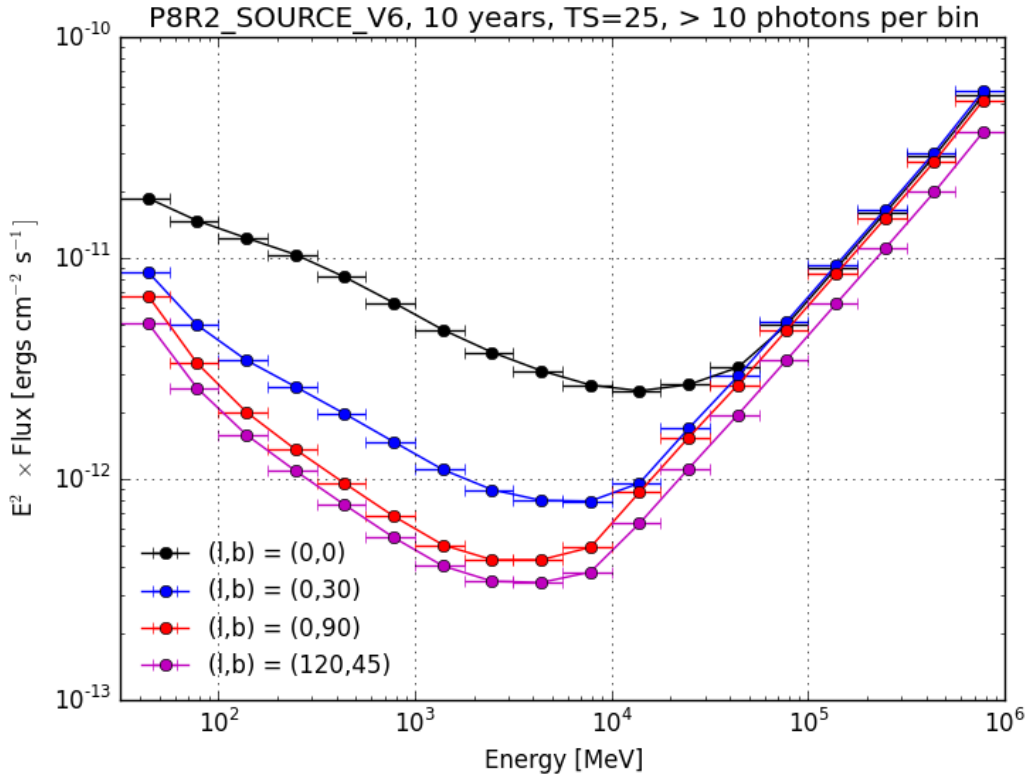


Figure 3.9: LAT 10 year, differential-flux sensitivity map for P8R2_SOURCE_V6 event classification. The all-sky map was created for energies above 100 MeV and for a point source (modeled as a PL of spectral index 2) to obtain a 5σ significance. Figure from https://www.slac.stanford.edu/exp/glast/groups/canda/lat_Performance.htm.

pattern recognition algorithm was used to find the two antimatter paths and combine them back to determine the vertex of conversion. The improved method uses a tree-based tracking method that considers conversion in the TKR as the start of an electromagnetic shower and attempts to model this process by grouping hits in the TKR into one or more “trees”. Similar event reconstruction methods have also been applied to the ACD and CAL.

The combined effects of the various upgrades result in an extension of the energy down to 30 MeV and up to 3 TeV (Bruel & Fermi-LAT Collaboration 2012, see Chapter 6 for applications), a 40% gain in point-source sensitivity, up to a $2\times$

increase in acceptance (defined as effective area integrated over solid angle) below 100 MeV and above 100 GeV, and a narrower PSF at high energies. Several new event classifications have also been developed (in addition to the previous front and back event types) to leverage the newfound Pass 8 LAT capabilities. Specifically, there are new event types that define the quality of event reconstruction for both the PSF and energy dispersion, by partitioning events into quartiles based on quality, allowing for an even finer grade energy and spatial resolution.

3.4 *Fermi*-LAT Data Analysis Method

The standard method for analyzing astrophysical data at other wavelengths (e.g. optical) is by performing aperture photometry. This consists of essentially counting the photons “on-source” in a extraction region and subtracting off the estimated background “off-source” in a neighboring region, where the background is typically assumed to be isotropic. Although not always simple, various source quantities can typically be derived from the data itself (e.g. intensity, extent if resolvable). The aperture photometry method is not feasible for analysis of *Fermi* data (as was the case for EGRET Mattox et al. (1996)) due to various complexities inherent to detecting γ -ray photons.

The first such issue is that because of the breadth of the LAT PSF, and wide energy range of the LAT, source confusion abounds and sources are not truly isolated from one another. The overlapping tails of the PSF would make analysis via aperture photometry particularly intractable at low energies (where the PSF rises steeply with decreasing energy, see Figure 3.5) and in the Galactic plane (with a high source density and strongly anisotropic diffuse emission ??). The second reason is the complex relationship between an individual source and the IRFs. Since *Fermi*

typically operates in a sky-survey mode, photons from an individual source need to accumulate over long integration times, and the orientation of the space craft with respect to the source of interest will vacillate over time. The response of the telescope is dependent on the orientation of the space craft, so it is non-trivial to determine source and background fluxes by simply counting photons.

To circumvent the issues described above, Cash (1979) applied the maximum likelihood method to astrophysical counting-experiments and parameter estimation of X-ray data. Mattox et al. (1996) then established a framework for analyzing EGRET γ -ray via the maximum likelihood method. The likelihood, \mathcal{L} , is defined as the probability of obtaining the data observed assuming a model of the sky. In the maximum likelihood framework, we want to estimate the model parameters by maximizing the likelihood and finding the parameters that best-fit the data. Since the LAT is a particle detector, and hence a photon counting experiment, the observed counts are distributed as a Poisson distribution with unknown mean. For large data sets it is more tractable to use a binned maximum likelihood analysis; binning in both position on the sky and energy. The binned maximum likelihood function for LAT is thus given as:

$$\mathcal{L} = \prod_i \frac{m_i^{n_j} e^{-m_i}}{n_i!} \quad (3.2)$$

Thus the likelihood is the product of the Poisson probabilities over all j positions and energies, where m_i is the expected counts in the i^{th} bin, and n_i is the observed counts in the i^{th} bin. It is often computationally easier to work with the log of the likelihood, so taking the log of 3.2 gives:

$$\log \mathcal{L} = - \sum_i m_i + \sum_i n_j \log m_j \quad (3.3)$$

where we have dropped the arbitrary constant $-\log n_i!$. The term $\sum_i m_j$ is the total expected counts in all bins. The model counts m_i are calculated by integrating the

differential source model (given by 3.1) over the i^{th} bin for all sources. The *Fermi* Science Tools were designed to perform the tasks involved in binning the sky in position and energy, calculating the convolution integral in 3.1, and computing the likelihood of 3.3 (implemented via `gtbin`, `gtsrcmaps`, and `gtlike` respectively).

The other way in which *Fermi* employs the maximum likelihood method is through the likelihood ratio test (LRT) to assess detection source significance and compare model hypotheses. The LRT is a statistical method to assess the goodness-of-fit of two different models. The likelihood is calculated for two models, one of which can be reduced to the other hypothesis under certain conditions. If the more complex model can be reduced to the simpler model (called the null hypothesis), we say the simpler hypothesis is nested within the more complex. In the LRT, the test statistic (TS) is defined as:

$$\text{TS} \equiv 2 \log(\mathcal{L}(H_1) / \mathcal{L}(H_0)), \quad (3.4)$$

with H_1 being the more complex hypothesis and H_0 the null. Mattox et al. (1996) detail how by Wilks' theorem, the TS for detection of a point source (with the null hypothesis being that with no source present, or 0 flux) should be distributed as a chi-squared distribution in the null hypothesis for an increasing sample size, which for photon counting experiments, is the number of events relevant to the parameter being estimated. Specifically,

$$\text{PDF(TS)} = 1/2 \chi_1^2, \quad (3.5)$$

where PDF(TS) is the probability distribution function for obtaining a specific value of TS and χ_1^2 is the chi-squared distribution for one degrees of freedom. The factor of 1/2 arises from the fact that the flux of a source is not permitted to be zero, and since negative and positive fluctuations in a parameter's value contribute equally

to the TS, half of the distribution is lost with the positive flux restriction. The significance of detection is oft quoted as $\sigma \approx \sqrt{TS}$, which is strictly valid only for χ_1^2 . More generally, when comparing the likelihood of two models with n degrees of freedom between them, equation 3.5 applies, but using χ_n^2 for n degrees of freedom versus one.

Chapter 4

Supernova Remnants: Observation and Theory

4.1 Identification and Classification of Supernova Remnants

When a massive star at the end stage of its evolution explodes as a supernova, it nearly instantaneously injects a massive amount of kinetic energy into the surrounding medium ($\sim 10^{51}$ erg). The supersonically expanding blast-wave, ejected stellar mass, and possible compact stellar remnant comprise an SNR. The first two identified SNRs (the Crab and Kepler's SNR) were initially observed as optical nebulosities found to be associated with historical supernovae (see Figure 4.1). It was not until the advent of the radio interferometer that a number of these nebulae were discovered and could thus be studied as a population. In fact, one of the first discrete radio objects to be detected was a remnant in the Cassiopeia constellation now known as Cassiopeia A (Ryle & Smith 1948).

One of the primary distinguishing features of the radio emission from SNRs was



Figure 4.1: Left: First depiction of the Crab nebula by William Parsons, the Third Earl of Rosse, based on his observations using a 36 inch telescope in 1844. The filamentary structure motivated him to dub it the Crab nebula. Right: Another depiction of the Crab nebula by William Parson and R. J. Mitchell based on observations with a 72 inch telescope in 1884. From J. Bevis, *Uranographia Britannica*, 1750

their distinctly non-thermal spectra (a PL with flux $S \propto \nu^\alpha$, where ν is frequency). The clearly non-thermal emission was first proposed to arise from synchrotron radiation (and hence is emitted by a population of relativistic electrons) by Kiepenheuer (1950) and Alfvén & Herlofson (1950), and then by Shklovskii (1953) who correctly associated the remnants with supernovae in the Galaxy. To this day, SNRs are still primarily identified through radio observations (although a number have been first detected in X-ray as well). A catalog of 294 radio-identified Galactic SNRs is maintained at <http://www.mrao.cam.ac.uk/surveys/snrs/> by Green (2014) (referred to as Green’s catalog) and a complementary high-energy catalog, summarizing the X-ray to γ -ray properties of Galactic SNRs, is upkeep by Ferrand & Safi-Harb (2012) at <http://www.physics.umanitoba.ca/snr/SNRcat>

While the non-thermal, radio synchrotron spectra of SNRs are used to identify remnants, their morphology is used to classify them. The classifications, based on

radio and X-ray observations are:

- **Shell-type** SNRs are characterized by a radio (and sometimes X-ray) limb-brightened shell or ring. The perimeter or the (possibly incomplete) shell corresponds to the expanding forward shock from the blast-wave and is composed of the ejecta from the initial explosion as well as mass from the surrounding medium swept-up by the blast-wave. They are typically associated with less-evolved, or dynamically young SNRs (see the following Chapter for details on SNR evolution). In Green (2014), 79% of the radio SNRs are classified as shell type.
- **Filled-center** SNRs or **plerions** are SNRs that show no clear shell structure but rather are centrally bright at radio, and sometimes X-ray, energies. The central synchrotron emission arises if the compact stellar remnant is a pulsar which can drive a pulsar wind nebula (PWN) Gaensler & Slane (2006). The PWN is generated by the rotational power of the spinning pulsar transferring its energy to a relativistic, magnetized wind of electrons and positrons that emit synchrotron radiation throughout the nebula. While the energy source of the shell-type SNR is deposited in the singular supernova event, the spin-down power of the pulsar is injected into the plerionic system over a much longer time span. 5% of radio SNRs are center-filled (Green 2014).
- **Composite** remnants are simply SNRs that display both a distinct shell-like structure as well as a center-filled, non-thermal synchrotron nebula.. Green (2014) classifies 12% of SNRs as being composite.
- **Mixed morphology** SNRs are ones that exhibit a non-thermal radio shell-like structure as well as centrally located thermal X-ray emission (Rho & Petre 1998). This is in contrast to the composite system which displays a non-

thermal emission nebula generated by a rotating neutron star. Some authors, including Green (2014), use mixed-morphology interchangeably with composite. The thermal X-ray emission is produced by swept-up and shock-heated material. These SNRs are often associated with more-evolved (or middle-aged) remnants that are interacting with surrounding, dense molecular material (as evidenced by shocked molecular lines and sometimes 1720 MHz OH masers).

The remaining few percent of SNRs not classified as one of the above are remnants that show a more complicated morphology, yet are still believed to be SNRs. In fact, with more sensitive, higher resolution telescopes, many shell-type SNRs only exhibit partially complete circular structures, and may show signs of blow-out (when part of the shell appears to expand faster in one direction than another) or elongated morphologies, all signs of not-purely spherical evolution of the blast-wave (which itself might not be spherically symmetric) in an inhomogeneous interstellar medium (ISM).

4.2 Supernova Remnant Dynamics and Evolution

The formation of an SNR begins as the supersonically traveling ejecta expands out and collides with the ISM forming a blast-wave. The standard model for the evolution of an SNR (first proposed by Woltjer (1972)) is divided into four phases.

1. **Free-Expansion Phase:** In this phase, (sometimes referred to as the ejecta-dominated phase), the forward shock of the blast-wave expands out into the ISM sweeping up mass as it expands. The ejecta mass is of the order of a few to 10's of M_{\odot} , while the shock speed is typically $\sim 10^3 - 10^4 \text{ km s}^{-1}$ for type Ia and core-collapse events respectively Reynolds (2008). The velocity of the shock remains essentially constant in this phase until the mass of the

swept-up material, equals that of the ejecta mass. At this point the swept-up mass starts to dynamically affect the expansion of the remnant, marking the end of the free-expansion phase.

2. **Sedov-Taylor (ST) Phase:** The ST phase (also referred to as the adiabatic expansion phase) begins when the swept-up mass M_{su} , is equivalent to the ejecta mass, M_{ej} . The radius of the SNR at the onset of the ST phase is given by:

$$R_{ST_0} = (3M_{ej}/4\pi\mu\rho_0)^{1/3} = 1.9(M_{ej}/n_0)^{1/3} pc, \quad (4.1)$$

for $\rho_0 = n_0 m_H$, the mass density of the swept up matter, where n_0 is the pre-shock particle density of the medium the SNR is expanding into (in units of cm^{-3}), $\mu \approx 1.4$ is the ISM's mean atomic weight and M_{ej} is in units of M_\odot . The ST phase is dominated by the thermal pressure of the shock-heated gas which is adiabatically expanding (conserving energy), yet the gas is still hot enough that radiative losses are relatively inefficient. Sedov (1959) and Taylor (1950a) developed a self-similar, analytic model for the evolution of the shock at this phase for an explosion that instantaneously injects energy at a point into a uniform density medium with no energy loss. The ST solution for the radius of a shock that evolves with time, t , for an explosion energy, E , is:

$$R_{ST} = \left(\zeta \frac{Et^2}{\rho_0} \right)^{1/5} = 0.314(E_{51}/n_0)^{1/5} t_y^{2/5} pc, \quad (4.2)$$

with the constant, $\zeta = 2.026$ corresponding to a monatomic, non-relativistic gas ($\gamma = 5/3$), E_{51} the energy of the explosion in units of 10^{51} erg, and t given in years. This phase typically lasts for a few 10^4 yr, with the radius of the SNR growing to 10's of pc. The ST phase ends when the temperature has decreased enough ($\approx 10^6 K$), through expansion and adiabatic cooling, that recombination can occur and atoms can cool radiatively.

- 3. Radiative Phase:** In the radiative phase, also known as the snowplow phase, the increased cooling causes the SNR shell to expand slower. Interior to the shock though, hot gas has not had time to cool and continues expanding adiabatically, exerting a pressure on the cooler, outer shell. The pressure of the hot interior pushes on the dense shell, “snowplowing” ambient mass from the ISM, which will coast out, conserving momentum as the interior cools.
- 4. Dispersion Phase:** Finally, the SNR diffuses and merges into the ISM with the temperature and shock velocity decreasing and becoming comparable to that of the ambient ISM.

While this general scheme for the evolution of an SNR in the ISM is sufficient for explaining general observational features of SNRs, more intricate models are required to explain details of individual SNRs. Various authors have since expanded on the dynamical evolution of SNRs by including information regarding the initial velocity/density structure of the ejecta, inhomogeneities of the material the SNR is expanding into, energy loss through escaping CRs, and the effects of magnetic fields on expansion (Chevalier 1974, 1982; Truelove & McKee 1999, and references in Vink (2012) which reviews various analytic SNR expansion models).

4.3 The Supernova Remnant Cosmic Ray Connection

As discussed in Chapter 4.2, the massive amount of energy released by a supernova explosion goes into the creation of a blast-wave that expands out, shocking and heating the region around the progenitor star. It is thought that the cataclysmic explosion is the prime energy source and generator of Galactic CRs (at least up to

the knee of the CR energy spectrum, see Figure 4.2). CRs are charged particles with energies ranging from about 1 MeV to 10^{21} eV, first discovered, and shown to be of extra-terrestrial origin by Hess (1912). CRs are a major source of energy in the ISM with an energy density, $\rho_{\text{CR}} \sim 1 \text{ eV cm}^{-3}$ (Blasi 2013; Hörandel 2008). CRs account for about 1/3 of the total energy density of the ISM and thus play a pivotal role in stoking chemical evolution and in driving Galactic evolution.

It was first proposed by Baade & Zwicky (1934) and then again, more quantitatively, by Ginzburg & Syrovatskii (1964) and Hayakawa (1969), that supernovae could be the source of CRs. At the time, this was based solely on energy requirements since there is a dearth of physical processes in the universe that can supply the appropriate energy to match the energy density in Galactic CRs. We can estimate the total power in CRs in the Galaxy as:

$$L_{\text{CR}} = \frac{V\rho_{\text{CR}}}{\tau} \sim 5 \times 10^{40} \text{ erg s}^{-1} \quad (4.3)$$

where the volume of the Galactic disk is, $V = \pi R^2 d \sim \pi(15 \text{ kpc})^2(200 \text{ pc})$ and $\tau \sim 6 \times 10^6$ yr is the residence time of CRs in the Galaxy determined from the boron to carbon ratio (Gaisser 1990). With the energy output of a single supernova event being $\sim 10^{51}$ erg, and a supernova rate in our Galaxy of $\sim 2\text{-}3$ per century, supernovae supply a total power of about $10^{42} \text{ erg s}^{-1}$, and we see that the energy density of CRs in the Galaxy can be explained if about 10% of the explosion energy goes into particle acceleration.

This energy argument is of course circumstantial, and a physical mechanism to explain the transfer of energy from explosion to shock, and shock to particles accelerated to very high energies is necessary. Fermi (1949) first proposed a mechanism by which charged particles can gain energy by being magnetically “reflected” back and forth by molecular clouds. In his initial formulation it seemed like it might

Energies and rates of the cosmic-ray particles

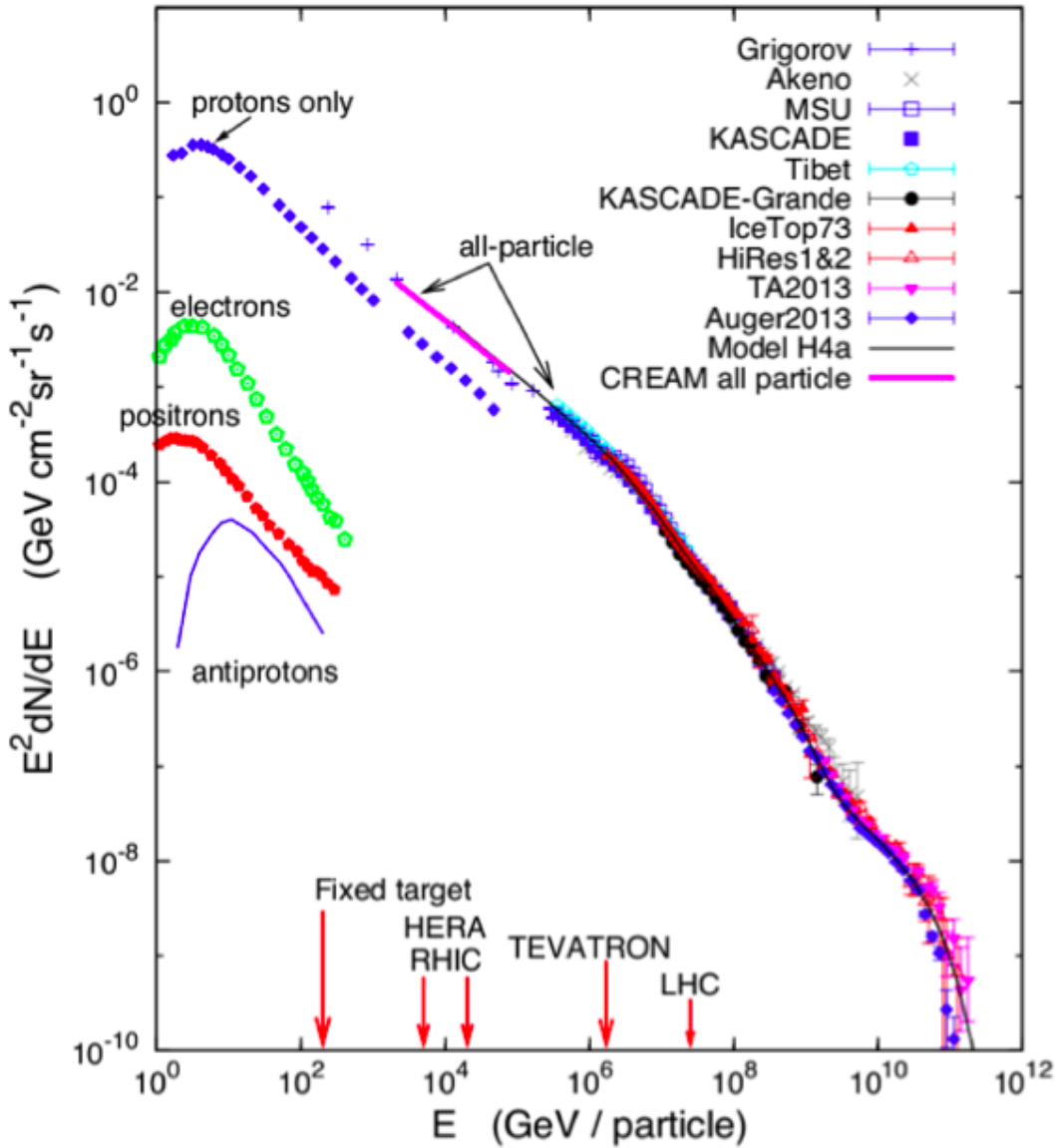


Figure 4.2: CR spectrum as measured at Earth. Protons are the dominant species accounting for $\sim 99\%$ of the detected particles. The electron-to-proton ratio at 10 GeV is $K_{ep} \approx 0.01$. The so-called “knee” of the CR energy spectrum occurs at $\sim 3 \times 10^{15}$ eV, where the PL spectral slope changes from -2.7 to -3.1 . Above the knee, the CRs are believed to be of an extra-galactic origin. Figure from Blasi (2013).

not be a viable mechanism to explain CRs since the effects of reflection by receding and approaching clouds would cancel out. Several authors (Bell 1978; Blandford

& Ostriker 1978, for example) noticed that in a strong shock there is a preferred frame (that of either the pre or post-shock scattering center) and particles crossing the shock will gain energy after every shock crossing as they are reflected multiple times by magnetic turbulence, or irregularities, up and down stream of the shock. This process is called first order Fermi acceleration or diffusive shock acceleration (DSA).

For the simplest test particle case (where the particle itself does not affect the shock or flow of plasma), DSA predicts a PL in the accelerated particle spectrum. For accelerated electrons with a PL energy distribution, $N(E) = KE^{-s}$ (with units of electrons per unit energy), the resulting synchrotron spectrum is governed by the compression ratio of the shock, $s = (r + 2)/(r - 1)$, where $r = 4$ for a specific heat ratio $\gamma = 5/3$. Thus, DSA predicts a PL index of 2 for the test particle case, which corresponds to a radio-synchrotron spectral index $\alpha = (1 - s)/2 = -0.5$ (Pacholczyk 1970, and Chapter 2.1). For detailed discussions of departure from the test-particle case (referred to as non-linear DSA, see Reynolds (2008),Malkov & Drury (2001) and Urošević (2014) for application to radio SNRs)

Observational evidence of particle acceleration at SNR shock fronts is non-trivial and of necessity indirect. Galactic magnetic fields deflect the paths of charged particles, so the CRs detected at Earth can not be traced back to their source of origin. Thankfully, there are several mechanisms that electrons and protons undergo (i.e. synchrotron radiation, non-thermal bremsstrahlung, IC, and pion-decay emission) that result in emission of photons, which can in turn be studied as a proxy for the CRs and followed back to the generating source (see Chapter 2.1 for details on these non-thermal emission mechanisms). The presence of radio synchrotron radiation implies that there is a population of electrons being accelerated at the shock-front of SNRs, but not to an energy approaching the knee in the CR energy

spectrum. The first “smoking-gun” evidence for electron acceleration to very-high energies was presented by Koyama et al. (1995) using X-ray observations from the ASCA telescope. Koyama et al. (1995) observed a featureless, non-thermal emission component in the shell of SN 1006, distinct from the thermal emission observed interior to the shell. This non-thermal radiation component was interpreted as synchrotron emission, and the inferred maximum energy of emitting electrons was \sim 100 TeV, clearly demonstrating that electrons can be accelerated to CR energies close to the knee of the CR spectrum by the shock front of an SNR. Furthermore, SNR observations of TeV γ -rays with similar morphologies to that in X-ray support the findings of Koyama et al. (1995) by revealing the IC radiation resulting from the synchrotron emitted photons up-scattering ambient light to TeV energies Aharonian et al. (2004); Tanimori et al. (1998).

Despite the fact that electrons can be accelerated to CR energies by SNR shock fronts, electrons only account for 1% of the total CRs observed at Earth (see Figure 4.2), so to definitively determine if the bulk of the CR energy density in the Galaxy can be explained by CR proton acceleration in SNRs, more direct-evidence of proton accelerations is necessary. While one can infer that if electrons are accelerated to ultra-relativistic energies by SNR shock-fronts, then protons should also be accelerated, direct evidence of proton acceleration is harder to come by. The primary energy-loss channel for protons is neutral pion-decay emission resulting from proton-proton interactions. As discussed in Chapter 2.1, the only observational realm to detect the resultant decay-photons is at γ -ray energies. In the following section we discuss the state of γ -ray observations of SNRs just prior to and including the *Fermi* era, as well as the vital role that *Fermi* has played and will continue to play in probing the origin of CRs and emission mechanisms acting at SNR shocks.

4.4 Supernova Remnants at γ -ray Energies

By the end of its science run, EGRET had detected 271 sources above 100 MeV, within a minimum detection significance of 4σ , 170 of which had no clear multi-wavelength counterpart, with 81 of those unidentified lying within $|b| < 10^\circ$ of the Galactic plane (Hartman et al. 1999).

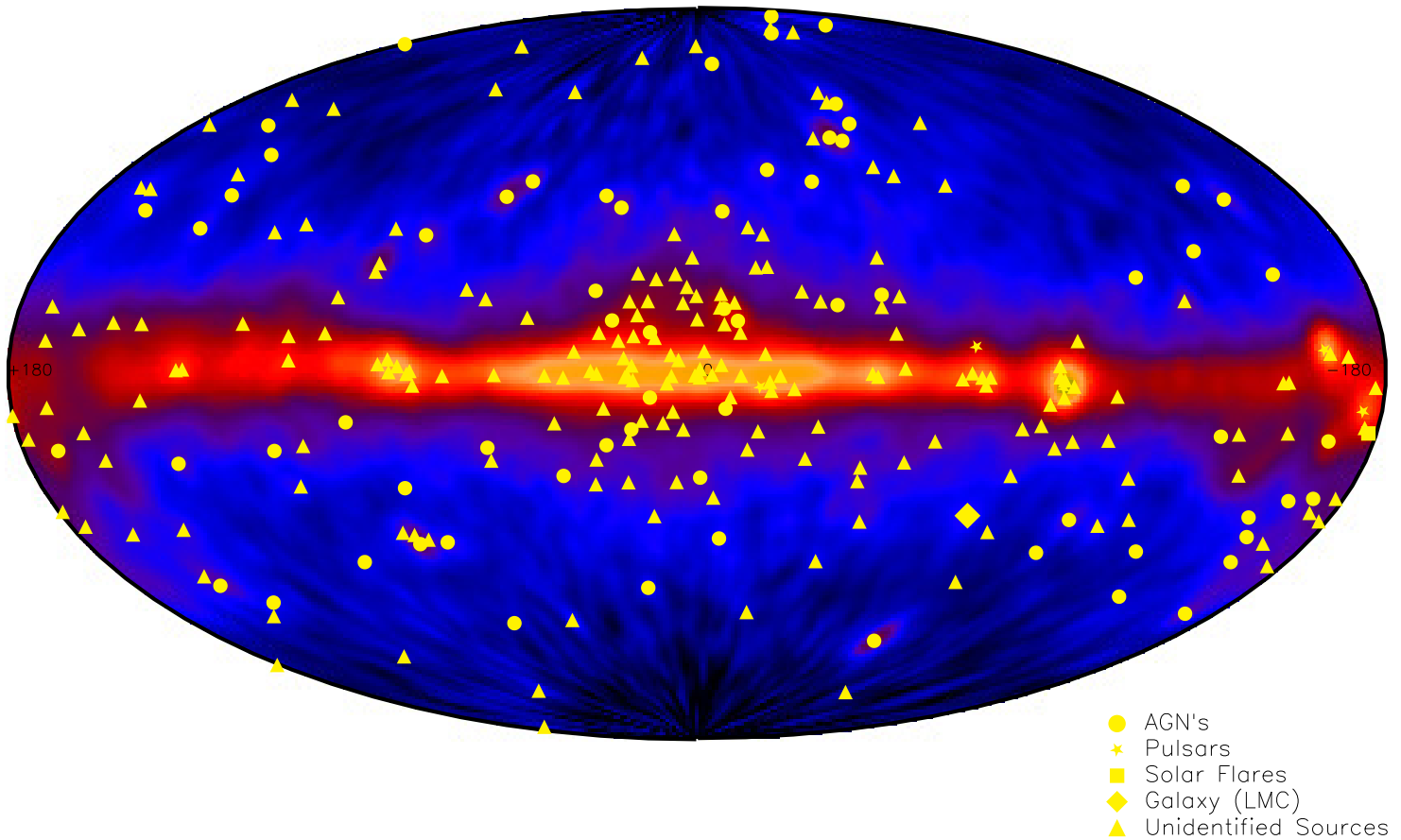


Figure 4.3: Third EGRET catalog all-sky map. Unidentified sources represented by triangles. Image courtesy of <https://heasarc.gsfc.nasa.gov/docs/cgro/images/epo/gallery/skymaps/>

Figure 4.3 shows an EGRET all-sky map for $E > 100$ MeV where the preponderance of unidentified sources and locations thereof are made clear. Many studies have tried correlating the unidentified EGRET sources with various Galactic popu-

lations, several of which attempted to assess how likely it was for the low-latitude sources to have an SNR origin. The main hindrances to source identification with EGRET were the numerous potential source counterparts (the instrument’s PSF was energy dependent, with a 68% containment radius of $\sim 6^\circ$ at 100 MeV and smaller for higher energies) and the large EGRET error boxes (Hartman et al. 1999). For SNRs at γ -ray energies, the signature non-thermal synchrotron component that distinguishes radio and X-ray remnants does not typically extend to such high energy, and the other electron and proton loss channels often overlap and are difficult to disentangle (see Chapter 2.1). The primary method for identifying a γ -ray source as an SNR is through positional coincidence and a compatible angular extent with observations at some other wavelength. Thus the ability to resolve emission from an SNR is vital to understanding the mechanisms therein giving rise to γ -rays.

In spite of the difficulties in EGRET source association Sturner & Dermer (1995), Esposito et al. (1996), and Romero et al. (1999) found strong evidence for statistical correlation between SNRs and some of the low-latitude unidentified sources. In a review of the state of potential SNR / EGRET associations, Torres et al. (2003) showed that there were 19 unidentified EGRET sources that had an SNR fall within its 95% error box. Performing Monte Carlo simulations of the population of EGRET sources, they determined that the chance probability for the 19 sources to be coincident with an SNR was 1.05×10^{-5} , implying a probability of 0.99998 that at least one of the associations was real. Despite the statistical correlation of EGRET sources with SNRs, there were no definitive associations of an SNR with any EGRET sources.

As the successor to EGRET, the LAT was designed to improve upon its predecessor in a multitude of areas relevant to detecting SNRs (Ackermann et al. 2012c; Atwood et al. 2009). The LAT has a much improved angular resolution (68% single-

photon containment radius $\sim 0.4^\circ$ at 1 GeV for photons with the best quality direction reconstruction, PSF3 event type, compared to $\sim 1.7^\circ$ for EGRET at the same energy), which is necessary to resolve SNRs as extended objects. The LAT also benefits from a superior sensitivity due to a combination of the improved PSF, larger peak effective area ($\sim 9500 \text{ cm}^2$ vs. $\sim 1500 \text{ cm}^2$), wider FoV (2.4 sr, which is nearly 5 times that of EGRET), and deeper, more-uniform sky exposure (afforded by the LAT’s scanning observations as opposed to EGRET’s pointing operation). All of the above applies to the Pass 8 IRFs (see Chapter 3.2 for details on the LAT’s performance).

This bump in sensitivity results in the LAT detecting considerably more sources than EGRET. Remarkably, within its first three months of commission, the LAT detected 205 sources above 10σ significance (Abdo 2009), and by 11 months, 1451 sources above 4σ (Abdo et al. 2010a), compared to the aforementioned 271 over the entire EGRET mission. In fact, over its lifetime, EGRET detected a total of about 1.5×10^6 cosmic photons (Thompson et al. 1993), while as of June 2016, the LAT has detected $\sim 873 \times 10^6$ events . The LAT’s point-source sensitivity peaks between 1 and 10 GeV, depending on location on the sky (see Figures 3.8 and 3.9). With its increased sensitivity and higher energy range compared to EGRET (up to $\sim 2 \text{ TeV}$ with the recent Pass 8 event reconstruction improvements, which is nearly an order of magnitude higher than EGRET), the LAT is uniquely situated to study γ -rays from SNRs, with the capability to shed light on CR origins and acceleration mechanisms.

Prior to the new work presented in Chapter 5 of this thesis, there had been no systematic study of the population of LAT detectable SNRs; all reported LAT SNRs were discovered in individual analyses. Second *Fermi*-LAT source catalog (2FGL) compiled these results and reported firmly identifying 7 γ -ray sources as

SNRs and 4 as PWNe. 4 2FGL sources were found to be potentially associated with SNRs (these were point sources positionally coincident with known SNRs but lacking morphological confirmation), and 58 sources were positionally coincident with an SNR/ PWN complex, yet it was inconclusive whether the γ -ray emission had an SNR or PWN origin. We discuss our contribution (as well as that of others) to the total LAT SNR population in Chapters 5 and 6.

Several classes of SNRs have begun emerging from the identified LAT SNR population. The most numerous of these are Sedov-Taylor phase, evolved SNRs (typically composite or mixed-morphology type, and $\gtrsim 10^3$ yr old). These remnants are typically known to be interacting with nearby molecular clouds through shocked molecular lines, CO line broadening, and possibly OH 1720 MHz maser emission (these systems are sometimes referred to as SNR-MCs). There are two interaction models that exist for accelerating particles to γ -ray emitting energies through interacting with molecular clouds: **1.** The “crushed-clouds” scenario where molecular clouds that have been overtaken by the SNR shock can accelerate CRs (or possibly re-accelerate an existing CR population) and produce γ -rays (Uchiyama et al. 2010) or **2.** through the energy dependent escape of high energy CRs from the shock of the SNR that subsequently diffuse in the surrounding medium and collide with nearby molecular material Aharonian & Atoyan (1996); Gabici et al. (2009); Ohira et al. (2011). See Figure 4.4 for an example of a LAT observed SNR with escaping CRs interacting with surrounding material. Interactions of these types, i.e. with a dense target material, lead to an observed enhanced luminosity (see Figure 5.13, and 7.7 for examples of the enhanced luminosity of the SNRs) and their emission is often either hadron dominated or shows signs of both leptonic and hadronic emission.

The second emergent class are the dynamically-young, shell-type SNRs. At LAT energies these SNRs are less luminous, likely due to the shock not expanding for long

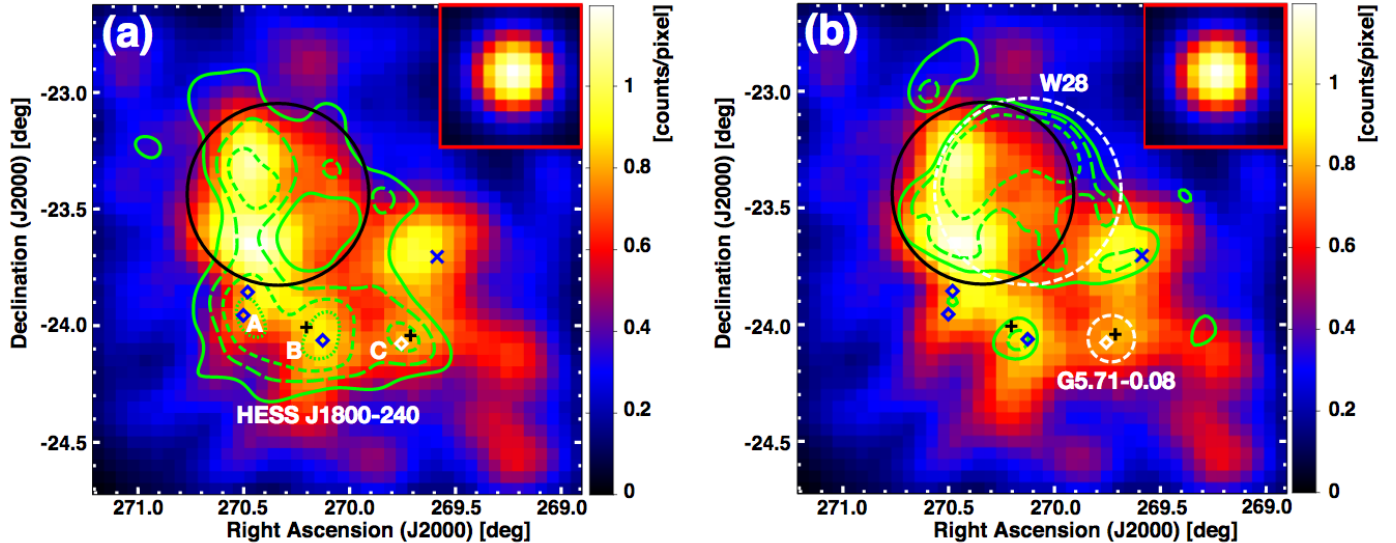


Figure 4.4: *Fermi*-LAT counts map from 10-100 GeV of the region around SNR W28. Black circle shows the Green's catalog radius of W28. Left plot shows correlation of the LAT emission near W28 with TeV illuminated molecular clouds (green contours). Right plot demonstrates GeV emission clearly outside the VLA 90 cm image of the shell of W28 (green contours) Figures from Hanabata et al. (2014).

enough to encounter any surrounding over-density of material. The good correlation between the γ -ray emission and the SNR shell suggests that particle acceleration is occurring at the shock front, and thus the γ -ray rays serve as a direct probe of DSA. These SNRs also seem to exhibit harder spectral indices than their evolved counterparts. The hard indices exclude the DSA proton test particle scenario, and are more compatible with an electron test particle Acero et al. (2015a), although this can also be a result of mixed leptonic/hadronic emission, or deviations from the standard hadronic test particle case.

The advent of the LAT presents for the first time the capability to spectrally and spatially resolve SNRs at GeV energies, which is important because SNR spectra at GeV energies are not just featureless PLs. An unexpected discovery in detecting and studying SNRs with the LAT is that evolved SNRs exhibit a spectral break between

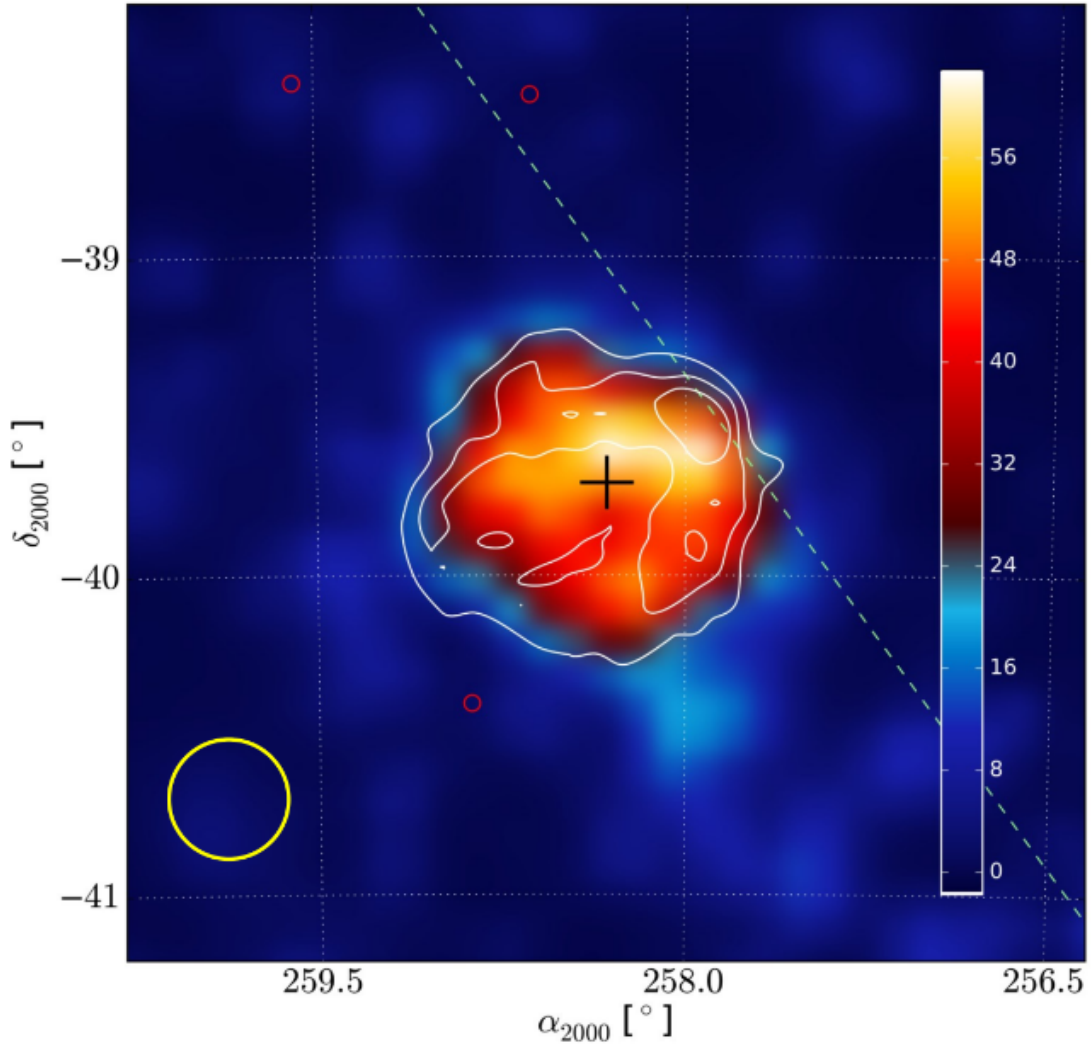


Figure 4.5: TS map for RX J1713.7-39.46 (see Chapter 7.2.2 for definition of TS map) as an example of a LAT observed, dynamically young, shell-type SNR. Good correlation is shown with the HESS significance contours, shown in white. Figure from Federici et al. (2015).

1-10 GeV (Hewitt & Lemoine-Goumard 2015). Explanations for the break range from Alfvén wave evanescence generated by collisions of partially ionized material in molecular clouds (MCs) overtaken by SNR shocks (Malkov et al. 2011), reflected shocks in clouds Inoue et al. (2010), and energy-dependent diffusion from shocks Ohira et al. (2011).

In addition to detecting many SNRs at γ -ray energies, the LAT has been instrumental in providing the first unequivocal evidence of proton acceleration at an SNR shock-front. Ackermann et al. (2013a) reported observations of SNRs W44 and IC443, which are the two highest flux SNRs detected by LAT and among the brightest LAT sources on the sky. With 4 years of data, and the recent (at the time) Pass 7 updated event-class analysis, Ackermann et al. (2013a), were able to extend the observation energy down to 60 MeV, significantly detecting the characteristic “pion-bump” feature (see Chapter 2.1.4 for a description of hadronic γ -ray emission). Detection of this feature by the LAT was integral in constraining the spectral energy distribution (SED) and hence non-thermal spectral models of each of the SNRs. The constrained models demonstrated that a hadronic origin for the observed emission, in both SNRs, was the only viable emission mechanism, and that protons can definitively be accelerated by SNR shocks.

Despite being the prime energy range to observe the effects of cosmic particle acceleration, complexities at the lower LAT energy range stymie SNR morphology studies. The LAT detects a strong, soft band of diffuse emission in the Galactic plane due to the interactions of CRs with interstellar material. This bright diffuse radiation combined with the multiple potential emission scenarios, broadening PSF at decreasing energy, and a high source density in the plane can make it difficult to spatially disentangle sources observed by the LAT. To circumvent these difficulties, the majority of the analyses undertaken in this thesis are focused on the $E \geq 1$ GeV energy range. This energy band is ideal for probing the properties of the accelerated particle populations present in the SNR environment. Studies of SNRs above 1 GeV benefit from the finer LAT PSF, striking a balance between minimizing the diffuse contribution, maximizing photon sensitivity, and retaining good photon statistics.

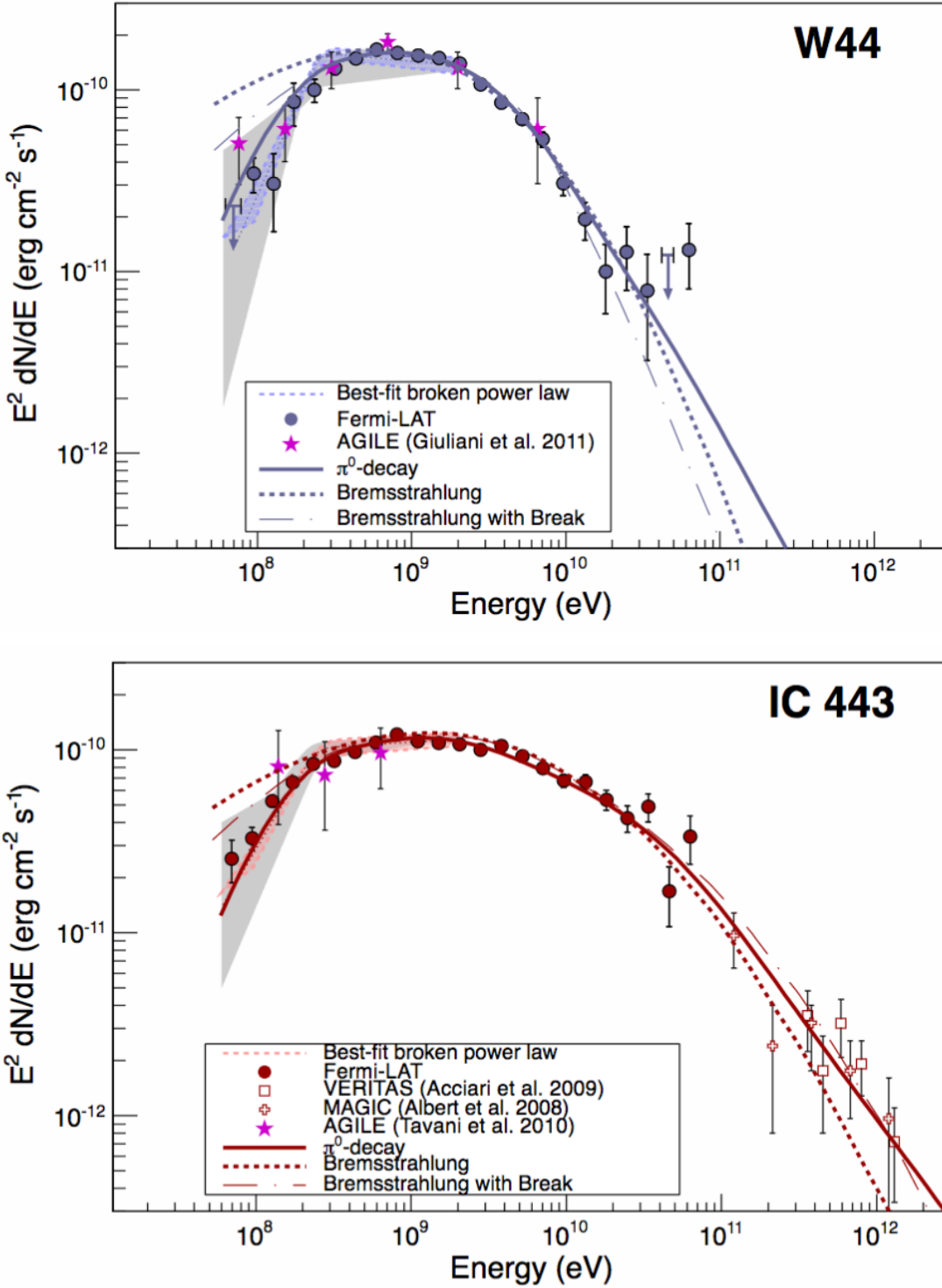


Figure 4.6: γ -ray SEDs of SNRs W44 (top) and IC443 (bottom) obtained by the LAT. Solid lines are for the best-fit pion-decay model, and dashed lines represent the best-fit bremsstrahlung model. A bremsstrahlung model can not sufficiently explain the observed γ -ray emission, unless an ad hoc, low-energy spectral break is included in the bremsstrahlung model (dash-dotted line). Figures from Ackermann et al. (2013a).

Chapter 5

An Automated Method for LAT Analysis of the Galactic Supernova Remnant Population

5.1 Introduction

Two of the primary science goals of the LAT are to 1. resolve the γ -ray sky, uncovering the nature of the unidentified sources detected by EGRET, and 2. to understand the mechanisms of cosmic particle acceleration (Atwood et al. 2009). In this chapter, we describe our efforts towards addressing these questions by studying the γ -ray emission coincident with sources comprising the population of known radio emitting SNRs.

Prior to this work, several individual studies with the LAT had successfully resolved spatially extended emission from SNRs (Nolan et al. 2012, and references therein), yet no systematic analysis leveraging the LAT’s full-sky coverage had thus been attempted. We performed for the first time a uniform study of the SNRs in

aggregate to measure the properties common to these objects. An understanding of these common characteristics allows us to assess SNRs as a class of γ -ray and CR emitting objects and serves as the impetus for this uniform analysis of the known Galactic SNRs. We report here on the published results from the First *Fermi*-LAT Supernova Remnant Catalog (SNRcat) (Acero et al. 2016).

5.2 The pointlike Maximum-Likelihood Package and addSrcs

As described in Chapter 3.4, maximum-likelihood analysis is the ideal method for determining the properties of LAT-observed sources due to the “counting-experiment” nature of *Fermi*-LAT. The standard maximum-likelihood tools for analyzing LAT data are implemented via the *Fermi* Science Tools, and in particular `gtlike`. Despite being the optimum method, likelihood analysis of LAT data is complex due to the highly non-linear performance of the instrument and can be computationally expensive. It is necessary to manage the data and response of the telescope as well as the source and background models. Furthermore, due to the broadening of the PSF at low energies, even when studying a single source, it is necessary to include in the model descriptions of multiple surrounding sources. The `pointlike` binned maximum likelihood package was created to ameliorate some of these issues. Described in detail in Kerr (2010), `pointlike` is an alternate likelihood analysis framework (a collection of Python modules with additional wrappers for accessing C++ code), designed to be interactive and rapidly evaluate likelihoods.

There are several ways in which `pointlike` improves in efficiency compared to the Science Tools. It saves computational time, while sacrificing some accuracy, with several assumptions and approximations, such as the PSF not varying strongly

with photon incidence angle (allowing a single PSF for each individual bin), and sources having a steady flux in individual short time bins. Most importantly though, `pointlike` varies the size of spatially binned **HEALPix** pixels (Górski et al. 2005) according to energy. The PSF at lower energies is large and each energy bin can contain multiple counts, while at higher energies, the PSF shrinks and many pixels will not contain even a single count. `pointlike` creates **HEALPix** bins that are approximately the size of the PSF at a given energy, and disregards empty bins to speed up the likelihood calculation.

In addition to these computational, time saving efficiencies, tools to analyze spatially extended sources have also been built into the `pointlike` framework. Studying the position and extension of an extended source, while possible with the standard *Fermi* Science Tools, is a cumbersome process. `gtlike` is not capable of simultaneously maximizing the likelihood of a source’s spectral and spatial parameters, so to assess the morphology of a source, an iterative process of fitting a spatially fixed source’s spectrum and then varying the sources centroid and extension is required. To address the issues that arise when studying individual extended sources, Lande et al. (2012) developed and validated spatial likelihood fitting tools for `pointlike`, taking advantage of the time-saving properties built therein.

To fit the position and extension of a source, `pointlike` assumes that the spatial and spectral distribution of a source’s expected photon distribution are separable. The extended source’s shape is convolved with the LAT PSF (which is a function of energy) to determine the expected distribution. Then, the `minuit` numerical minimization library (James & Roos 1975) is used to maximize the likelihood of the model by simultaneously varying the spectrum, extension, and position of the source. Various geometric surface brightness models are built into `pointlike`, including, but not limited to a uniform intensity disk and ring, and a 2D Gaussian, with radially and

non-radially symmetric versions of each. Akin to the speed optimizations mentioned previously, for radially symmetric sources, `pointlike` calculates the angular integral of a source's expected photon distributions analytically to save computational time.

The significance of extension of a source is determined by using the LRT, described in Chapter 3.4. Applying the LRT to the hypothesis of a spatially extended source, we can calculate the significance of a source being extended compared to that of the source being modeled as point source as:

$$TS_{\text{ext}} \equiv 2 \log(\mathcal{L}_{\text{es}} / \mathcal{L}_{\text{ps}}) = TS_{\text{es}} - TS_{\text{ps}}, \quad (5.1)$$

Lande et al. (2012), extended (and verified) the definition of TS (see equation 3.4) to calculating the significance of extension, replacing the source flux with its radius. The uncertainty of the extension parameter is estimated by fixing a source's position while varying the extension until the log likelihood decreases by 1/2 from the maximum value (i.e. 1σ errors). A similar procedure is used to estimate the errors on a source's position, but rather, fixing the extension and spectrum (Nolan et al. 2012). While `pointlike` is a tool for the analyses described above, `gtlike` is still the go-to for estimating the best-fit spectral parameters since it is expected to be slightly more accurate than `pointlike` since it makes approximations. For the studies in this thesis, we used `pointlike` to calculate extension and source positions, and then use the `pointlike` results as a starting point for the likelihood parameter estimation of spectra with `gtlike`.

With its efficient likelihood calculations, and ability to simultaneously fit both the spectral and spatial parameters of a source, `pointlike` is ideally suited for large-scale studies (like the all-sky analyses performed for the LAT point source catalogs), and analyses requiring several iterations. Studying the γ -ray emission from the population of Galactic SNRs is precisely the sort of analysis that `pointlike`

was designed to perform. To attain the best understanding of a source of interest, the best characterization of the corresponding region of interest (RoI) is necessary. In particular, to understand the GeV emission from a potentially extended SNR, it is important to quantify the surrounding emission because of the steep energy-dependence of the LAT PSF. This can be especially challenging in dense source and strong diffuse-dominated regions, like the Galactic plane where the SNRs we are studying lie. We have developed an automated method for systematically locating and modeling all potential point and/or extended sources in an RoI using `pointlike`.

A typical LAT analysis starts by including all sources from the most recent LAT point source catalog and modifying the RoI to suit ones needs. Unmodeled emission can arise if using a dataset longer than that used in the most recent catalog or by focusing on a different energy range compared to that of the catalogs. We created a Python subclass of the primary `pointlike` analysis object (which works within that framework, inheriting all of the class' features, while adding new functionality) to systematically and uniformly characterize sources in an RoI by finding residual, unmodeled emission in the region and iteratively add sources to the RoI to account for this emission. The main module in the designed codebase was dubbed `addSrcs`.

The general work flow of `addSrcs` is to start with a model of the RoI, including some combination of the diffuse background components, point and extended sources. `addSrcs` reads in a residual TS map or creates one on the fly if none is passed in. Residual emission is detected by finding the peak emission in the TS map and adding a source to the existing RoI at the position of the peak pixel. Either all point or extended sources can be iteratively detected and added to the RoI. For the SNRcat, we exclusively ran `addSrcs` in point source mode. Chapter 6 provides an application of `addSrcs` for extended sources.

In point source mode, a point source with a PL spectrum is added to the model

of the region, a likelihood fit of the RoI is performed, and subsequently, the source’s position is localized. Similarly, in extended mode a PL extended source (of any morphological form included in `pointlike`) is added to the RoI with a small seed radius, and the spatial parameters of the newly added source are fit simultaneously with the spectra of the other sources already in the model. If the source has $\text{TS}_{\text{ext}} < 16$ (equivalent to a 4σ extension significance and validated through simulations in Lande et al. (2012) as a reasonable extension detection significance), the extended source is replaced with a point source and the iteration continues as in point source mode. To extend the functionality of `addSrcs` and make it generally applicable to a multitude of LAT analyses, several optional methods were built in.

One such option is to test the newly added source for signs of spectral curvature (described further in Chapter 5.6). If the source is found to show significant spectral curvature, the appropriate curved spectral model is retained, otherwise, we revert to the best-fit PL model. Another option provided is to fix the new sources spectrum if it is within a given angular separation of the center of the RoI to limit the number of free parameters for the likelihood fit and aid in proper convergence. If the source of interest being studied is not central in the RoI it might be beneficial to free the spectral parameters of sources within a given distance of the newly added source rather than from the center of the RoI. This choice was also built into `addSrcs`. Further, we included an option to refit the extension of any extended source already in the model at each iteration if they are within a given distance of the new (point or extended) source. Due to the broad size of the PSF, nearby source spectra can be influenced by each other, (particularly for extended sources) so the iterative procedure allows the likelihood to relax to a preferred value when adding new sources.

Throughout the `addSrcs` process, various checks are performed to ensure that

parameter values are reasonable, the likelihood fit converges, and the procedure is generally running as expected. The range of permissible fit values for a parameter can be limited, the values of the parameters themselves can be fixed, or a consistently poorly-fit source can be automatically removed from the model. During the source localization step, if the fit goes awry and the source wanders too far from its initial position, the position of the source can be rolled back to its staring location and fixed. Checks were also included to keep track of the Galactic diffuse and isotropic emission models to ensure they were adequately fit.

The penultimate step of the iteration is to produce various diagnostic plots and output information about the fits, the spectral and spatial parameters of each source in the model, and other relevant information such as the TS of the source and loglikelihood of the fit. Finally, a new residual TS map of the region is created and the source addition procedure repeats until a given threshold in TS is reached. The peak pixel TS found in the residual TS map does not necessarily decrease monotonically, as is expected of the actual TS of successive sources as more of the emission is accounted for and the model improved. Since the peak pixel TS can fluctuate a bit, to ensure that we do not miss significant sources in the RoI, we continue adding sources until the TS threshold is reached for some number of successive sources (discussed further in 5.6). After sources are no longer being added to the region, we iteratively remove sources with TS less than a given threshold (typically $TS < 16$, again see Chapter 5.6) starting with the lowest TS sources first. As each source is removed, we refit the RoI, including any extended sources close to the removed source. When the TS of all sources in the RoI are above threshold, we deem the emission in the RoI to be sufficiently characterized.

In the following sections, we detail the application of `addSrcs` to studying the GeV Galactic SNR population and describe the analysis and results presented in

Acero et al. (2016).

5.3 Galactic Supernova Remnants

In this work we focus on the 279 currently known Galactic SNRs. They are derived from the 274 SNRs noted in the catalog of Green (2009, hereafter Green’s catalog), plus five additional SNRs identified following its publication. All but 16 of these SNRs have been identified by their radio synchrotron emission, so their centroids and extensions are primarily determined from the radio. When the radio detection is not securely identified through the synchrotron emission, positional information is obtained from the optical, X-ray, or TeV observations that identified the SNR, as noted in Green’s catalog. The catalog is thought to be complete down to a 1 GHz radio surface brightness limit of $\approx 10^{-20} \text{ W m}^{-2} \text{ Hz}^{-1} \text{ sr}^{-1}$ (i.e. 1 MJy sr^{-1}). However, selection effects are known to bias radio surveys against the identification of radio faint and small angular size remnants (Brogan et al. 2006; Green 2004). We note that as this work neared completion, a revised catalog of 294 SNRs was published (Green 2014), representing only a small increase ($< 10\%$) over the previous catalog.

5.4 Analysis Methods

To systematically analyze the *Fermi*-LAT γ -ray data, we apply a maximum likelihood (Mattox et al. 1996) framework to RoIs centered on known SNRs (Green 2009). For each SNR, we begin by constructing a model for the spectral and spatial dependence of the γ -ray emission which includes significant point sources in the ROI. We then test for the existence of a γ -ray source near the center. This includes determining the most likely position and extension of the candidate source and testing for spectral curvature, rather than assuming it follows a PL across the energy

range studied. In cases where we find no significant source associated with the SNR, we calculate upper limits on the flux. We calculate both statistical and systematic errors, where the latter are estimated from both the uncertainty in the effective area and the effects of changing the interstellar emission model (IEM), which accounts for γ -rays produced by CR interactions with interstellar gas and radiation fields in the Milky Way.

This analysis uses both the standard Science Tools (version 09-32-05), including `gtlike`, and the `pointlike` analysis package (Kerr 2010) which has been developed and verified for characterizing source extension for *Fermi*-LAT data (Lande et al. 2012). §5.5 describes our data selection; §5.6 details our new method for automatically finding point sources in the *Fermi*-LAT γ -ray emission; and §5.8 discusses the detection method.

5.5 Data Selection

This catalog was constructed using 3 years of LAT survey data from the Pass 7 (P7) “Source” class and the associated P7V6 IRFs. This interval spans 36 months, from 2008 August 4 to 2011 August 4 (mission elapsed time 239557417 – 334108806). The Source event class is optimized for the analysis of persistent LAT sources, and balances effective area against suppression of background from residual misclassified charged particles. We selected only events within a maximum zenith angle of 100° and use the recommended filter string “`DATA_QUAL==1 && LAT_CONFIG==1`” in `gtmktime`¹. The P7 data and associated products are comparable to those used in the other γ -ray catalogs employed in this work. We used the first three years

¹See LAT data selection recommendations at: http://fermi.gsfc.nasa.gov/ssc/data/analysis/documentation/Cicerone/Cicerone_Data_Exploration/Data_preparation.html.

of science data for which the associated IEM is suitable for measuring sources with extensions $> 2^\circ$ ². A detailed discussion of the instrument and event classes can be found in Atwood et al. (2009) and at the *Fermi* Science Support Center¹.

For each of the 279 SNRs we modeled emission within a 10° radius of the SNR's center. As a compromise between number of photons collected, spatial resolution, and the impact of the IEM, we chose 1 GeV as our minimum energy threshold. The limited statistics in source class above 100 GeV motivated using this as our upper energy limit.

To avoid times during which transient sources near SNRs were flaring, we removed periods with significant weekly variability detected by the *Fermi* All-sky Variability Analysis (FAVA) (Ackermann et al. 2013b). We conservatively defined a radius within which a flaring source may significantly affect the flux of a source at the center. We take this distance to be the radio radius of an SNR plus 2.8° , corresponding to the overall 95% containment radius for the *Fermi*-LAT point spread function (PSF) for a 1 GeV photon at normal incidence (Ackermann et al. 2012c). The time ranges of FAVA flares within this distance were removed in 23 RoIs, leaving $\geq 98.9\%$ of the total data in each RoI.

²See the LAT caveats, http://fermi.gsfc.nasa.gov/ssc/data/analysis/LAT_caveats.html, particularly those for the IEM developed for Pass 7 reprocessed data described in http://fermi.gsfc.nasa.gov/ssc/data/access/lat/Model_details/FSSC_model_diffus_reprocessed_v12.pdf.

5.6 Input Source Model Construction

To characterize each candidate SNR we constructed a model of γ -ray emission in the RoI which includes all significant sources of emission as well as the residual background from CRs misclassified as γ -rays. We implemented an analysis method, built upon the `addSrcs` method described in ??, to create and optimize the 279 models for each of the 279 RoIs. For each RoI, we initially included all sources within the 10° RoI listed in the 2FGL (Nolan et al. 2012), based on 2 years of Source class data. To this we added pulsars from the Second *Fermi*-LAT catalog of Gamma-ray Pulsars (2PC) (Abdo et al. 2013), based on 3 years of source class data, with 2PC taking precedence for sources that exist in both. For the diffuse emission we combined the standard IEM corresponding to our P7 data set, `gal_2yearp7v6_v0.fits`, with the standard model for isotropic emission, which accounts for extragalactic diffuse γ -ray emission and residual charged particles misclassified as γ -rays. Both the corresponding isotropic model, `iso_p7v6source.txt`, and the IEM are the same as used for the 2FGL catalog analysis³.

Compared to 2FGL, we used an additional year of data and limited the energy range to $1 - 100$ GeV. This can result in different detection significances and localizations than previously reported in 2FGL. To account for these effects, we recreated the RoIs' inner 3° radius regions, which encompass the radio extents of all known SNRs, observed to be $\leq 2.6^\circ$ and allows a margin for the LAT PSF. The weighted average 68% containment radius of the LAT PSF for events at 1 GeV is $\sim 0.7^\circ$ (Ackermann et al. 2012c). We note that this implicitly assumes that an SNR's GeV extent should not be more than about an order of magnitude larger than its radio

³Further details on the diffuse emission models are available at <http://fermi.gsfc.nasa.gov/ssc/data/access/lat/BackgroundModels.html>

extension and also note that the selection biases stated in Green’s catalog limit the range of known SNRs’ radio extensions.

To build the inner 3° radius model of each ROI, we first removed all sources except identified active galactic nuclei (AGN) and pulsars, whose positions on the sky are independently confirmed by precise timing measurements (Abdo et al. 2013). Retained AGN were assigned their 2FGL positions and spectral model forms. Pulsars’ positions and spectral forms were taken from 2PC. 2FGL sources identified or associated with SNRs are removed when they lie within the inner 3° .

Using `addSrcs`, we generated a TS map via `pointlike` on a square grid with $0.1^\circ \times 0.1^\circ$ spacing that covers the entire ROI. At the position of the maximum TS value, we added a new point source with a Power Law (PL) spectral model:

$$\frac{dN}{dE} = N \frac{(-\Gamma + 1)E^{-\Gamma}}{E_{\max}^{-\Gamma+1} - E_{\min}^{-\Gamma+1}} \quad (5.2)$$

where N is the integrated photon flux, Γ is the photon index, and E_{\min} and E_{\max} are the lower and upper limit of the energy range in the fit, set to 1 GeV and 100 GeV, respectively. We then performed a maximum likelihood fit of the ROI to determine N and Γ and localized the newly added source. The significance of a point source with a PL spectral model is determined by the χ^2_n distribution for n additional degrees of freedom for the additional point source, which is typically slightly less than $\sqrt{\text{TS}}$

To promote consistent convergence of the likelihood fit, we limited the number of free parameters in the model. For sources remaining after the removal step, described above, we freed the normalization parameters for the sources within 5° of the ROI center, including identified AGN and pulsars. For 2FGL sources between 5° and 10° , we fixed all parameters. The spectrum of the IEM was scaled with a PL whose normalization and index were free, as done in 2FGL. For the isotropic emission model, we left the normalization fixed to the global fit value since the ROIs are too

small to allow fitting the isotropic and Galactic IEM components independently. The isotropic component's contribution to the total flux is small compared to the IEM's at low Galactic latitudes.

After localizing them, the new sources were tested for spectral curvature. In each of the four energy bands between 1 and 100 GeV, centered at 1.8, 5.6, 17.8 and 56.2 GeV, we calculated the TS value for a PL with spectral index fixed to 2 and then summed the TS values. We refer to this as $\text{TS}_{\text{bandfits}}$. A value for $\text{TS}_{\text{bandfits}}$ much greater than the TS calculated with a PL (TS_{PL}) suggests that, with a more rapid calculation, that the PL model may not accurately describe the source. Analogously to 2FGL, we allow for deviations of source spectra from a PL form by modeling sources with a log-normal model known colloquially as LogParabola or logP:

$$\frac{dN}{dE} = N_0 \left(\frac{E}{E_b} \right)^{-(\alpha + \beta \log(E/E_b))} \quad (5.3)$$

where N_0 is the normalization in units of photons/MeV, α and β define the curved spectrum, and E_b is fixed to 2 GeV⁴. If $\text{TS}_{\text{bandfits}} - \text{TS}_{\text{PL}} \geq 25$, we replaced the PL spectral model with a logP model and refit the RoI, including a new localization step for the source. We retained the logP model for the source if the global log likelihood across the full band improved sufficiently: $\text{TS}_{\text{curve}} \equiv 2(\log \mathcal{L}_{\text{logP}} - \log \mathcal{L}_{\text{PL}}) \geq 16$. Otherwise we returned the source to the PL model which provided the better global log likelihood. Across all RoIs, less than 2% of the newly added sources retained the logP model.

We continued iteratively generating TS maps and adding sources within the entire RoI until additional new sources did not significantly change the global likelihood of the fit. The threshold criterion was defined as obtaining $\text{TS} < 16$ for three consecutively added new sources, denoted as $N_{\text{TS} < 16} = 3$. Despite iteratively adding

⁴Note: E_b is a scale parameter which should be set near the lower energy range of the spectrum being fit and is usually fixed, see Massaro et al. (2004)

a source at the location of the peak position in the TS map, the TS values of new sources may not decrease monotonically with iteration for several reasons. First, source positions were localized after fitting the ROI and generating the TS map. Second, some added sources were fit with a more complex spectral model than a simple PL. Finally, when creating the TS map, we fixed the source's spectral index to 2, whereas when adding the actual source to the model, we allowed its index to vary.

The specific value of $N_{TS < 16} = 3$ was chosen to avoid missing sources with $TS \geq 25$ (the threshold commonly used for source detection in LAT data), and to optimize computation time. We tested the threshold by selecting eight representative SNRs from both complex and relatively simple regions of the sky, with both hard and soft spectral indices. The eight chosen regions were:

SNR043.3-00.2 (W49B): A relatively simple region and test case that was previously detected as a point-source SNR (Abdo et al. 2010c)

SNR034.7-00.4 (W44): Previous LAT studies showed the SNR had a GeV extension slightly larger than the radio size as well as surrounding GeV emission from nearby extended sources associated with molecular clouds (Abdo et al. 2010d; Uchiyama et al. 2012)

SNR078.2+02.1 (gamma Cygni): A complex region containing the SNR an embedded pulsar, several nearby pulsars, and a large diffuse structure known as the Cygnus cocoon which is believed to be a bubble of hot gas acting as a source of freshly accelerated CRs (Ackermann et al. 2011, 2012b). The region serves as a test of how robust `addSrcs` is in one of the more extreme ROIs. Despite the complexity of the region, Lande et al. (2012) detected GeV emission co-spatial with the radio SNR.

SNR027.4+00.0 (Kes 73), SNR031.9+00.0 (3C391), SNR292.2-00.5,

SNR332.4-00.4 (MSH 16-51), SNR205.5+00.5 (Monoceros): These five sources were found to have large fitted extensions (greater than twice the radio radius of the SNR) in preliminary SNRcat pipeline runs so were included to understand this occurrence.

We applied the procedure detailed above to the test RoIs using a criterion of $N_{TS<16} = 6$ and counted how many $TS \geq 25$ sources would be excluded if a smaller $N_{TS<16}$ criterion was used. Figure 5.1 shows how reducing the threshold to $N_{TS<16} = 3$ cut only one significant source in any of the regions. A further criteria to validate the value of $N_{TS<16}$ used in this paper was that the spectrum of a source of interest (i.e. the central extended SNR in an ROI) or extension was robust to the addition of nearby sources. In Figure 5.2 we show an example of the evolution of the flux, index, and extension of SNR gamma Cygni as subsequent sources are added. Sources were added to the ROI until $\Delta(\log \mathcal{L}) < 8$, 6 times in a row, and see that while a significant source added close to the SNR can affect the fit of the extended source, these fits stabilize before our threshold is reached. Since the maximum number of sources added in any test ROI was 38, the minimum 14, and the total number of sources added across all test regions was 221, we chose to use $N_{TS<16} = 3$ for the full sample of 279 RoIs.

To allow for proper convergence of the likelihood fit, we reduced the number of free parameters prior to each new source addition. If the previously added source was between 3° and 5° from the center of the ROI, just its normalization was freed, and if greater than 5° all its source parameters were fixed. To avoid having newly added sources overlap with pulsars, we deleted new sources from the ROI if they were within 0.2° of a γ -ray pulsar and refit the pulsar in the $1 - 100$ GeV range following the 2PC conventions. 2PC modeled pulsar spectra as a PL with an exponential

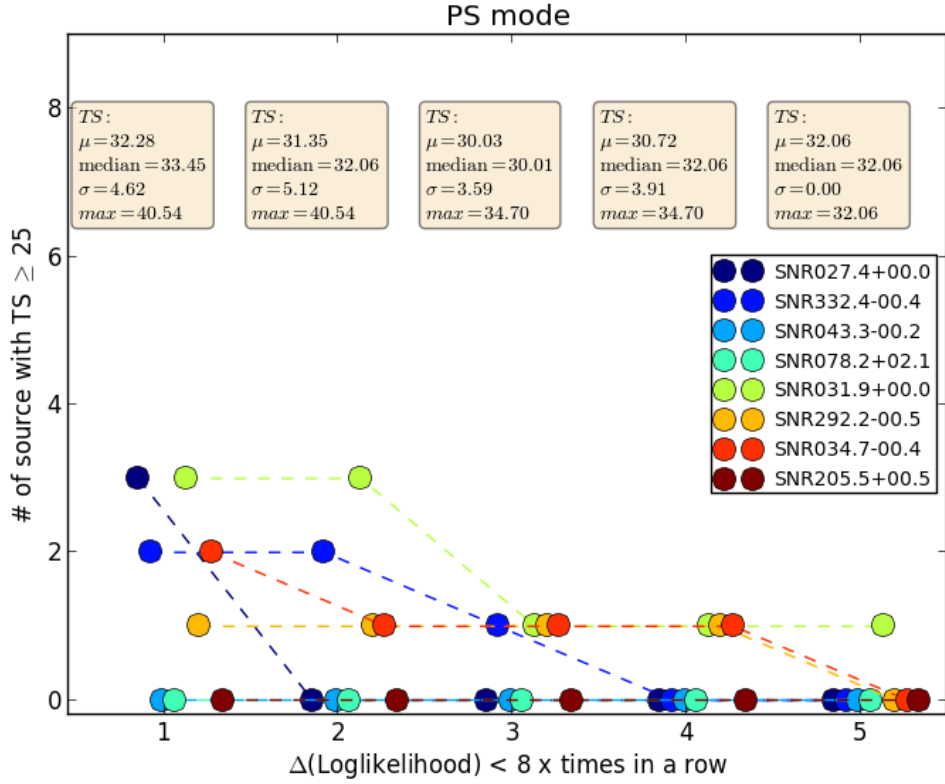


Figure 5.1: Histogram of the number $\text{TS} \geq 25$ sources remaining in each of the 8 test ROI for iterations in which $\Delta(\log \mathcal{L}) < 8$ (i.e. $\text{TS} < 16$). Points are offset for each SNR for clarity. The text boxes detail statistics for the values of TS of significant sources for the 8 studied SNRs for each corresponding value on the x-axis.

cutoff (PLEC),

$$\frac{dN}{dE} = N_0 \left(\frac{E}{E_0} \right)^{-\Gamma} \exp \left(-\frac{E}{E_c} \right)^b, \quad (5.4)$$

where N_0 is the normalization factor, Γ is the photon spectral index, E_c the cutoff energy, and b determines to the sharpness of the cutoff. 2PC assessed the validity of fixing b to 1 in Equation 5.4 (PLEC1) by repeating the analysis using a PL model, as well as the more general exponentially cut off PL form, allowing the parameter b in Equation 5.4 to vary. For the pulsar spectra in this analysis, we compared the maximum likelihood values for spectral models with and without a cutoff and with and without the value of b being free, via $\text{TS}_{\text{cut}} \equiv 2(\log \mathcal{L}_{\text{PLEC1}} - \log \mathcal{L}_{\text{PL}})$ and

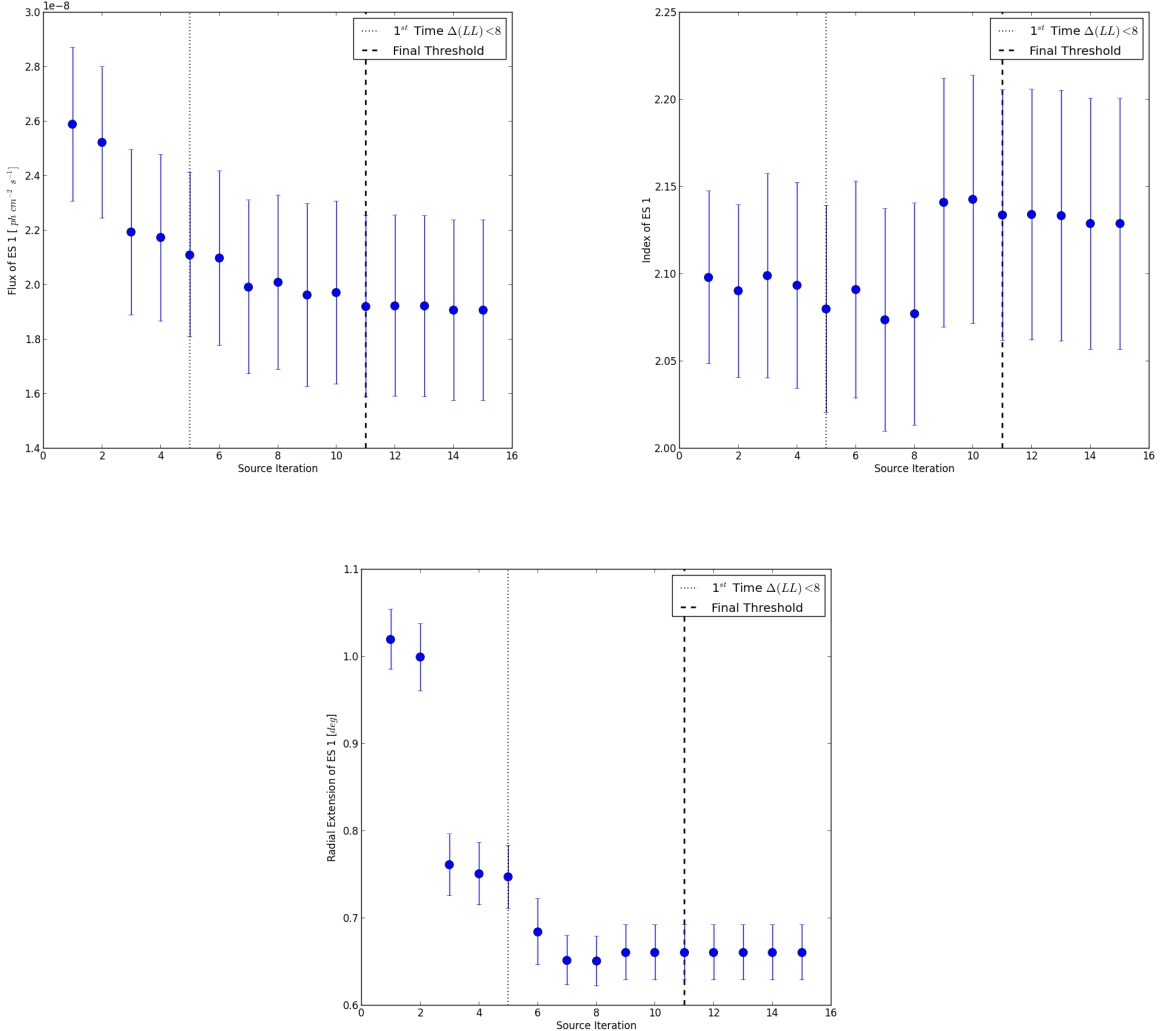


Figure 5.2: Flux (upper left), PL spectral index (upper right), and extension (lower panel) evolution of the extended source coincident with SNR gamma Cygni (labeled ES 1 in the figures) as successive sources are added to the RoI. Dotted line is first time $\Delta(\log \mathcal{L}) < 8$, dashed line shows the final threshold for this test study.

$TS_b \equiv 2(\log \mathcal{L}_{\text{PLEC}} - \log \mathcal{L}_{\text{PLEC1}})$ to determine which to use. If $TS_{\text{cut}} < 9$ is reported for the pulsar in 2PC then a PL model is used. If $TS_{\text{cut}} \geq 9$, we then check to see if the cutoff energy fit in 2PC lies within the restricted energy range of 1 – 100 GeV used in this work. For pulsars with cutoffs ≥ 1 GeV, we then use the PLEC model if

$\text{TS}_b \geq 9$, and the PLEC model with cutoff freed otherwise. For those pulsars with cutoffs less than 1 GeV the spectral parameters are fixed to the 2PC values.

To complete the construction of our point source RoI model, we took the output of the previous steps and removed all sources with $\text{TS} < 16$. This final model was then used as the starting model for analyzing candidate SNR emission. In Figure 5.3, we show a residual TS map of the region around SNR W44 as an example of the source configuration in an ROI prior to running `addSrcs`. Figure 5.4 is a residual TS map of the same region after running `addSrcs` to decompose the region into point sources.

We conservatively allow sources with TS down to 16 ($\sim 4\sigma$) in order to account for the effects of at least the brightest sub-threshold sources on the parameter fits for the other sources in the model. Furthermore, while the SNR analysis method described in the chapter 5.8 is allowed to remove sources, it cannot add them. Thus we start from a set of sources designed to allow the final model to capture all significant emission within the central region. To corroborate our method of systematically adding sources to a region, we compare our ROI source models with those found by the 2FGL approach in Chapter 5.7.

5.7 Comparison of Source Models with 2FGL

This SNR catalog was constructed using 3 years of P7 Source class data in the energy range 1 – 100 GeV, whereas 2FGL used 2 years of data over the larger energy range 0.1 – 100 GeV. The differences in observing time and energy range resulted in residual, unmodeled emission in some ROIs as well as changes to some 2FGL sources’ spectral model, position localization, and detection significance. Here we compare the input source models constructed for this catalog, described in Chapter

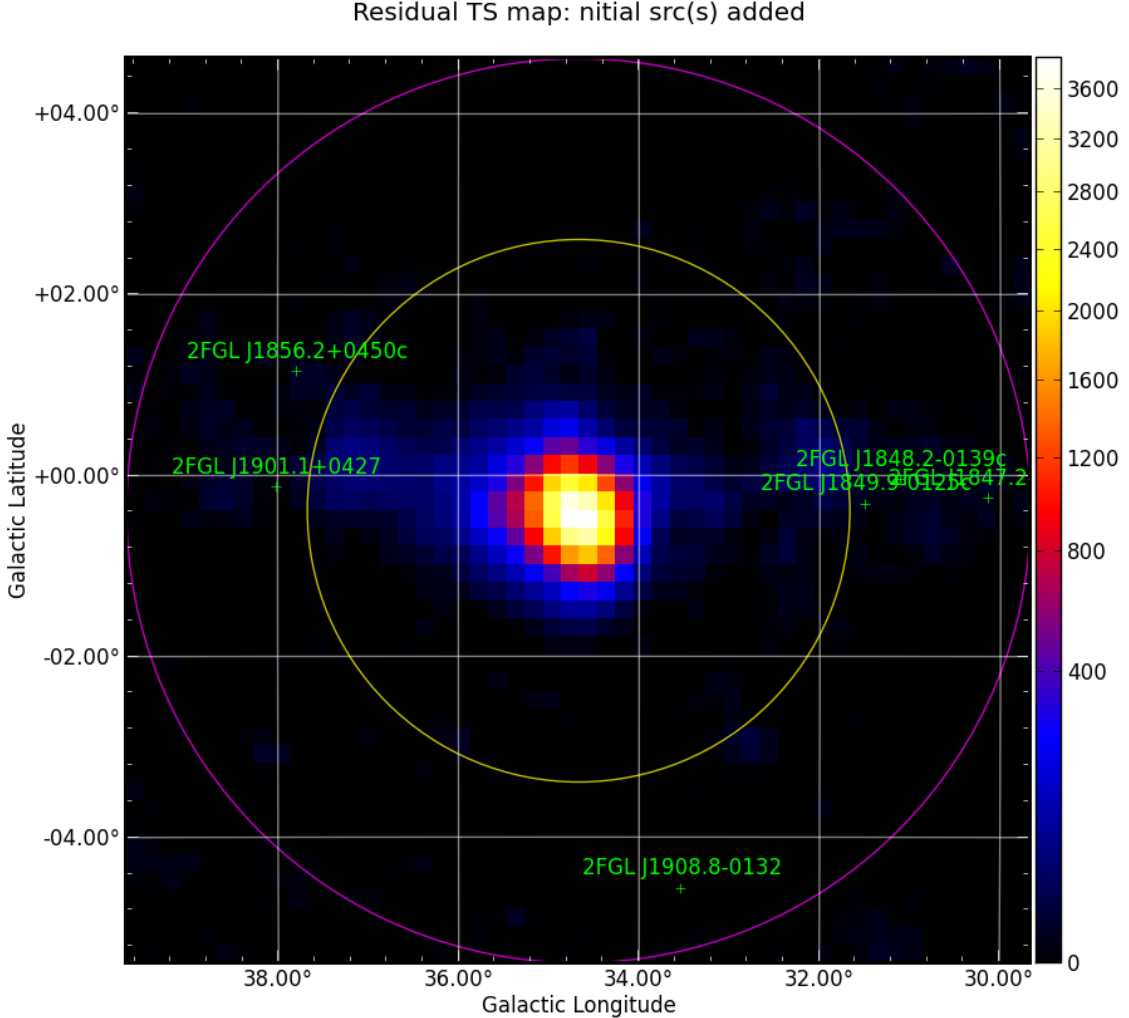


Figure 5.3: 1-100GeV residual TS map for SNRW44 before running `addSrcs` and with 2FGL sources removed from the inner 3° radius (yellow circle). Bin size is $0.2^\circ/\text{pixel}$. Magenta circle shows a 5° radius. 2FGL and newly added sources are shown as green crosses.

5.6, with 2FGL to better understand the `addSrcs` method's ability to describe the regions studied. Since we rederive the input source model only within a 3° radius of the center of each ROI, we consider sources only inside that radius.

Given the data set differences, in each ROI we expect similar but not identical numbers of sources relative to those in 2FGL. Figures 5.5 and 5.6 show the numbers of significant ($\text{TS} \geq 25$) 2FGL sources and derived input model sources (excluding 2FGL identified AGN and pulsars kept in the input model) in individual ROIs as 2D

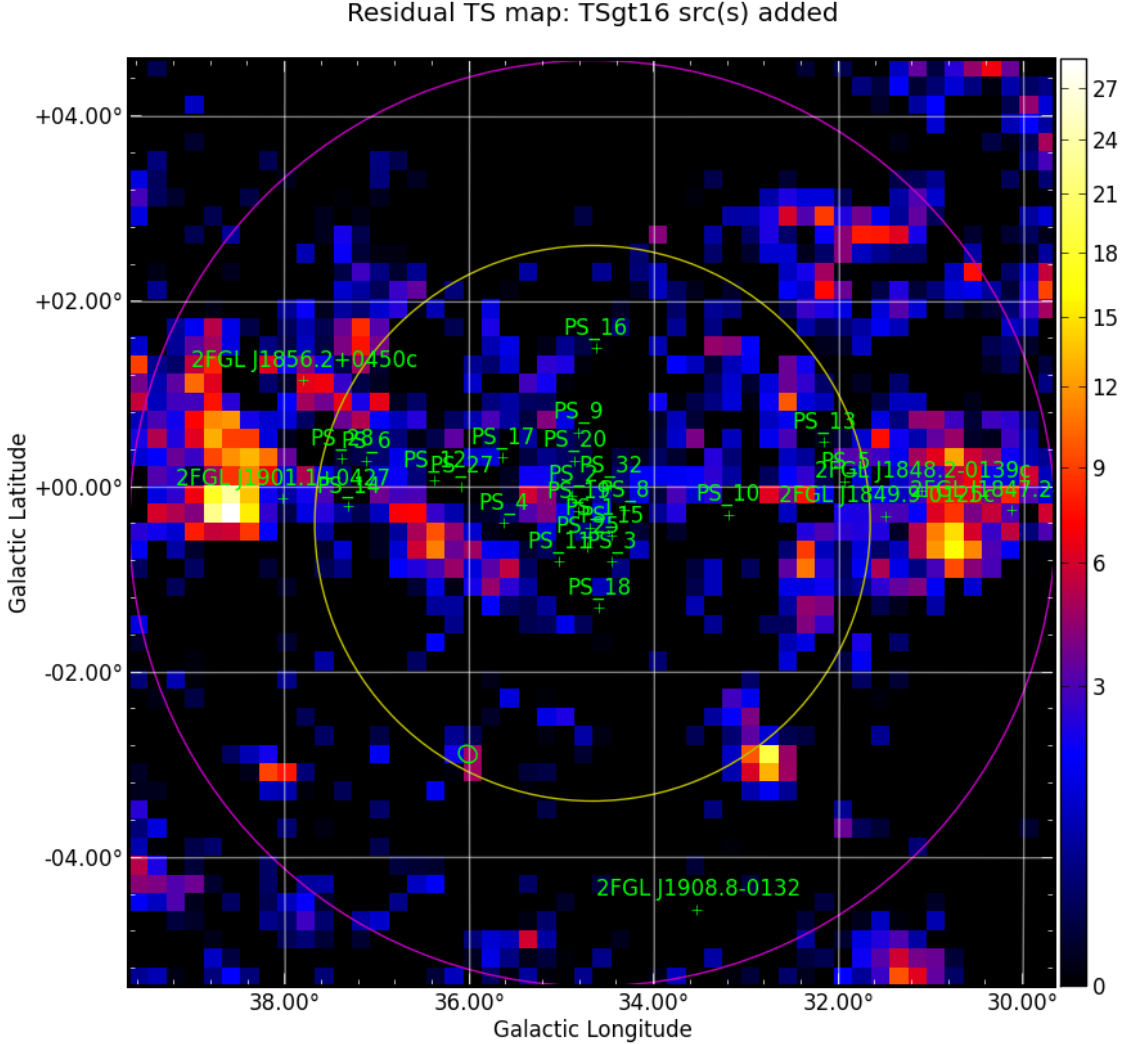


Figure 5.4: 1–100GeV residual TS map for SNR W44 after `addSrcs` has completed. 2FGL sources have been removed from the inner 3° radius (yellow circle), and the bin size is $0.2^\circ/\text{pixel}$. Magenta circle shows a 5° radius. 2FGL sources are shown as green crosses.

histograms. In Figure 5.5, the number of sources in the derived input model is typically greater than the number of 2FGL sources that are significant at 1 – 100 GeV. 73 of the 279 RoIs studied contain at least one of the the 12 extended 2FGL sources. Since 2FGL extended sources were removed from the inner 3° of each ROI, and this region was repopulated with point sources, we can detect multiple point sources inside the extent of any removed extended 2FGL sources. This decomposition of

extended sources, combined with the longer data set and different energy range compared to 2FGL, contribute to the high ratio of input model to 2FGL sources in some ROI, which demonstrates the need to rederive the source model.

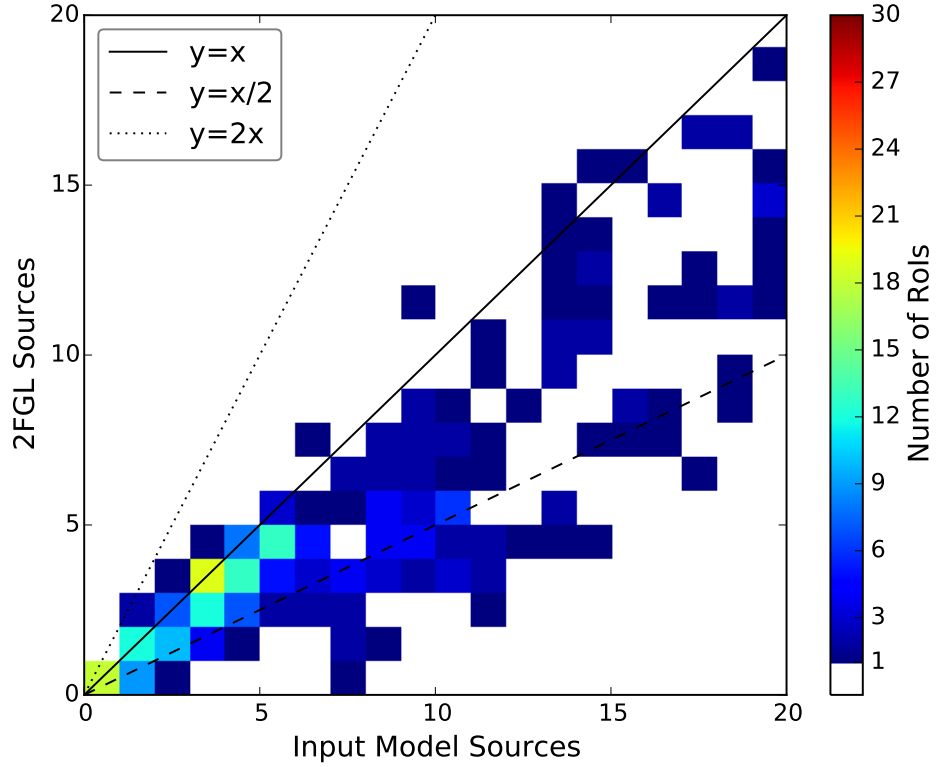


Figure 5.5: Comparison of the number of 2FGL sources with $\text{TS}_{1-100\text{ GeV}} \geq 25$ (excluding AGN and pulsars) with the number of newly added input model sources in the present analysis, for sources within 3° of the center of each ROI. The color scale shows the number of ROIs with a particular combination of numbers of 2FGL sources and new sources. White corresponds to no ROI with that combination of source counts.

To more accurately represent the 2FGL sources being reproduced in the central 3° , in Figure 5.6 we limited the input model sources to those within 0.2° (approximately the width of the core of the 10 GeV PSF) of a 2FGL source, effectively excluding input sources that are not co-spatial with a 2FGL source. Here we see that the majority of 2FGL sources have counterparts in the rederived set. As a

region’s complexity increases, seen as an increase in numbers of 2FGL sources, up to about half of the 2FGL sources may not have counterparts within 0.2° . Given that in these same regions we have more new sources than 2FGL sources, as seen in Figure 5.5, we find as expected that the longer data set with improved statistics at higher energies, where the angular resolution of the LAT is the best, allows us to add new sources to account for newly significant excesses in these complex regions. Additionally, sources with low TS in 2FGL are particularly susceptible to having a newly added source which may start at a similar position but then localize further than 0.2° from the 2FGL source.

Thus, we find that the method developed and used here produces a model which reproduces the 2FGL sources as expected, including differences that trend as anticipated given the longer data set and modified energy range, yielding better spatial resolution. The new method thus provides reasonable representations of the regions being modeled as input for the final analysis.

5.8 Detection Method

For each SNR, we characterize the morphology and spectrum of any γ -ray emission that may be coincident with the radio position reported in Green’s catalog. This was achieved by testing multiple hypotheses for the spatial distribution of γ -ray emission: a point source and two different algorithms for an extended disk. The best fit was selected based on the global likelihoods of the fitted hypotheses and their numbers of degrees of freedom. The hypothesis with the best global likelihood was then evaluated using a classification algorithm described in Acero et al. (2016) to determine whether the radio SNR could be associated with the detected γ -ray emission.

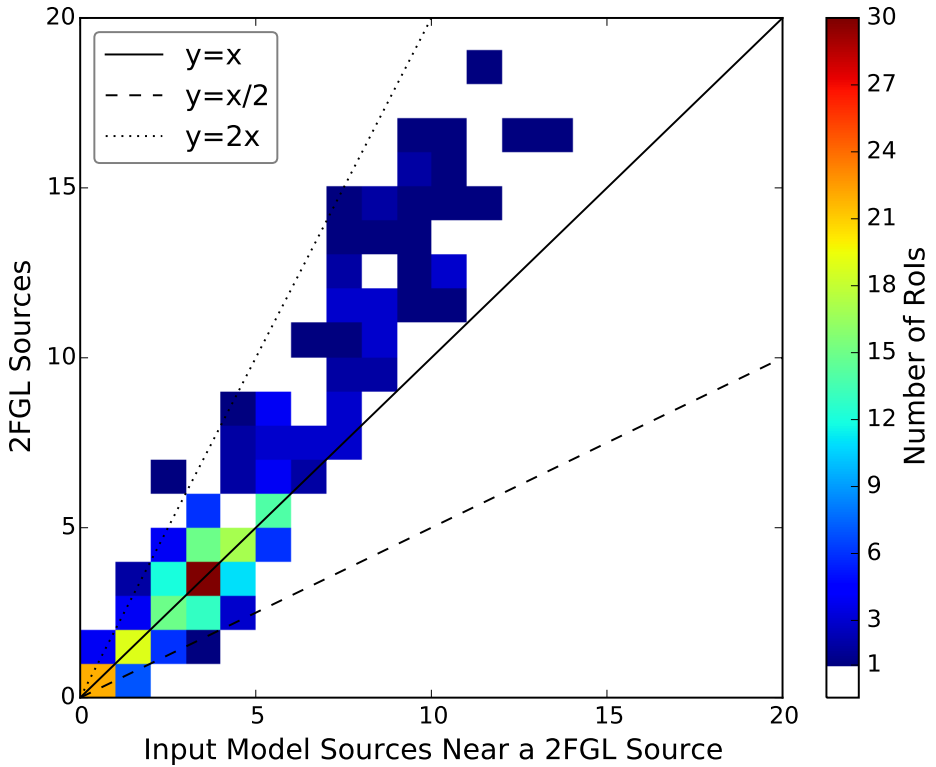


Figure 5.6: Same as Figure 5.5, including only input model sources lying within 0.2° of a 2FGL source.

Spatial coincidence is a necessary but not sufficient criterion to identify a γ -ray source with a known SNR. The detection of spatially extended γ -ray emission increases confidence in an identification, especially if GeV and radio sizes are similar, as has been observed on an individual basis for several extended SNRs (e.g. Lande et al. 2012). The LAT has sufficient spatial resolution to detect many Galactic SNRs as extended. Figure 5.7 shows the distribution of radio diameters from Green’s catalog. Vertical dashed lines show the minimum detectable extension for sources with flux and index typical of those observed in this catalog, based on simulations using the P7V6 IRFs (Lande et al. 2012). The minimum detectable extension depends not only on the source’s flux and spectrum, but also the flux of the background, which was estimated by scaling the average isotropic background level by factors

of 10 and 100 to be comparable to the Galactic plane. As figure 5.7 illustrates, roughly one third of the known Galactic SNRs may be resolved by the LAT if they are sufficiently bright GeV sources.

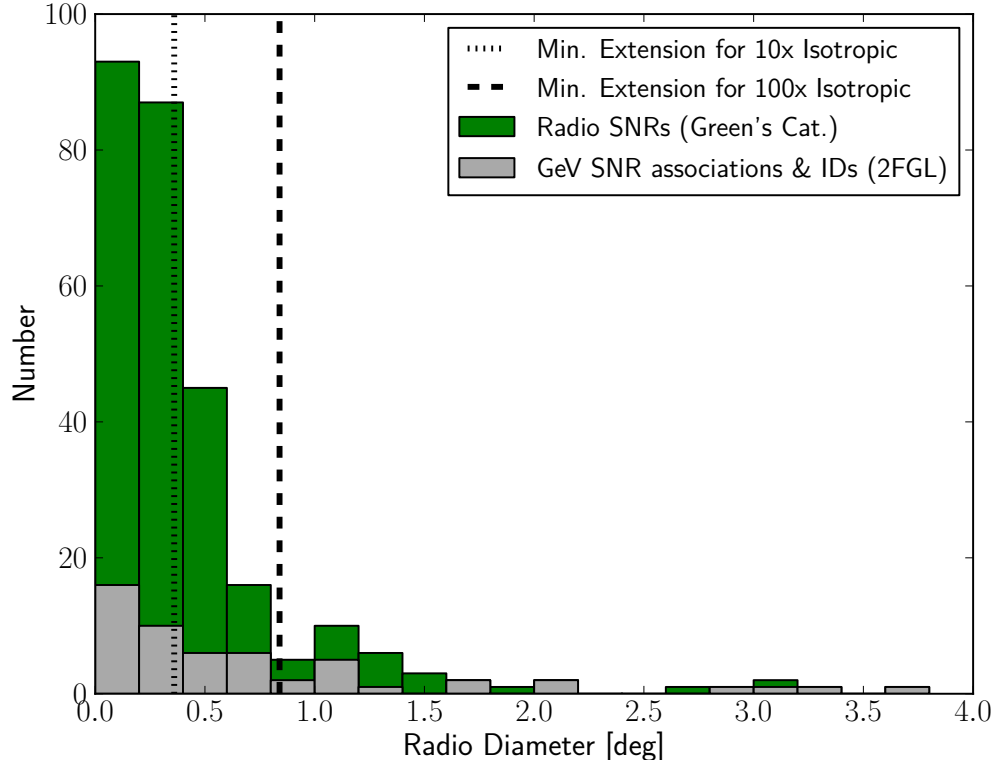


Figure 5.7: Distribution of SNR radio diameters from Green’s catalog. The vertical dashed lines indicate the minimum detectable extension for a source with a photon flux of $10^{-8} \text{ ph cm}^{-2} \text{ s}^{-1}$ in the $1 - 100 \text{ GeV}$ energy range and a PL index of -2.5 , from simulations of 2 years of data and the P7V6 IRFs (Lande et al. 2012). In that work, simulations using 10x and 100x the isotropic background level (thin-dotted and thick-dashed lines) are used to estimate a reasonable background range for sources in the Galactic plane.

In order to determine the best representation for each SNR, we analyzed each SNR-centered ROI using multiple hypotheses for the spatial and spectral form. We used `pointlike` (Kerr 2010) to compare PL and logP spectral forms, to compare point source versus extended source hypotheses, and to analyze the robustness of sources near the extended source.

For each hypothesis, we started with the input model described in Chapters 5.5 and 5.6. We removed sources falling within the SNR’s radio disk unless they had been identified as an AGN or pulsar, as described in Chapter 5.6. We then proceeded to evaluate the following point and extended source hypotheses. For the point source hypothesis, a point source with a PL index initialized to 2.5 was placed at the radio centroid of the SNR. The positions, spectral index, and spectral normalization of the point source were then fit. As for the initial input model described in Chapter 5.6, we tested the source for spectral curvature. To test the extended source hypothesis, we employed two separate procedures. Both employed a uniform disk model initially placed at the center of the RoI with a radius equal to that observed in the radio. In the first procedure, called the “disk” hypothesis, we fit both the position and extension of the disk, as well as tested for spectral curvature. A second procedure, which results in a model we call the “neardisk” hypothesis, additionally examines the significance of sources nearby the disk, removing those which are not considered independently significant and refitting the disk position and radius. This procedure is described in Chapter 5.8.1.

Having evaluated these hypotheses, we compared the global likelihood values of the final extended hypothesis and of the point source hypothesis to determine which model had the largest maximum likelihood. If the source is significant in the best hypothesis, the model parameters are reported as Tables 1 and 2 in Acero et al. (2016) . If no hypothesis had a significant γ -ray source coincident with the radio SNR, we calculated the upper limit on the flux from a region consistent with the radio SNR, described in Chapter 5.8.2, and report the results in Table 3 in Acero et al. (2016).

5.8.1 Localization, Extension, and Spectral Curvature

To test our hypotheses, we combined the initial model of point sources (Chapter 5.6) and the Galactic and isotropic diffuse contributions (Chapter 5.5 and 5.6) with a test source at the center of each RoI. All sources that fell within the radio SNR radius other than previously identified AGN or pulsars were removed, as was done for the input source model (Chapter 5.6). We note that multiple point sources removed within a single radio SNR radius may represent substructure within the source itself. This process conservatively assigns the majority of the flux to a single source, rather than decomposing it. We optimized the position of the test source with `pointlike`, iteratively allowing other model parameters to vary. For all hypotheses, the normalizations of all sources within 5° of the radio SNR center were fit while all other spectral parameters were fixed. The parameters for sources outside 5° were also fixed.

For the point source hypothesis, a point source was placed at the radio centroid of the SNR. For the disk hypothesis, a uniform disk with radius equal to the radio radius was placed at the center. In both hypotheses, the normalization, index, and position of the candidate source were fit. For the disk hypothesis, the extension was also fit. Previous analyses of a range of possible Galactic SNR sources with similar data sets (e.g. Lande et al. 2012) typically showed no differences in global likelihood significant enough to justify choosing a Gaussian over a uniform disk template or vice versa. In addition, there was typically little difference in spectral parameters for the two spatial forms. For simplicity and clarity, we thus test only the uniform disk hypothesis. We allowed the localization to wander up to 5° in the fits as a reasonable upper limit on what might later be associated with the SNR. This is roughly twice the radius of largest radio SNR.

We included an additional disk hypothesis in which we recalculated the significance of each nearby point source. Because neighboring sources can influence the best fit disk parameters, we iteratively evaluated the significance of the neighboring source by calculating $\text{TS}_{\text{nearby}}$, defined as twice the difference between the model’s log-likelihood ($\log \mathcal{L}$) with the nearby point source and the model without the source, as determined by `pointlike`. Starting from the fitted disk model, for each neighboring point source we refit the position, extension, normalization, and spectrum of the uniform disk after removing the source. A nearby source was considered to be significant and thus kept if $\text{TS}_{\text{nearby}} \geq 9$. Each point source was evaluated individually, starting with the closest point source and extending radially outward to all sources within 1° of the furthest edge of the SNR’s radio disk. The final result of this iterative process is called the “neardisk” hypothesis which, for cases where neighboring source(s) were removed, can have different best fit disk parameters. As a final step we refit the region with `gtlike`, using the neardisk model.

We chose the best extended source hypothesis by comparing the final disk and neardisk `gtlike` $\log \mathcal{L}$ values. Since the neardisk hypothesis can have fewer degrees of freedom, we chose the final disk hypothesis only if $2 \times (\log \mathcal{L}_{\text{disk}} - \log \mathcal{L}_{\text{neardisk}}) \geq 9$. Otherwise, we used the neardisk model as the final extended source hypothesis, hereafter referred to as the “disk hypothesis”.

In some cases a point source could not be localized starting at the SNR center. If the `pointlike` localization failed to converge when starting at the SNR center, we placed the candidate at the position of the most significant source removed from within the radio SNR radius and followed the procedure outlined above. For 69 RoIs there was either no source removed within the radio SNR or localization failed. For 31 RoIs, the candidate found had a $\text{TS} < 1$ and was removed from the model so as not to cause instabilities in the minimization. If the disk hypotheses converged and

the final candidate was significant ($\text{TS} \geq 25$) in both the localization and spectral fits, the best extended hypothesis was selected.

Prior to the final fit of the region, sources were tested for spectral curvature using $\text{TS}_{\text{bandfits}} - \text{TS}_{\text{PL}} \geq 25$. If this criterion was satisfied then we replaced the PL spectral model with a logP model and refit the RoI. The final spectral model was selected, as for the input model, by comparing the $\log \mathcal{L}$ values, in this case $\text{TS}_{\text{curve}} \geq 16$, as defined in Chapter 5.6. Seven sources were found to be significantly better fit by a logP spectrum. To obtain final spectral parameters, we performed a final fit using the standard likelihood analysis tool `gtlike`. The normalization and index parameters were constrained to lie within a physically reasonable range.

We determined the final RoI model by selecting the most likely hypothesis based on a comparison of the `gtlike` global $\log \mathcal{L}$ of the point source hypothesis with the most likely extended source hypothesis. An extended hypothesis was considered significantly more likely if TS_{ext} was ≥ 16 , where TS_{ext} is defined as twice the difference between the $\log \mathcal{L}$ of the final model from the disk hypothesis and that of the point source hypothesis, $\text{TS}_{\text{ext}} = 2(\log \mathcal{L}_{\text{disk}} - \log \mathcal{L}_{\text{point}})$, as in Lande et al. (2012). Otherwise, if the point source itself had $\text{TS} > 25$, we chose the point source hypothesis. In cases in which the optimization for the position of the point source did not converge but an extended disk was detected, we calculated the global $\log \mathcal{L}$ of the region without any source and with a point source at the center of the extended source. We then use the latter value to calculate TS_{ext} reported in Table 1 in Acero et al. (2016). For these candidates, if the source was significantly extended in both cases, we select the extended hypothesis. If none of the criteria were met, the candidate was considered undetected and we calculated an upper limit on the flux. Both the upper limits and flux calculation are described in the following subsection.

5.8.2 Fluxes and Upper Limits

Fluxes in the $1 - 100$ GeV band are determined using the standard analysis tool `gtlike` by a final fit of the model chosen to have the overall maximum likelihood characterization of the morphology and spectrum of the candidate source from the analysis detailed in Chapter 5.8 and 5.8.1. For those RoIs where no significant source was detected, we computed Bayesian upper limits on the flux using the method described in Helene (1983) excluding any overlapping sources in the model that have not been identified as AGN or pulsars, as described in Chapter 5.6. As a spatial model we used a uniform disk equal in position and radius to that reported in Green’s catalog. We assumed the spectral model to be a PL and report upper limits for indices of 2.0 and 2.5 at 95% and 99% confidence levels. The choice of indices was motivated by the distribution of PL indices for classified sources. The results are reported in Acero et al. (2016).

5.9 Catalog Results

We detected 102 candidates with a final source $\text{TS} \geq 25$ in the 279 SNR RoIs (see Chapter 5.8). Of the 102 detected candidates, 36 passed the association probability threshold (see Acero et al. (2016)). Of these, 30 SNRs ($\sim 11\%$ of the total) show significant emission for all alternative IEMs and are classified as likely GeV SNRs. An additional four were identified as sources which are not SNRs. Two other candidates were demoted to marginal due to their dependence on the IEM, as described in the next paragraph. Of the sources likely to be GeV SNRs, 17 show evidence for extension ($\text{TS}_{\text{ext}} > 16$). Only sources associated with SNRs G34.7–0.4 and G189.1+3.0 show evidence of significant spectral curvature in the $1 - 100$ GeV range and are fit with logP spectra. Of the classified candidates, four extended and 10 point SNRs

are new and published here for the first time. Descriptions of the new extended (G24.7+0.6, G205.5+0.5, G296.5+10.0, and G326.3–1.8) SNRs is given in Acero et al. (2016).

For those 245 SNRs that are either not detected by this analysis or which fail to meet the most stringent threshold for classification as a detected SNR, upper limits assuming the radio disk morphology of Green’s catalog with PL indices of 2.0 and 2.5 are reported in Table 3 in Acero et al. (2016). For those candidates which fail to meet the most stringent threshold, we replaced the source with the radio disk. We do not calculate upper limits for the four sources which are identified as not SNRs. A FITS version of the catalog is available through the *Fermi* Science Support Center, as described in Acero et al. (2016)⁵.

5.10 GeV Supernova Remnants in a Multiwave-length Context: Discussion Summary

As discussed in Chapter 2.1, the same population of radio, synchrotron-emitting CR electrons active in the shell of an SNR are expected to also produce γ -rays through the IC process and non-thermal bremsstrahlung radiation. If indeed the GeV and radio emission are produced in a single zone, it is reasonable to assume that the radio and γ -ray morphologies will correlate. We find that the best GeV diameter is within errors of the radio diameter for most of the candidates classified as being associated with an SNR, as shown in Figure 5.8. The same, co-spatial, electron population producing the GeV and radio emission is also suggestive of a potential correlation between the radio and γ -ray flux. Figure 5.9 shows the 1 GHz synchrotron flux versus the 1 GeV γ -ray flux for all SNRs. Various factors, such as the lack of

⁵http://fermi.gsfc.nasa.gov/ssc/data/access/lat/1st_SNR_catalog/

detailed non-thermal emission modeling, distance measurement errors, and use of oversimplified γ -ray spectral models can skew these results, obscuring any inherent correlation.

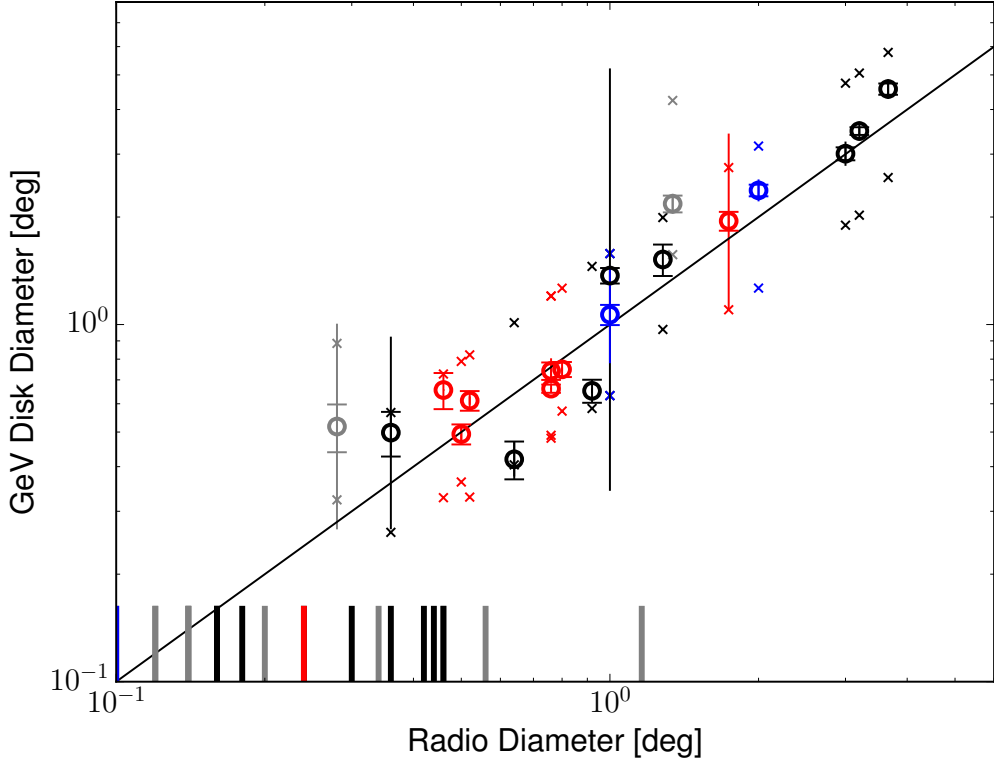


Figure 5.8: Radio diameters of Green’s catalog SNRs plotted against the fitted GeV diameters for those candidates with significant extension. The solid line represents equal radio and GeV diameters. All cases of detected extension have diameters greater than 0.2° . The ticks denote the radio extension of GeV point-like candidates, colored in order of their characteristics (young or interacting) and by their classifications (well defined or marginal). The small ‘x’s bracketing the points show the minimum and maximum GeV extensions allowed such that the source remains classified or marginally classified given the radio position and extension and best fit GeV position. Open circles indicate extended SNRs. All SNRs that passed classification are shown as black unless also classified as young, non-thermal X-ray SNRs (blue) or as interacting with MCs (red). Candidates that did not pass classification but that still had both fractional overlaps > 0.1 are gray. Statistical error bars have caps; error bars without caps represent the systematic error.

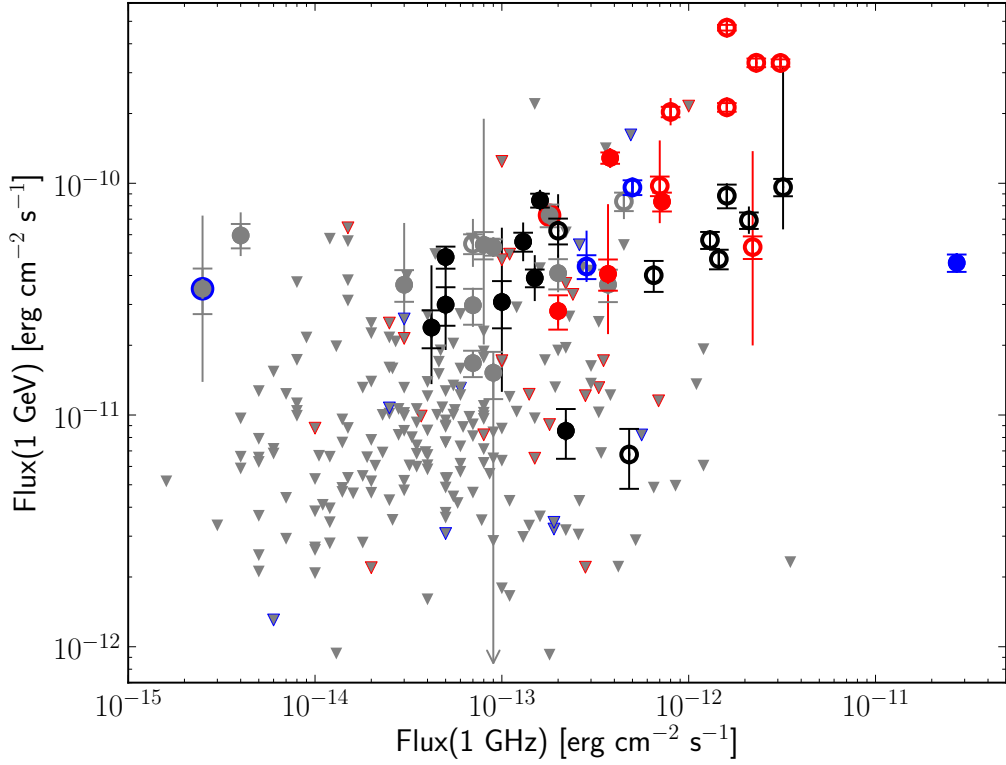


Figure 5.9: Comparison of γ -ray and radio spectral flux densities for all SNRs and candidates. For all SNRs that were not detected or which failed classification, grey triangles indicate upper limits at 99% confidence, computed assuming the radio location and extension. Symbols, colors, and error bars are as in Figure 5.8. In addition, filled circles indicate point-like sources, and if grey markers are also young or interacting, they are outlined in blue or red, respectively (No extended marginally classified candidates were also identified as young or interacting).

We test for one further relationship between the radio and GeV emission and the underlying particle populations through the measured radio and GeV spectral indices. The energy of synchrotron-emitting leptons traced by 1 GHz observations depends on the magnetic field. If radio and GeV emission trace the same underlying particle population, then, at energies below the maximum energy reached by the accelerated particles, the photon indices of radio and γ -ray emission should be correlated. For π^0 decay and e^\pm bremsstrahlung, the GeV and radio photon indices (Γ and α respectively) are related as $\Gamma = 2\alpha + 1$. For IC scattering leptons, the

GeV and radio photon indices follow $\Gamma = \alpha + 1$, or in the case in which high-energy leptons have been cooled via synchrotron or IC radiation, $\Gamma = \alpha + 3/2$ (Reynolds 2008). Figure 5.10 compares the deduced radio spectral index α with the 1–100 GeV photon index Γ .

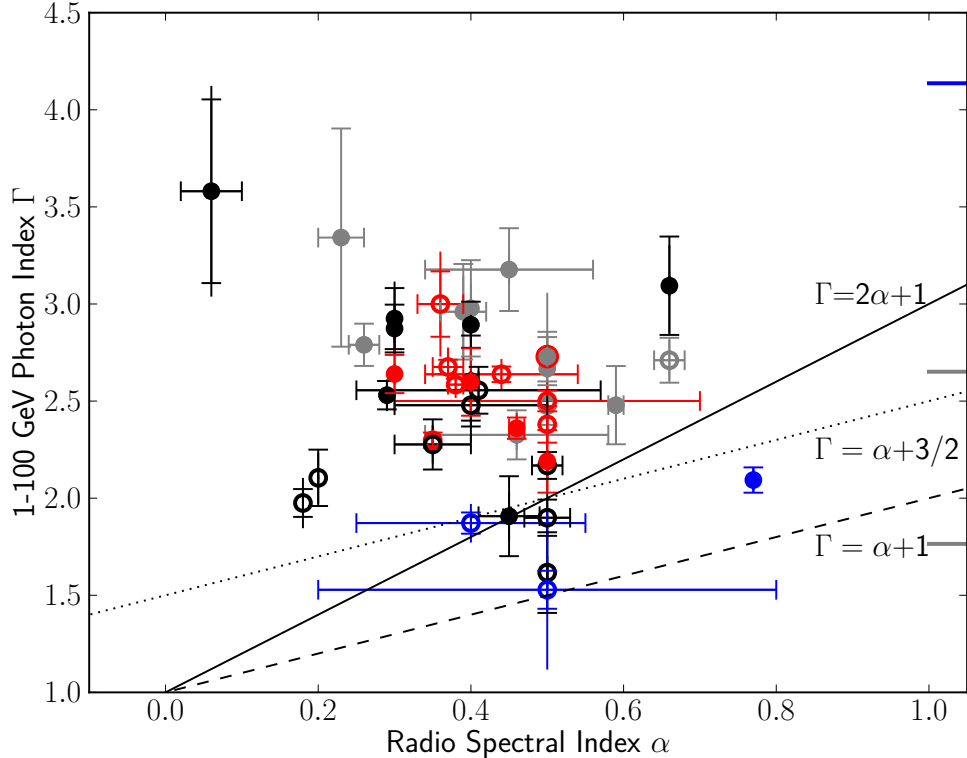


Figure 5.10: Comparison of radio spectral index, α , and GeV photon index, Γ . The expected correlations are plotted for π^0 decay or e^\pm bremsstrahlung (solid) and IC emission from an electron population that is freshly accelerated (dashed) or cooled by radiative processes (dotted). Emission via a combination of processes would fall between the lines (e.g. between the solid and dashed for a combination of π^0 decay and IC emission). Symbols, colors, and error bars are as in Figure 5.8; ticks along the right hand side show the 1 – 100 GeV photon indices of those SNRs without reported radio spectral indices.

Nearly all candidates have γ -ray photon indices that are softer than predicted given their radio spectra, regardless of the GeV emission mechanism. The three young SNRs in blue are most consistent with a single underlying particle population,

and it has been suggested they emit via IC (dashed line) at GeV energies. SNRs emitting via a combination of mechanisms under these simple assumptions would have indices falling between the two index relations, that is, they would lie in the region spanned by the π^0 /bremsstrahlung (solid) and IC (dashed) lines.

The lack of an observed correlation between the indices as expected under these simple assumptions suggests that more detailed physical models are required for the majority of SNR candidates. The observed soft GeV spectra relative to the radio has several potential explanations. The underlying leptonic and hadronic populations may have different PL indices. The emitting particle populations may not follow a PL but may instead have breaks or even differing spectral shapes. Finally, there may be different zones with different properties dominating the emission at different wavelengths.

In the SNRcat, we also compared the GeV and TeV properties of SNRs to test the second common assumption in SNR models: that momentum distributions of the emitting particle populations do not follow simple PLs but have curvature or breaks. Such changes in spectral slope could also cause breaks in the γ -ray spectra. As TeV emission may originate via the same processes as the *Fermi*-LAT-observed GeV emission (e.g. Funk et al. 2008; Tam et al. 2010; Tibolla 2009), we might expect to see such a change reflected in a spectrum combining *Fermi*-LAT data with observations from Imaging Air Cherenkov Telescopes (IACTs) such as the High Energy Stereoscopic System (H.E.S.S.), the Very Energetic Radiation Imaging Telescope Array System (VERITAS), and the Major Atmospheric Gamma-ray Imaging Cherenkov telescopes (MAGIC). The converse is also true, where detection predictions in the GeV based on simple PL extrapolation from the TeV have been borne out in GeV studies, e.g. identifications of H.E.S.S. sources from Tibolla (2009) in 2FGL (Nolan et al. 2012) and Ackermann et al. (2012a).

In Figure 5.11 we plot the PL index in the GeV versus TeV range for all SNRs observed with both *Fermi*-LAT and an IACT detections. Six of the ten SNR candidates have TeV indices that are softer than their GeV indices, while three have GeV and TeV indices that are consistent with each other, within statistical and systematic errors. The remaining interacting candidate has a somewhat softer index at GeV energies than at TeV. Such a hardening of the index from GeV to TeV suggests that another particle population may dominate at higher energies or that the emission mechanism may change between the GeV and TeV regimes. Such curvature in the spectrum may also explain the lack of a simple correlation between GeV and radio PL indices, as described above in this section. We also note that Figure 5.11 shows a distinct separation between young and interacting SNRs, which are often older. This suggests an evolution in index with age, from harder when younger to softer when older.

In Figure 5.12, we take SNR ages from the literature and plot the $1 - 100$ GeV photon index versus age. For our uniform sample of all GeV SNR candidates, young SNRs tend to have harder GeV photon indices than interacting SNRs, which are likely middle aged, though the scatter in age for the two classes is one to two orders of magnitude. The general trend of younger SNRs having harder indices may be due to the decrease of the maximum acceleration energy as SNRs age and their shock speeds slow down. This would also result in fewer particles being swept up by the shock front, given a constant density, suggesting a corresponding decrease in luminosity with age.

It is important to account for the distances of the SNRs when comparing physical quantities such as luminosity. Table 5.1 records distance from the literature, including the most recent and/or most certain distance estimates adopted in this work. Of the 279 SNRs studied, only 112 have published distance estimates. Most

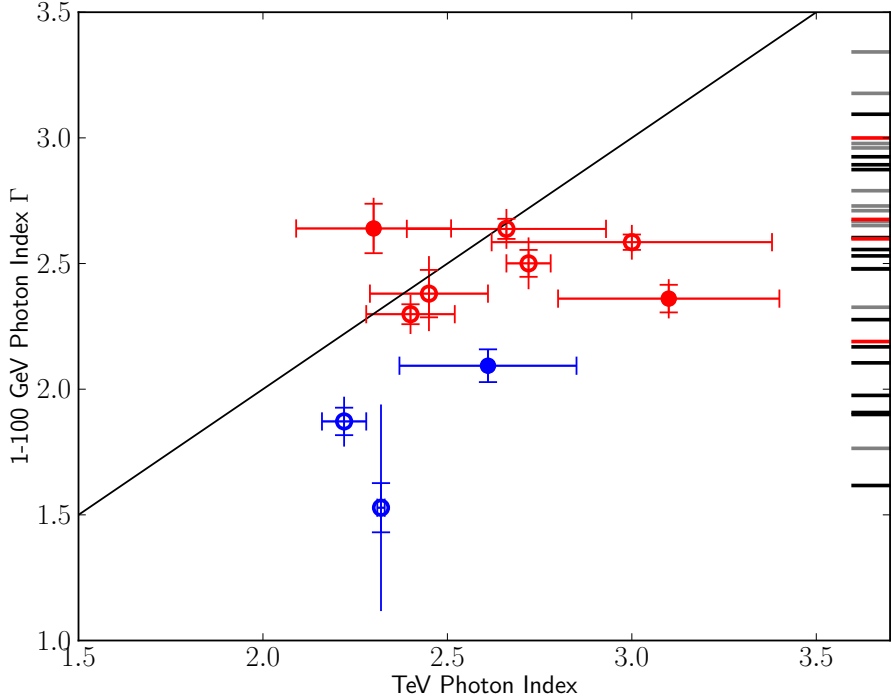


Figure 5.11: GeV index compared to published index measurements from IACTs. The line corresponds to equal index values. The predominance of SNRs below the line suggests spectral curvature, potentially reflecting a change in spectral slope of the underlying particle population(s') index or indices. The ticks represent the GeV candidates with indices in the range of those with a TeV counterpart but with no TeV measurements themselves, demonstrating the limitations of the data set. Symbols, colors, and error bars are as in Figure 5.8.

often these distances are determined from observed line-of-sight velocities using an assumed Galactic rotation curve. Furthermore, kinematic distance estimates have largely been done on an individual basis, and are not uniformly determined for all SNRs. We do not consider distances derived using the “ Σ -D relation” because SNRs show a wide range of physical diameters (D) for a given surface brightness (Σ), limiting the utility of such a relationship for determining the distances to individual SNRs (Green 2012).

Table 5.1. Distances to SNRs

Name	d [kpc]	Method	Reference(s)
G000.0+00.0	8.5	IAU value	Kerr & Lynden-Bell (1986)
G000.3+00.0	$8.5^{+3.0}_{-3.0}$	H I	Lang et al. (2010)
G000.9+00.1	$8.5^{+7.5}_{-1.5}$	PSR	Camilo et al. (2009b)
G001.0-00.1	8.5	Maser	Yusef-Zadeh et al. (1999)
G001.4-00.1	$8.5^{+5.6}_{-0.0}$	Maser	Yusef-Zadeh et al. (1999)
G004.5+06.8	$7.0^{+2.0}_{-0.6}$	H I	Reynoso & Goss (1999), Sankrit et al. (2005), Aharonian et al. (2008b)
G005.4-01.2	$4.75^{+0.45}_{-0.45}$	Maser	Hewitt & Yusef-Zadeh (2009)
G005.7-00.0	$8.4^{+5.3}_{-5.3}$	Maser	Hewitt & Yusef-Zadeh (2009)
G006.4-00.1	$1.9^{+0.4}_{-0.4}$	Maser, CO	Velázquez et al. (2002)
G008.7-00.1	4.5	Maser	Kassim & Weiler (1990)
G009.7-00.0	4.7	Maser	Hewitt & Yusef-Zadeh (2009)
G011.2-00.3	$5^{+21}_{-0.5}$	H I	Radhakrishnan et al. (1972), Becker et al. (1985), Green et al. (1988)
G012.8-00.0	$4.7^{+1.3}_{-1.1}$	PSR	Halpern et al. (2012)
G013.3-01.3	$3.3^{+1.8}_{-1.7}$	CO	Seward et al. (1995), Koralesky et al. (1998)
G015.1-01.6	$5.7^{+1.3}_{-3.5}$	NH	Boumis et al. (2008)
G015.4+00.1	$4.8^{+1.0}_{-1.0}$	CO	Castelletti et al. (2013)
G016.7+00.1	$10.0^{+3.7}_{-7.4}$	Maser, CO	Hewitt et al. (2008), Reynoso & Mangum (2000)
G016.8-01.1	$5.1^{+4.6}_{-1.8}$	H I	Sun et al. (2011)
G018.1-00.1	$5.58^{+0.24}_{-0.27}$	H I	Leahy et al. (2014)
G018.6-00.2	$4.6^{+0.6}_{-0.6}$	H I	Johanson & Kerton (2009)
G018.8+00.3	$12.0^{+3.0}_{-5.1}$	H I	Tian et al. (2007b)
G021.5-00.9	$4.7^{+0.4}_{-0.4}$	PSR	Camilo et al. (2006), Tian & Leahy (2008b)
G021.8-00.6	$5.35^{+0.15}_{-0.15}$	CO, PSR	Tian & Leahy (2008b), Zhou et al. (2009)
G023.3-00.3	$4.2^{+0.3}_{-0.3}$	H I, CO	Leahy & Tian (2008b), Tian et al. (2007c)
G027.4+00.0	$8.5^{+0.6}_{-1.0}$	H I	Tian & Leahy (2008a)
G028.6-00.1	$7.0^{+1.5}_{-1.0}$	H I, NH	Bamba et al. (2001)
G028.8+01.5	4.0	NH	Schwentker (1994), Misanovic et al. (2010)
G029.7-00.3	$7.8^{+2.8}_{-2.7}$	H I	Leahy & Tian (2008a)
G031.9+00.0	7.2	Maser	Frail et al. (1996)
G032.4+00.1	17	NH	Yamaguchi et al. (2004)
G032.8-00.1	$5.2^{+1.5}_{-0.4}$	Maser	Zhou & Chen (2011)
G033.6+00.1	$7.0^{+1.0}_{-0.5}$	H I	Giacani et al. (2009), Frail & Clifton (1989)
G034.7-00.4	3.0	Maser	Paron et al. (2009)
G035.6-00.4	$3.6^{+0.4}_{-0.4}$	H I	Zhu et al. (2013)
G039.2-00.3	$6.5^{+6.0}_{-0.3}$	CO	Hewitt et al. (2009a), Su et al. (2011)
G041.1-00.3	$10.3^{+2.5}_{-3.9}$	CO	Jiang et al. (2010)
G043.3-00.2	10^{+2}_{-2}	H I	Brogan & Troland (2001)
G049.2-00.7	$4.3^{+1.7}_{-0.0}$	Maser, H I	Koo & Moon (1997), Hewitt et al. (2009b), Tian & Leahy (2013)
G054.1+00.3	$7^{+2.0}_{-2.5}$	H I	Leahy et al. (2008)
G054.4-00.3	$3.0^{+0.8}_{-0.8}$	CO	Junkes et al. (1992), Caswell (1985)
G069.0+02.7	$1.5^{+0.6}_{-0.4}$	H I, PSR	Leahy & Ranasinghe (2012)
G073.9+00.9	$1.3^{+0.7}_{-0.8}$	NH	Lozinskaya et al. (1993)
G074.0-08.5	$0.58^{+0.06}_{-0.06}$	PM	Blair et al. (2009)
G074.9+01.2	$6.1^{+0.9}_{-0.9}$	H I	Kothes et al. (2003)
G076.9+01.0	$10.0^{+5.0}_{-4.0}$	NH	Arzoumanian et al. (2011)
G078.2+02.1	$2^{+2.0}_{-1.5}$	H I	Leahy et al. (2013), Ladouceur & Pineault (2008)
G089.0+04.7	$1.7^{+1.3}_{-1.0}$	CO	Byun et al. (2006)
G106.3+02.7	$0.8^{+1.2}_{-0.1}$	H I	Kothes et al. (2001)
G109.1-01.0	$3.2^{+0.2}_{-0.2}$	H I, CO	Kothes & Foster (2012)
G111.7-02.1	$3.4^{+0.3}_{-0.1}$	PM	Reed et al. (1995)
G114.3+00.3	$1.0^{+1.5}_{-0.3}$	H I	Yar-Uyaniker et al. (2004)
G116.5+01.1	1.6	H I	Yar-Uyaniker et al. (2004)
G116.9+00.2	$1.6^{+1.9}_{-0.0}$	H I	Yar-Uyaniker et al. (2004), Hailey & Craig (1994)
G119.5+10.2	$1.4^{+0.3}_{-0.3}$	H I	Pineault et al. (1993)
G120.1+01.4	$3.0^{+2.0}_{-0.6}$	H I	Tian & Leahy (2011), Hayato et al. (2010), Krause et al. (2008)
G127.1+00.5	$1.15^{+0.35}_{-0.25}$	H I	Pauls (1977), Xilouris et al. (1993), Leahy & Tian (2006)
G132.7+01.3	$2.2^{+0.2}_{-0.2}$	H I	Routledge et al. (1991)

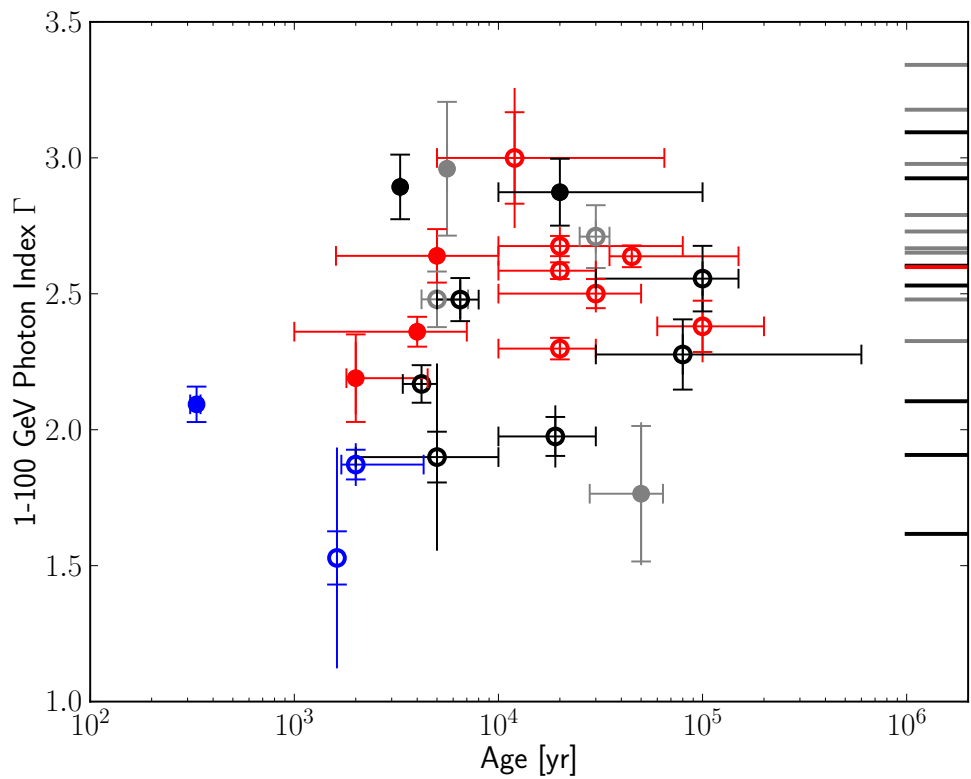


Figure 5.12: Age versus GeV spectral index. For those with ages in the literature, the young (blue) SNR candidates are separated in this phase space from the identified interacting candidates (red). The ticks on the right show indices for GeV candidates without well-established ages. Symbols, colors, and error bars are as in Figure 5.8.

To investigate the role of environment in the trends for the young and interacting SNRs, we examined the GeV luminosity versus radio diameter in Figure 5.13. The square of the physical diameter (D) can be regarded as a reasonable indicator for SNR age and environment (see 4.2), as its evolution during the Sedov-Taylor phase follows

$$D \propto n_0^{-1/5} E_{\text{SN}}^{1/5} t^{2/5} \quad (5.5)$$

where n_0 is the ambient density of the surrounding medium, E_{SN} is the supernova energy, and t is the age of the SNR (Sedov 1959; Taylor 1950b). We can thus use the physical diameter as an age proxy: “effective age”. Any apparent correlation between the luminosity and D^2 may be due to their inherent dependence on distance (squared). As observed in earlier works, e.g. Thompson et al. (2012), Figure 5.13 shows that, for the detected candidates, interacting SNRs are generally more luminous for a given physical diameter than young SNRs, though there is large scatter. This suggests that SNRs at the same effective age may be more luminous because they have encountered denser gas (n_0). It should also be noted that there is an explicit correlation between the luminosity and physical diameter plotted in Figure 5.13 as both are proportional to distance (squared), which is only reliably measured for a subset of our sample. Observational biases, including that young, often smaller and fainter SNRs tend to be more difficult to detect in the radio as well as in γ -ray, may also affect the observed trends.

5.11 Conclusions

In this Chapter, we have discussed the state of γ -ray observations of SNRs prior to the launch of *Fermi*, and the unique role that the LAT plays in identifying SNRs and exploring γ -ray production mechanisms therein. We presented the new automated

Table 5.1 (cont'd)

Name	d [kpc]	Method	Reference(s)
G156.2+05.7	$1.1^{+1.9}_{-0.8}$	NH	Pfeffermann et al. (1991), Gerardy & Fesen (2007)
G160.9+02.6	$0.8^{+3.2}_{-0.4}$	H I	Leahy & Tian (2007), Leahy & Roger (1991)
G166.0+04.3	$4.5^{+1.5}_{-1.5}$	H I	Landecker et al. (1989)
G180.0-01.7	$1.3^{+0.22}_{-0.16}$	PSR	Sallmen & Welsh (2004), Ng et al. (2007), Chatterjee et al. (2009)
G184.6-05.8	$1.93^{+0.57}_{-0.43}$	PM	Trimble (1973)
G189.1+03.0	1.5	Maser	Hewitt et al. (2006)
G205.5+00.5	$1.5^{+0.1}_{-0.7}$	H I	Odegard (1986), Fesen et al. (1985), Xiao & Zhu (2012)
G260.4-03.4	$2.2^{+0.3}_{-0.2}$	H I	Dubner & Arnal (1988), Paron et al. (2008)
G263.9-03.3	$0.287^{+0.017}_{-0.021}$	PSR	Moriguchi et al. (2001), Caraveo et al. (2001), Dodson et al. (2003)
G266.2-01.2	$0.75^{+0.15}_{-0.25}$	PM	Katsuda et al. (2008)
G272.2-03.2	$4.0^{+1.0}_{-2.2}$	NH	Lopez et al. (2011)
G284.3-01.8	3	CO	Ruiz & May (1986)
G290.1-00.8	$7^{+4.0}_{-3.5}$	H I	Rosado et al. (1996a), Slane et al. (2002), Reynoso et al. (2006)
G291.0-00.1	$5^{+1}_{-1.5}$	NH	Harrus et al. (1998)
G292.0+01.8	$6.2^{+0.9}_{-0.9}$	H I, PSR	Gaensler & Wallace (2003)
G292.2-00.5	$8.4^{+0.4}_{-0.4}$	PSR	Caswell et al. (2004), Camilo et al. (2000)
G296.5+10.0	$2.1^{+1.8}_{-0.9}$	H I	Giacani et al. (2000)
G304.6+00.1	$9.7^{+4.3}_{-1.7}$	H I	Caswell et al. (1975)
G308.4-01.4	$9.8^{+0.0}_{-3.9}$	NH	Prinz & Becker (2012)
G309.2-00.6	$4.0^{+1.4}_{-2.0}$	NH	Rakowski et al. (2001)
G315.1+02.7	$1.7^{+3.7}_{-0.3}$	PM	Stupar et al. (2007)
G315.4-02.3	$2.5^{+0.3}_{-0.2}$	PM	Rosado et al. (1996a), Sollerman et al. (2003a)
G315.9-00.0	8^{+2}_{-2}	PSR	Camilo et al. (2009a)
G316.3-00.0	$7.2^{+22.8}_{-2.5}$	H I	Caswell et al. (1975)
G318.2+00.1	$4.0^{+5.4}_{-0.7}$	H I	Hofverberg et al. (2010)
G320.4-01.2	$5.2^{+1.4}_{-1.4}$	H I, NH	Gaensler et al. (1999)
G321.9-00.3	$6^{+4.0}_{-0.5}$	H I	Stewart et al. (1993)
G326.3-01.8	$4.1^{+0.7}_{-0.7}$	NH	Rosado et al. (1996a), Kassim et al. (1993)
G327.1-01.1	$6.5^{+6.5}_{-1.5}$	NH	Sun et al. (1999)
G327.4+00.4	4.3	H I	McClure-Griffiths et al. (2001)
G327.6+14.6	$2^{+0.2}_{-0.4}$	PM	Nikolić et al. (2013)
G328.4+00.2	$17.4^{+2.6}_{-5.4}$	H I	McClure-Griffiths et al. (2001)
G330.2+01.0	4.9	H I	McClure-Griffiths et al. (2001)
G332.4-00.4	3.3	H I, CO	Paron et al. (2006), Reynoso et al. (2004)
G332.4+00.1	$7.5^{+3.5}_{-4.2}$	NH	Vink (2004)
G335.2+00.1	1.8	CO	Eger et al. (2011)
G337.0-00.1	11.0	Maser	Frail et al. (1996)
G337.2+00.1	$14.0^{+16.0}_{-0.5}$	H I, NH	Combi et al. (2005), Combi et al. (2006)
G337.2-00.7	$5.8^{+3.8}_{-3.8}$	H I	Rakowski et al. (2006), Lopez et al. (2011)
G337.8-00.1	12.3	Maser	Frail et al. (1996)
G338.3-00.0	$10.0^{+3.0}_{-2.0}$	H I	Lemiere et al. (2009)
G343.0-06.0	$1.0^{+0.5}_{-0.5}$	H I, NH	Kim et al. (2010), Welsh et al. (2003), Walker & Zealey (2001)
G346.6-00.2	11.0	Maser	Frail et al. (1996)
G347.3-00.5	$1.0^{+0.3}_{-0.2}$	H I, CO	Moriguchi et al. (2005)
G348.5+00.1	$9^{+0.5}_{-2.7}$	H I	Tian & Leahy (2012)
G348.5-00.0	$6.3^{+3.4}_{-3.3}$	Maser	Tian & Leahy (2012)
G348.7+00.3	13.2	H I	Tian & Leahy (2012)
G349.7+00.2	$11.5^{+0.7}_{-0.7}$	Maser	Frail et al. (1996), Tian & Leahy (2014)
G350.1-00.3	$4.5^{+6.2}_{-0.5}$	H I	Gaensler et al. (2008)
G351.7+00.8	$13.2^{+0.5}_{-11.1}$	H I	Tian et al. (2007a)
G352.7-00.1	$7.5^{+0.9}_{-0.7}$	H I, CO	Giacani et al. (2009)
G353.6-00.7	$3.2^{+0.8}_{-0.8}$	H I, CO	Tian et al. (2008)
G357.7+00.3	6.9	Maser	Frail et al. (1996)
G357.7-00.1	12	Maser	Frail et al. (1996), Gaensler et al. (2003), Lazendic et al. (2004)
G359.1-00.5	4.6	Maser	Yusef-Zadeh et al. (2007), Hewitt et al. (2008)

Note. — Table of SNR distances drawn from the literature. The method for determining the distance is noted as: CO = line-of-sight velocity from molecular CO lines; H I = kinematic distance from H I absorption; NH = extinction estimate from optical or X-rays; Maser = kinematic distance from OH maser velocity; PM = Proper motions; PSR = association with pulsar. The d_{error} values indicate the range of uncertainties from the quoted distance values as assessed in the cited publications. The distance uncertainties are often asymmetric.

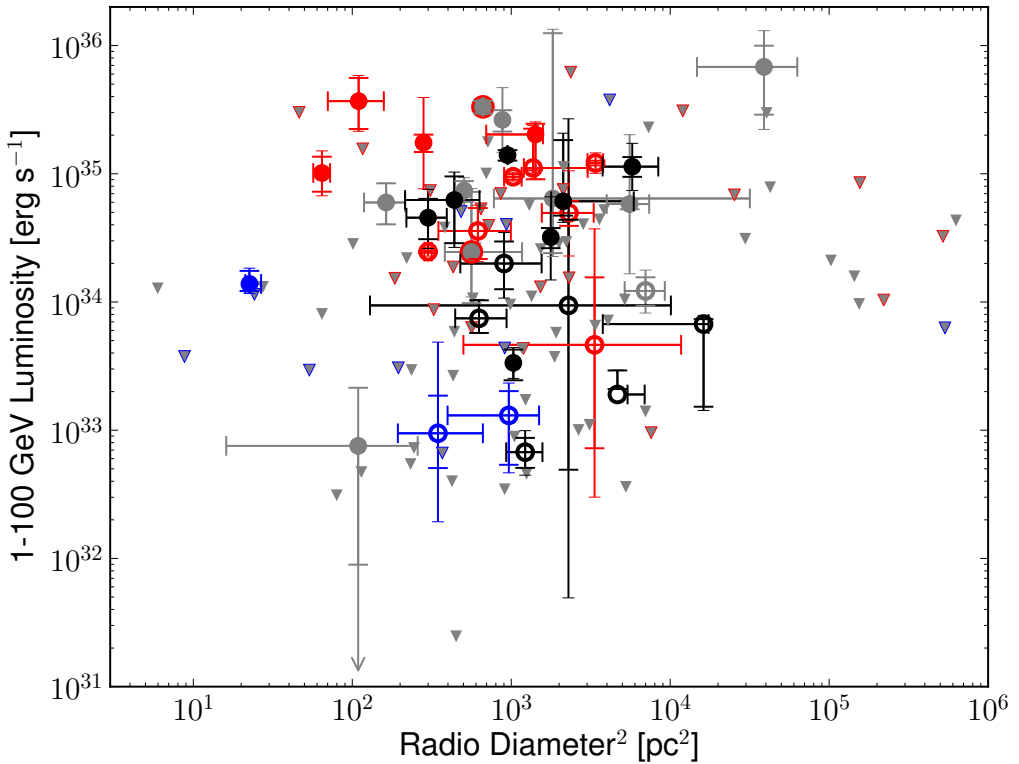


Figure 5.13: The $1 - 100$ GeV luminosity is plotted against the square of the radio diameters in pc of those SNRs with known distances. Symbols, colors, and error bars are as in Figure 5.8.

source addition and analysis method, `addSrcs`, and its application to studying the population of SNRs emitting GeV γ -rays, published in Acero et al. (2016). With this first *Fermi*-LAT SNR Catalog we have systematically characterized GeV emission in regions containing known radio SNRs, creating new methods to address issues associated with these typically complex regions. These include methods for systematically adding sources to a region and better estimating the systematic error due to choice of interstellar emission model (discussed in detail in)Acero et al. (2016)). From this, we have determined characteristics of the GeV SNR population, down to our measurement limit, finding 30 classified and 14 marginal candidates with a false identification limit of <22%(Acero et al. 2016). This GeV data provide a

crucial context for the detailed modeling of individual SNRs. In combination with multiwavelength measurements, the GeV data now challenge simple, previously sufficient SNR emission models. Within the limits of existing multiwavelength data, our observations generally support previous findings of changes in spectral slope at or near TeV energies and a softening and brightening in the GeV range with age and effective age, yet we see indications that new candidates and new multiwavelength data may provide evidence of exceptions to this trend.

Chapter 6

Extended Source Detection above 50 GeV: The 2FHL Catalog

6.1 Introduction

The LAT (Atwood et al. 2009) on board the *Fermi* γ -ray space telescope has been surveying the whole sky since August 2008. Its unprecedented sensitivity and localization accuracy allowed the detection of over 3,000 point-like sources in 4 years of data (see the third catalog of *Fermi*-LAT sources, 3FGL, Acero et al. 2015b). Typically, *Fermi*-LAT catalog studies are based on source detection and characterization in the whole 0.1 GeV–100 GeV energy band. The larger photon statistics present at low energy, counterbalanced by the LAT point-spread function (PSF) whose size decreases with energy, yields an optimum sensitivity at a energies of a few GeV. The *Fermi*-LAT catalogs are thus representative of the GeV sky more than they are of the MeV or the sub-TeV sky.

The first *Fermi*-LAT catalog of hard sources, named 1FHL (Ackermann et al. 2013c), provided an unbiased census of the sky at energies from 10 GeV up to

500 GeV. All-sky surveys at γ -ray energies are instrumental for ground-based imaging atmospheric Cherenkov telescopes (IACTs) such as H.E.S.S., MAGIC, and VERITAS (Hinton 2004; Holder et al. 2009; Lorenz 2004, respectively) in order to find new sources because of their limited fields of view (FoV).

Recently, a new event-level analysis (known as Pass 8) has been developed by the *Fermi*-LAT collaboration (Atwood et al. 2013a,b). Pass 8 significantly improves the LAT's background rejection, PSF, and effective area. All these enhancements lead to a significant increase of the LAT sensitivity and its effective energy range, from below 100 MeV to beyond a few hundred GeV (Atwood et al. 2013a,b). These improvements are particularly significant above 50 GeV, yielding an enhancement in the acceptance and PSF by a factor between 1.2 and 2. It is interesting to note that, above 50 GeV, both the PSF (governed mostly by the pitch of the tracker silicon strips and the spacing of the tracker planes, see Chapter 3.2) and the effective area of the LAT are only weakly dependent on energy and that the LAT operates, due to the (almost complete) absence of background, in the photon-limited regime.

We use 80 months of Pass 8 data to produce a catalog of sources detected by the LAT at energies¹ between 50 GeV and 2 TeV. This constitutes the second catalog of hard LAT sources, named Second Catalog of Hard *Fermi*-LAT Sources (2FHL), which allows a thorough study of the properties of the whole sky in the sub-TeV domain. In this thesis, we present results published in Ackermann et al. (2016), exclusively focusing on the Galactic science analysis and results and leave the extragalactic results to the published 2FHL paper .

¹Note the different energy range with respect to the 1FHL.

6.2 Analysis

6.2.1 Data Selection

We use 80 months (from August 2008 to April 2015) of P8_SOURCE photons with reconstructed energy in the 50 GeV–2 TeV range. At these energies the LAT has an energy resolution of around 10–15 % (1σ). Photons detected at zenith angles larger than 105° were excised to limit the contamination from γ -rays generated by cosmic-ray interactions in the upper layers of the atmosphere. Moreover, data were filtered removing time periods when the instrument was not in sky-survey mode². This leaves approximately 61,000 photons detected across the entire the sky. The count map reported in Figure 6.1 shows that the LAT observes many point-like sources and large scale diffuse emission in the direction of our Galaxy, some of which appears coincident with the so-called *Fermi* bubbles (Ackermann et al. 2014; Su et al. 2010).

6.2.2 Source Detection

The first step of the source detection stage comprises the identification of source seeds, which are locations of potential sources whose significance is later tested through a maximum likelihood (ML) analysis. The seed detection method, described further in Ackermann et al. (2016), includes all the point sources detected in the 1FHL catalog. We note that this seed list may include statistical fluctuations as well as real sources with a non-optimal position.

A full ML analysis is then performed in order to verify which, among the seeds, are the reliable sources. The analysis is performed in 154 RoIs, varying between 10°

²This was achieved using the expression ‘(DATA_QUAL>0)&&(LAT_CONFIG==1)’ in `gtmktime`.

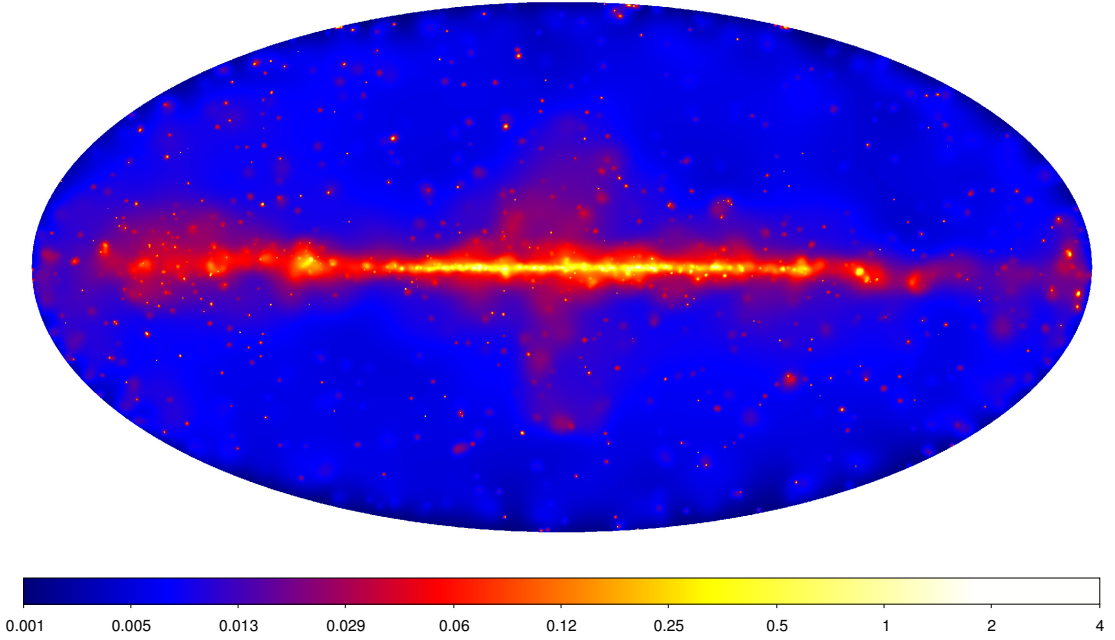


Figure 6.1: Adaptively smoothed count map in the 50 GeV–2 TeV band represented in Galactic coordinates and Hammer-Aitoff projection. The image has been smoothed with a Gaussian kernel whose size was varied to achieve a minimum signal-to-noise ratio under the kernel of 2. The color scale is logarithmic and the units are counts per $(0.1 \text{ deg})^2$.

and 20° in radius, whose sizes and positions in the sky are optimized to cover all the seeds, ensuring that no more than 45 seeds are contained in a single ROI. For each ROI, we build a sky model that includes all the potential sources in the region as well as the Galactic and isotropic diffuse emissions³. These models, which are defined only up to ~ 600 GeV and ~ 900 GeV respectively, where extrapolated up to 2 TeV. The ROI models include also the extended sources present in the region (see Chapter 6.3). The model is fit to the data via the unbinned ML algorithm provided within the *Fermi* Science Tools⁴ (version v9r34p3).

³We used the `gll_iem_v06.fits` and `iso_P8R2_SOURCE_V6_v06.txt` templates available at <http://fermi.gsfc.nasa.gov/ssc/data/access/lat/BackgroundModels.html>.

⁴Available at <http://fermi.gsfc.nasa.gov/ssc/data/analysis/software/>.

The spectrum of each source is modeled with a power law because none of the sources is expected to show statistically significant spectral curvature detectable by the LAT in this energy band. Indeed, this was the case for the sources in the 1FHL catalog (Ackermann et al. 2013c).

The fit is performed iteratively in order to ensure convergence and to produce an optimal solution. It proceeds as follows:

1. Complex ML fits require approximate knowledge of the starting values of the parameters. For this reason the first step aims to find those values by fitting each single source separately to determine approximate spectral parameters. Throughout the entire process, the parameters of the diffuse emission models are left free to vary. The significance of each source is evaluated using the test statistic $TS = 2(\ln \mathcal{L}_1 - \ln \mathcal{L}_0)$, where \mathcal{L}_0 and \mathcal{L}_1 are the likelihoods of the background (null hypothesis) and the hypothesis being tested (e.g. source plus background). At each step in the procedure, marginal sources, those with $TS < 10$, are removed from the model. Once the spectral parameters and significance of each source have been evaluated, a global fit for which all the parameters of the sources with a $TS \geq 10$ are allowed to vary is performed. Then one more global fit is performed after removing all the sources that had $TS < 10$ at the previous global fit. This step, as well as all the others, includes sources that are spatially extended (see Chapter 6.3);
2. In this second step, the positions of point-like sources, using the best-fit sky model derived at step 1, are optimized using the `gtfindsrc` tool. This step is done iteratively as well by optimizing first the positions of the most significant sources found at step 1 and later those of the fainter ones;
3. The parameters and significances of sources are estimated again (as in step 1)

using the best-fit source positions. This step produces the best-fit sky model for any given RoI. Seeds with $10 \leq \text{TS} < 25$ are included in the model, but not reported in the final catalog;

4. For each source we estimate the energy of the highest-energy photon (HEP) that the fit attributes robustly to the source model. This is done using the tool `gtsrcprob` and selecting the HEP that has a probability $> 85\%$ to belong to the source;
5. A spectrum with three logarithmically spaced bins (boundaries of 50 GeV, 171 GeV, 585 GeV, 2 TeV) is generated for each source in the RoI that is detected with $\text{TS} \geq 25$ and with the number of detected γ rays (estimated by the likelihood, N_{pred}) to be ≥ 3 .

The procedure described above achieves the detection of 360 sources (including the extended sources discussed next in Chapter 6.3) with $\text{TS} \geq 25$ and $N_{\text{pred}} \geq 3$ across the entire sky. The number of seeds kept in the RoI models with $10 \leq \text{TS} < 25$ is 453, while 7 are seeds with $\text{TS} \geq 25$, but $N_{\text{pred}} < 3$.

6.3 Search for Spatially-Extended Sources

Preliminary runs of the source detection method described in Chapter 6.2.2 detected clusters of point sources in the Galactic plane, which were suggestive of spatially extended sources. It is also possible that clusters of seed sources, each with sub-detection-threshold significance, could be detected as a significant extended source. Not modeling extended γ -ray emission as such can lead to inaccurate measurements of spectral and spatial properties of both the extended source and neighboring point sources, particularly in the Galactic plane (Lande et al. 2012). Most of the TeV

sources in the Galactic plane are spatially extended (Carrigan et al. 2013; Ong 2013), so to clearly connect LAT detections spectrally to these sources, extension detection and characterization is important. In the following, we distinguish between sources whose extension have been previously determined with *Fermi*-LAT and new extended sources that are reported for the first time in a LAT catalog. The details of all significantly detected extended sources are reported in Chapter 6.4.4.

6.3.1 Extended Sources Previously Detected by the LAT

We explicitly modeled sources as spatially extended when a previous, dedicated, analysis found the source to be resolved by the LAT. The 25 extended sources reported in 3FGL were included in our model using the spatial templates derived in the individual source studies (see references in Acero et al. 2015b). Refitting the positions and extensions of the 3FGL extended sources in this energy range is beyond the scope of this work.

Of the 25 3FGL extended sources, 19 are significantly detected here above the detection threshold ($TS \geq 25$). Only 6 sources are not detected and, since all have $TS < 10$, are removed from the sky model (see Chapter 6.4.4 for details).

One extended LAT source has had a dedicated analysis published since the release of the 3FGL catalog. Abramowski et al. (2015a) reported joint H.E.S.S. and LAT observations of the very high energy (VHE) source HESS J1834-087. This source is coincident with SNR W41 and was detected as spatially extended in a wide energy range spanning 1.8 GeV to 30 TeV. In this paper, we employ the spatial model for the GeV emission determined in Abramowski et al. (2015a), leading to a significant detection of this source.

6.3.2 Newly Detected Extended Sources

In addition to modeling the extended sources mentioned in Chapter 6.3.1, we performed a blind search of the Galactic plane ($|b| < 10^\circ$) to identify potential extended sources not included in previously published works. Our analysis pipeline is similar to that used in Acero et al. (2016) (described in detail in Chapter ??), with some modifications tailored to searching for multiple extended sources in an ROI. The pipeline employed the `pointlike` binned maximum likelihood package (Kerr 2010), in particular utilizing the extended source fitting tools validated by Lande et al. (2012) to simultaneously fit the position, extension, and spectra of sources in our ROIs. We used the `addSrcs` method (developed for the SNRcat and described in Chapter 5.6) to characterize potentially extended sources across the Galactic plane. We detail how it was applied to the 2FHL study below.

We created 72 ROIs of radius 10° , centered on $b = 0^\circ$ with neighboring ROIs overlapping and separated by 5° in Galactic longitude. Our initial model of the γ -ray emission in each ROI consisted solely of the Galactic diffuse (allowing just the normalization to be fit) and isotropic emission models (fixing the normalization), with no other sources in the ROI. Emission in the ROIs was further characterized by iteratively adding sources and fitting their spectral parameters (normalization and spectral index) in a $14^\circ \times 14^\circ$ region.

A TS map that included all significant sources found previously, made up of $0.1^\circ \times 0.1^\circ$ bins across the ROI, was created at each iteration and a small radius (0.1°) uniform disk, with a power-law spectrum was placed at the position of the peak TS pixel. The spectra of any newly added sources, as well as the position, extension, and spectral parameters of the disk were then fit. If $TS_{\text{ext}} \geq 16$, where $TS_{\text{ext}} = 2 \log(\mathcal{L}_{\text{ext}}/\mathcal{L}_{\text{ps}})$ (i.e. twice the log-likelihood ratio of an extended to a point

source, Lande et al. 2012), then the disk was kept in the model. For $\text{TS}_{\text{ext}} < 16$, the extended source was replaced by a point source with a power-law spectral model. For the point-source replacement case, spectral parameters of sources in the ROI were fit and the position of the new point source was optimized. Finally, the spatial parameters of any previously added extended sources were refit iteratively before creating a new TS map and repeating the process. We stopped adding sources when the peak TS was less than 16 for two successive sources.

To assess the impact of fitting extended sources when starting with an ROI devoid of sources, a crosscheck analysis (also using `pointlike`) was performed across the Galactic plane. We included 3FGL point and extended sources, the Galactic diffuse and isotropic emission, and pulsars from the 2PC catalog (Abdo et al. 2013) (as well as from 3FGL) in the preliminary source model for each region. Sources were iteratively added to account for residual emission and both these residual sources and 3FGL sources were tested for extension. Remarkably, this alternative analysis converges (i.e. spectral and spatial parameters for the detected extended sources are compatible in both analyses) to the initially source-devoid analysis for nearly all detected extended sources.

Extended sources detected in the analysis described in this chapter for which the position and extension were compatible with those found by the crosscheck were included in the ROI model at step 1 of the full ML analysis detailed in Chapter 6.2.2. Seed point sources interior to the extended sources were removed prior to the ML fit. Since any source that had $\text{TS}_{\text{ext}} < 16$ reverted to a point source model, `addSrcs` characterized both extended and point-like emission in each ROI. While the extended source results were passed into the ML fit, the point source results derived with `pointlike` were not included. Despite their non-inclusion, the point source results were cross-checked against the final results of the ML procedure to

ensure there were no glaring inconsistencies, of which none were found.

To address the ambiguity between detecting a source as spatially extended as opposed to a combination of point sources, we utilized the algorithm detailed in Lande et al. (2012) to simultaneously fit the spectra and positions of two nearby point sources. $\text{TS}_{2\text{pts}}$ is defined as twice the log of the ratio of the likelihood for the region containing two point sources to the same region with a single point source, $\text{TS}_{2\text{pts}} = 2\log(\mathcal{L}_{2\text{pts}}/\mathcal{L}_{\text{ps}})$. We only consider a source to be extended if $\text{TS}_{\text{ext}} > \text{TS}_{2\text{pts}}$. Since the extended and two point source hypotheses are not nested models, a likelihood-ratio test cannot be used to quantitatively compare $\text{TS}_{2\text{pts}}$ with TS_{ext} to determine which is the more significant model. Despite this, Lande et al. (2012) showed through Monte Carlo simulations that comparing the two likelihood ratios is a strong test for determining if the detected emission truly arises from two point sources, and that it is unlikely to incorrectly favor the two-point hypotheses if a source is extended. We only consider a source to be extended if $\text{TS}_{\text{ext}} > \text{TS}_{2\text{pts}}$.

Our blind search of the Galactic plane allowed us to find 5 sources not previously detected as extended by *Fermi*-LAT. Further details on these sources are presented in Chapter 6.4.4.

6.4 The 2FHL Catalog

The 2FHL catalog⁵ includes 360 sources detected over the whole sky, each with a likelihood test statistic of $\text{TS} \geq 25$ and number of associated photons, $N_{\text{pred}} \geq 3$. The source association procedure (detailed in Ackermann et al. (2016)) finds that 75% of the sources in the catalog (274 sources) are extragalactic⁶, 11% (38 sources)

⁵FITS catalog can be found at <http://fermi.gsfc.nasa.gov/ssc/data/access/lat/2FHL/>

⁶This includes N 157B, an extragalactic PWN.

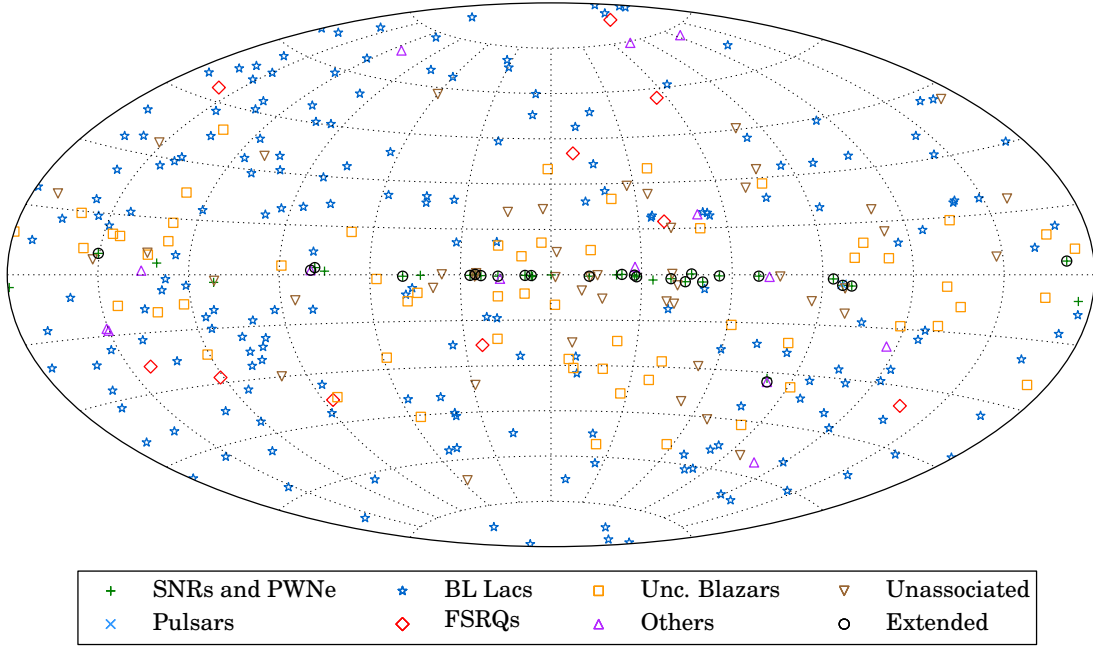


Figure 6.2: Sky map, in Galactic coordinates and Hammer-Aitoff projection, showing the sources in the 2FHL catalog classified by their most likely association.

are of Galactic nature, and 13% (48 sources) are unassociated (or associated with a TeV source of unknown nature). The unassociated sources are divided between 23 sources located at $|b| < 10^\circ$, and 25 sources at $|b| \geq 10^\circ$. Therefore the fraction of extragalactic sources in the sample is likely larger than 80 %. The number of 2FHL sources that have not been reported in 3FGL is 57, 47 of which have not been previously reported in any LAT catalog nor in the TeVCat⁷ catalog of TeV detected sources, and are thus new γ -ray sources. Figure 6.2 shows the location of 2FHL sources, color-coded according to their source class.

⁷<http://tevcat.uchicago.edu/>

6.4.1 General Characteristics of 2FHL Sources

The 2FHL sources have > 50 GeV fluxes ranging from $\sim 8 \times 10^{-12}$ ph cm $^{-2}$ s $^{-1}$ to $\sim 1.3 \times 10^{-9}$ ph cm $^{-2}$ s $^{-1}$ with a median flux of 2.0×10^{-11} ph cm $^{-2}$ s $^{-1}$ and a median spectral index of 2.83. The index uncertainty increases rapidly with the spectral index (e.g. the uncertainty is about ± 0.5 for sources with $\Gamma = 2$ whereas it is ± 2 for sources with $\Gamma = 5$). Half of the sources are localized to better than 1.7' radius at 68 % confidence. The distributions of spectral indices and the highest photon energy reported in Figure 6.3 show that extragalactic sources tend to have larger photon indices (median of 3.13) than Galactic sources (median of 2.10). Because of the harder spectra, Galactic sources tend to have higher-energy HEPs than those of extragalactic sources as shown as well in Figure 6.3. It is interesting to note that unassociated sources have a median index of 2.22 (2.00 for sources at $|b| < 10^\circ$ and 2.96 for those at $|b| \geq 10^\circ$), showing that a fraction (see Chapter 6.4.2) of unassociated sources are likely of Galactic origin.

Building a spectral energy distribution (SED) represents a powerful way to discriminate or infer the nature of a source. By combining the spectral data from the 3FGL, 1FHL, and 2FHL catalogs, it becomes possible to measure the SEDs of sources over four decades in energy. Although these catalogs rely on different exposures and most γ -ray sources are variable, these data allow us to characterize the high-energy peak of their broadband SEDs. The SEDs of a few notable sources will be shown in the next sections.

6.4.2 The 2FHL Galactic Source Population

The narrow PSF core (about 0.1°) and moderate Galactic diffuse emission (in comparison with the > 100 MeV band) allows the LAT to characterize and study well the emission of sources in the plane of our Galaxy above 50 GeV. Within $|b| < 10^\circ$, LAT has detected 103 sources. Of those, 38 sources are associated with Galactic sources, 42 with blazars, 14 are unassociated and 9 are associated with other γ -ray sources whose origin is not known (see below). Figure 6.4 shows cut-outs of the Galactic plane with all detected sources labeled.

Among the 38 Galactic sources, 16 are spatially coincident with SNRs, 13 are coincident with PWNe, 4 are associated with PWN/SNR complexes and the other 5 sources are X-ray binaries (3), one pulsar (PSR J0835–4510) and the Cygnus Cocoon. It is clear that the majority of Galactic sources detected above 50 GeV are associated with objects at the final stage of stellar evolution.

Galactic sources display on average hard spectra, which is a sign of efficient particle acceleration. Roughly 55% of all Galactic sources have a spectral index lower than 2.2. For comparison, only 14% of the 2FHL blazars display such hard spectra. A sizable fraction (approximately 25%, see Figure 6.3, upper panel) of Galactic sources has a photon index harder than 2, implying a high-energy SED peak in the TeV band. Indeed, as the lower panel of Figure 6.3 shows, LAT detects emission from many Galactic sources well beyond 500 GeV. All PWNe detected by *Fermi* are found to be powered by young and energetic pulsars (age $\lesssim 30$ kyr, Acero et al. 2013). While it is common for PWNe to show hard spectra, this is less so for SNRs whose majority (about 85 %) display softer spectra (Acero et al. 2016). Hard-spectrum SNRs are typically young or mid-aged ($\lesssim 3\text{--}5$ kyr) and might be difficult to find in radio surveys. Thus, Galactic surveys at above 50 GeV have

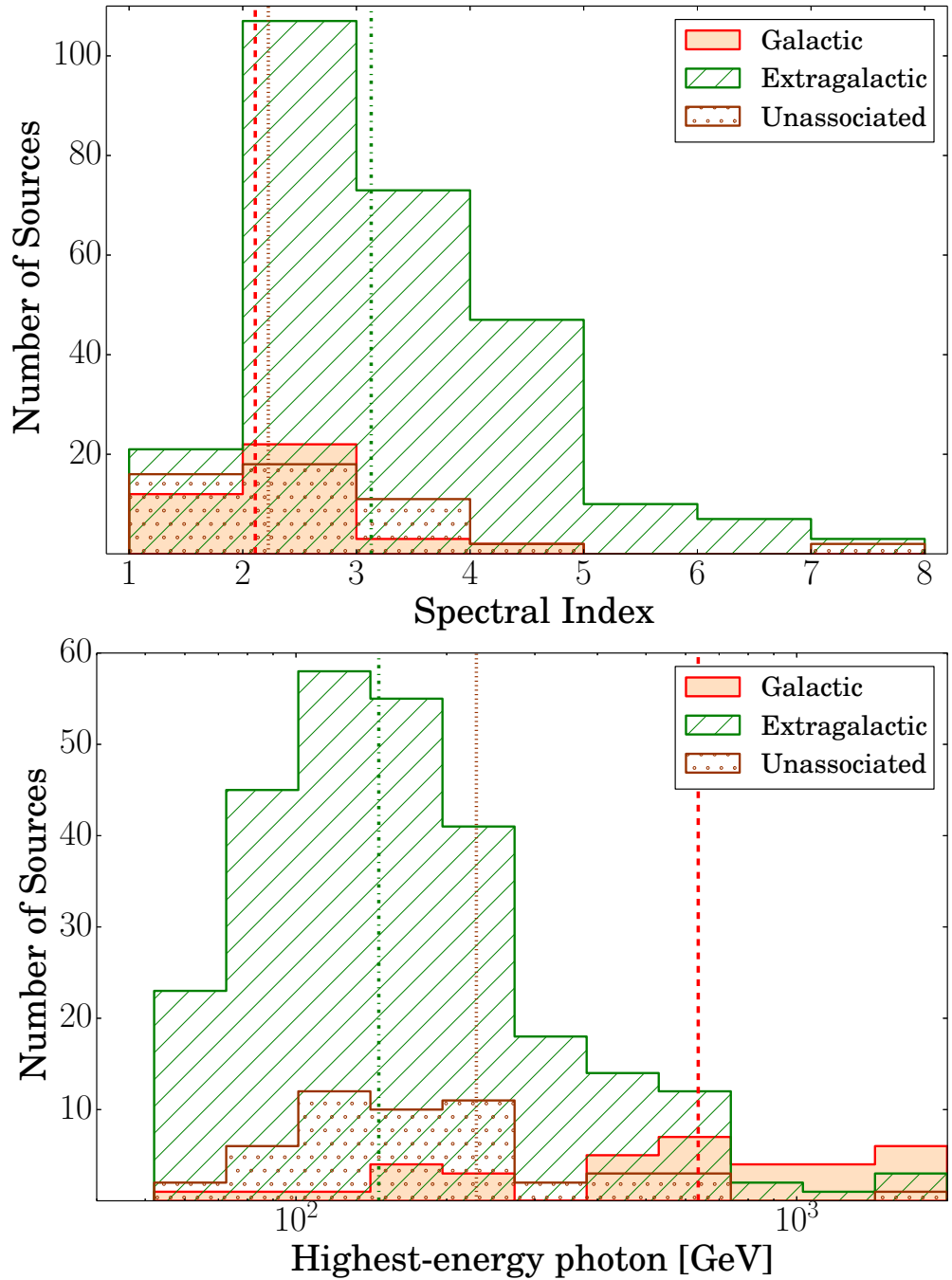


Figure 6.3: Distribution of the spectral indices (*top panel*) and highest photon energy (*bottom panel*) of the Galactic sources (orange), extragalactic sources (green slash), and unassociated sources (brown dotted). The medians of the distributions are plotted with dashed, dash-dotted, and dotted vertical lines, respectively. Both plots show that a distinct population of hard-spectrum sources is of Galactic origin.

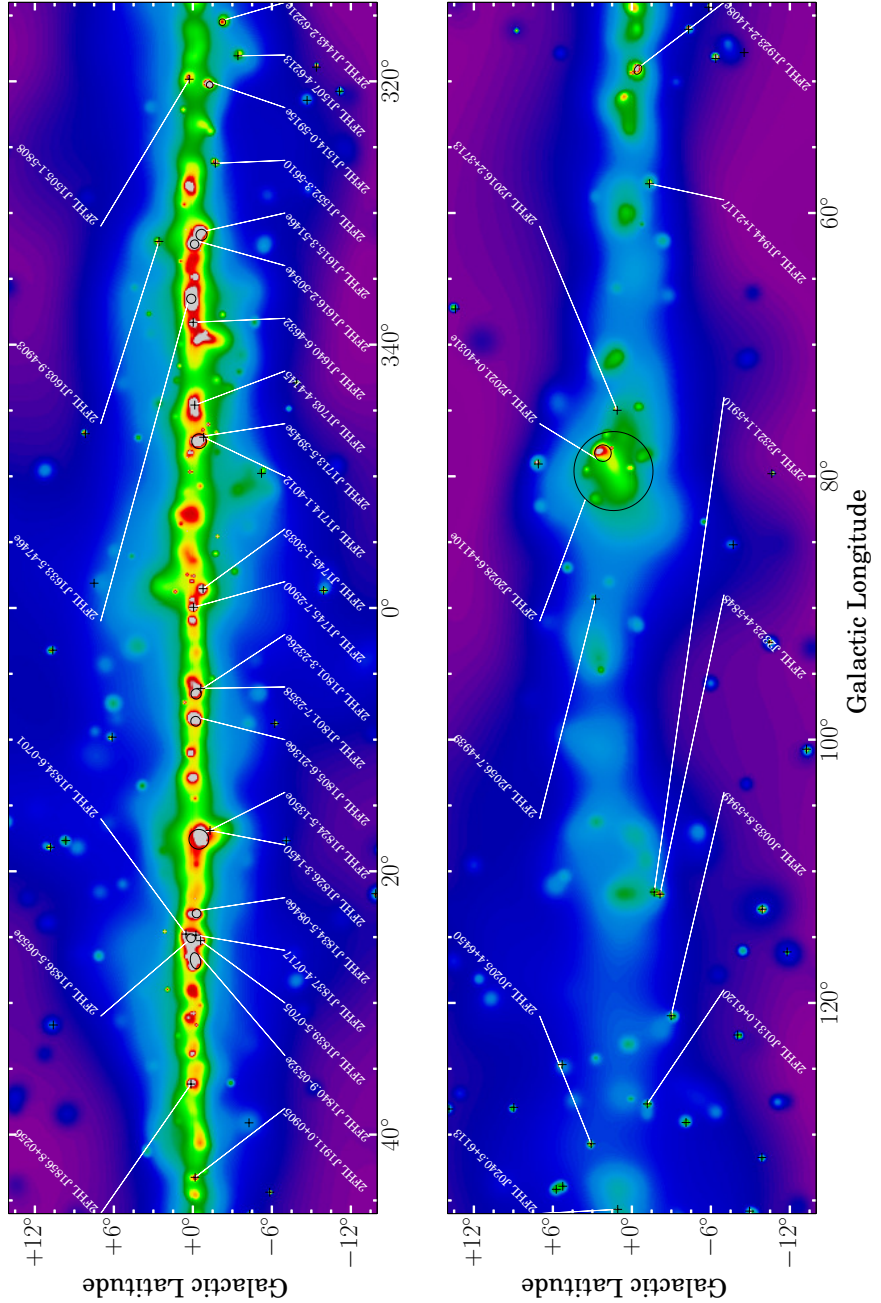


Figure 6.4: Adaptively smoothed count map showing the whole Galactic plane $0^\circ \leq l \leq 360^\circ$ at Galactic latitudes $-14^\circ \leq b \leq 14^\circ$ divided in four panels. The panels are centered at $l = 0^\circ$, 90° , 180° and 270° , respectively. Detected point sources are marked with a cross whereas extended sources are indicated with their extensions. Only sources located at $-4^\circ \leq b \leq 4^\circ$ are explicitly named, plus the Crab Nebula.

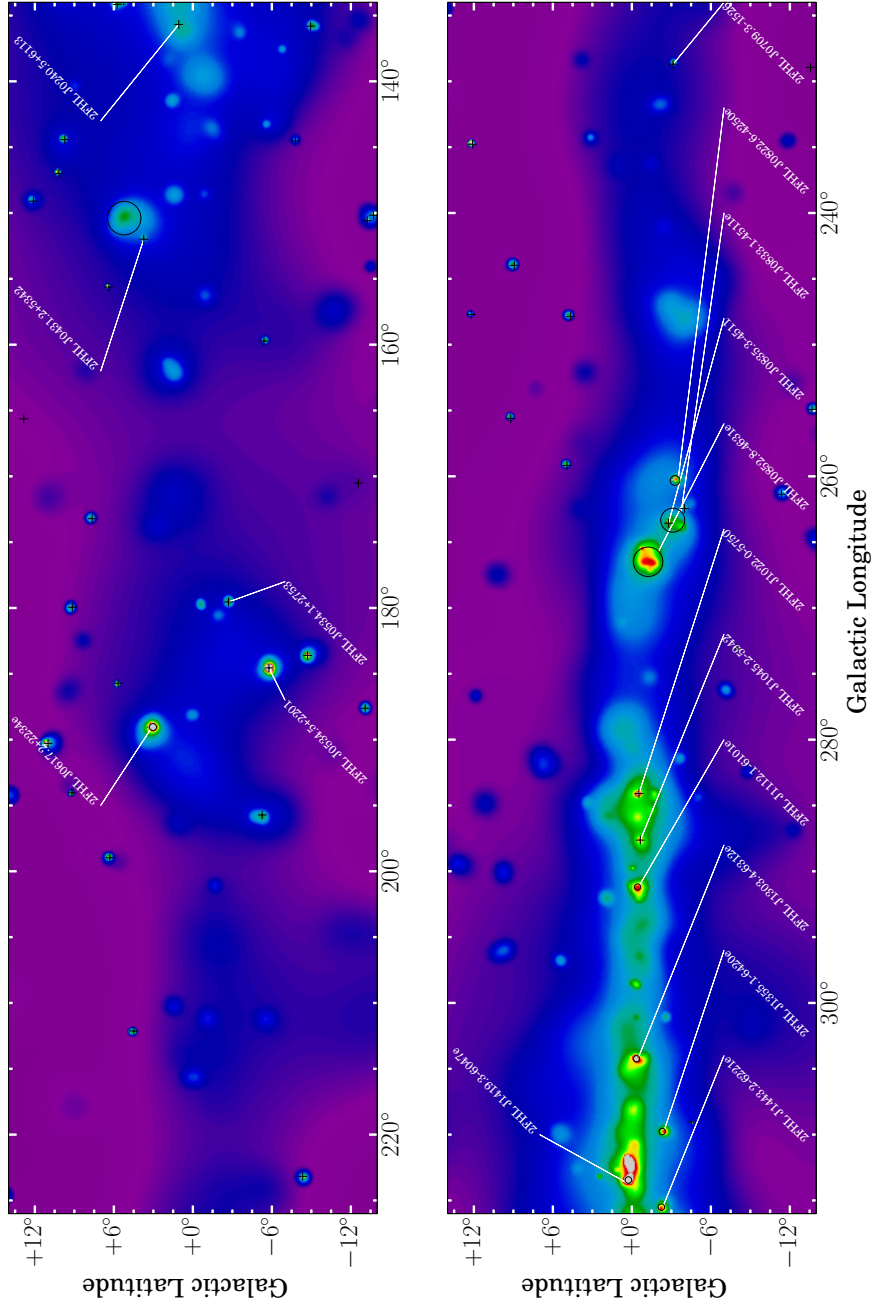


Fig. 6.4.— continued

the capability to detect new SNRs that might have been previously missed. Such an example is represented by the extended source 2FHL J0431.2+5553e which is spatially coincident with a new SNR (SNR G150.3+4.5) recently reported by Gao & Han (2014) (see Chapter 7).

Of the 14 sources at $|b| < 10^\circ$ that do not have an association, 7 have power-law indices harder than 2 which renders them likely Galactic objects. It is interesting to note that 6 of these 7 objects are offset from the plane of the Galaxy by more than 4° . This is in marked contrast with the associated portion of the sample where only the Crab Nebula and the newly discovered SNR G150.3+4.5 (out of 34 SNR/PWN systems) have such a large offset. Thus it seems unlikely that all these unassociated sources are SNR/PWN systems.

6.4.3 Comparison with the H.E.S.S. Galactic Plane Survey

The H.E.S.S array, with a field of view of about 5° and an angular resolution of approximately 0.12° , has invested 2800 hrs of exposure to survey part⁸ of the Galactic plane, reaching an average sensitivity of 2 % of the Crab Nebula flux (i.e. $4.5 \times 10^{-13} \text{ ph cm}^{-2} \text{ s}^{-1}$) at $\geq 1 \text{ TeV}$ (Aharonian et al. 2006b; Carrigan et al. 2013). Considering that the Crab Nebula spectrum is harder in the 2FHL band than in the $> 1 \text{ TeV}$ band, we estimate that the average sensitivity of 2FHL in the same region of the H.E.S.S. survey is $\sim 3\text{--}4\%$ of the $50 \text{ GeV}\text{--}2 \text{ TeV}$ Crab Nebula flux. The slightly better sensitivity allows H.E.S.S. to detect 69 sources (as reported in the TeVCat), while the LAT finds 36 objects in the same area. However, the comparable sensitivities of the two surveys allow the study of the properties of the high-energy Galactic population. In the 2FHL catalog there is almost an equal number of SNRs and PWNe in contrast to what is found in the H.E.S.S. survey where the ratio of PWNe to SNRs is 1.5 to 1. This might be because the hardest PWNe and softest SNRs are difficult to detect respectively in the $> 50 \text{ GeV}$ and $> 1 \text{ TeV}$ bands.

Of the 36 2FHL sources that fall within the footprint of the H.E.S.S. survey, 23

⁸The H.E.S.S. Galactic plane survey extends between $283^\circ < l < 59^\circ$ and Galactic latitudes of $|b| < 3.5^\circ$.

have already been detected at TeV energies and are associated with known counterparts, while 7 are undetected. The remaining 6 objects (2FHL J1022.0–5750, 2FHL J1505.1–5808, 2FHL J1507.4–6213, 2FHL J1703.4–4145, 2FHL J1745.1–3035 and 2FHL J1856.8+0256) are spatially coincident with TeV sources whose origin is not known. All of them have hard spectral indices ($\Gamma < 2.2$), but it is interesting to note that 4 of them (2FHL J1022.0–5750, 2FHL J1505.1–5808, 2FHL J1703.4–4145, and 2FHL J1745.1–3035) have $\Gamma < 1.7$ (see also Figure 6.5).

We find that 2FHL J1022.0–5750 is spatially compatible with HESS J1023–575, an extended TeV source (Abramowski et al. 2011b), whose emission might be due to a PWN powered by PSR J1023–5746 (Acero et al. 2013). 2FHL J1505.1–5808 is spatially coincident with the unidentified object HESS J1503–582, which has a size of 0.26° and a flux above 1 TeV (Renaud et al. 2008) compatible with the extrapolation of the 2FHL J1505.1–5808 spectrum. Its spectrum, reminiscent of that of a PWN (e.g., HESS J1825–137, Grondin et al. 2011), is reported in Figure 6.5.

2FHL J1507.4–6213 is spatially coincident with HESS J1507–622, an extended source with a radius of 0.15° located 3.5° from the plane (Acero et al. 2011). The analysis of multiwavelength data showed that it is not possible to discriminate between a hadronic and leptonic origin of the emission, but that the latter scenario, if the emission is powered by a PWN, would require a pulsar generated in the explosion of a hyper-velocity star in order to reach the required distance from the plane (Domainko & Ohm 2012).

The sources 2FHL J1703.4–4145 and 2FHL J1745.1–3035 are the hardest sources ($\Gamma < 1.3$) among the six objects. 2FHL J1703.4–4145 is spatially coincident with the bright radio emission observed from the western side of the shell of SNR G344.7–001, a nearby mid-aged shell-type (age ~ 3000 yr and $8'$ diameter) SNR (Giacani et al. 2011). Both the 2FHL source and the SNR are spatially coincident with the larger,

elongated and unidentified HESS J1702–420 (Aharonian et al. 2008c). It thus seems likely that SNR G344.7–001 is the counterpart of 2FHL J1703.4–4145 and perhaps also of HESS J1702–420. The combined *Fermi*-H.E.S.S. spectrum of this source is reported in Figure 6.5.

2FHL J1745.1–3035 is found to be spatially coincident with the extended source HESS J1745–303, which may be comprised of up to three different sources (Aharonian et al. 2008a). Indeed, the position of 2FHL J1745.1–3035 is compatible with the ‘C’ emission region (the second brightest region in the complex, Aharonian et al. 2008a). However, the nature of this source is more complex, because the 2FHL source is marginally brighter at 1 TeV than the entire H.E.S.S. region and also has a harder spectrum (spectral index of 1.25 ± 0.38 in 2FHL versus 2.17 ± 0.11 as measured by H.E.S.S.).

Finally, 2FHL J1856.8+0256 is coincident with HESS J1857+026, an almost radially symmetric extended source (Aharonian et al. 2008d), whose emission likely originates from a PWN powered by PSR J1856+0245 (Rousseau et al. 2012).

6.4.4 Extended Source Results

In total, 31 sources are modeled as spatially extended and input into the ML analysis: 25 listed in 3FGL, 5 sources detected in the `pointlike` analysis (described in Chapter 6.3.1) that were not detected as extended at the time of 3FGL, and one, SNR W41, reported recently by both the H.E.S.S. and LAT teams (Abramowski et al. 2015a). Names and properties of the extended sources are provided in Tables 6.1 and 6.2. Six extended sources, detected in 3FGL, were not detected in 2FHL: the SMC, S 147 (the point source 2FHL J0534.1+2753 was detected inside it), the lobes of Centaurus A (although we detect its core as a point source, 2FHL J1325.6–4301), W 44, HB 21 and the Cygnus Loop.

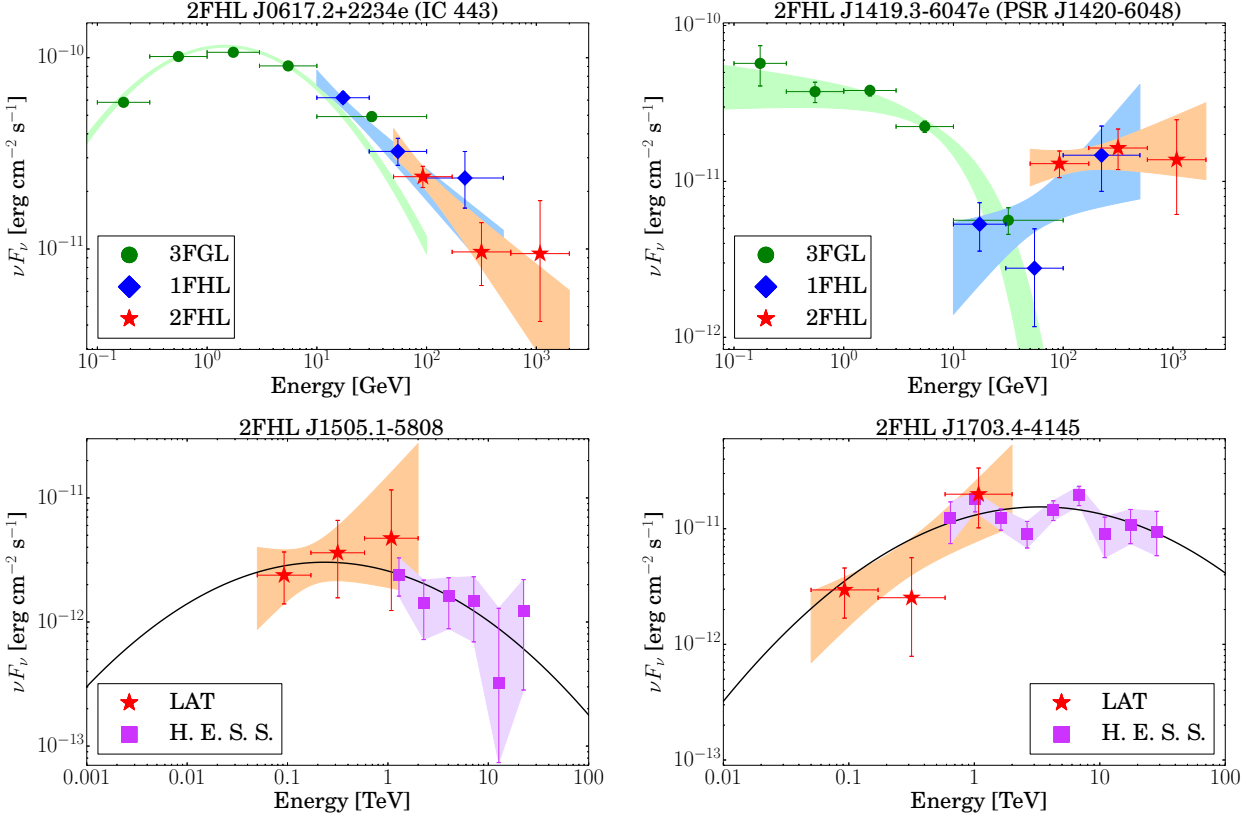


Figure 6.5: Spectral energy distributions of four Galactic sources constructed by combining data from the 3FGL (green diamonds), 1FHL (blue circles), and 2FHL (red stars). We show the 3FGL extended source SNR IC 443 (*top left*), the new 2FHL extended source PSR J1420–6048 (*top right*), and two “dark accelerators” detected by H.E.S.S. at TeV energies (Carrigan et al. 2013, purple squares) without a previous LAT counterpart: HESS J1503–582 (*bottom left*) and HESS J1702–420 (*bottom right*).

We detect a weak source, 2FHL J1714.1–4012 (TS = 27), just outside the south-western edge of the 3FGL spatial template used to model the emission from SNR RX J1713.7–3946 (2FHL J1713.5–3945e). 2FHL J1714.1–4012 has a hard spectral index $\Gamma = 1.63 \pm 0.38$, that is within errors of the spectral index derived for the SNR, $\Gamma = 2.03 \pm 0.20$ (Abdo et al. 2011). It is unclear whether 2FHL J1714.1–4012 is a distinct source separated from the SNR, or the result of un-modeled residual emission due to an imperfection in the spatial template adopted for the extended

source.

2FHL J1836.5–0655e is associated with the PWN HESS J1837–069. The 3FGL catalog contains several point sources in the vicinity of the PWN. We detect three sources in the vicinity, 2FHL J1834.5–0701, 2FHL J1837.4–0717 and 2FHL J1839.5–0705, the first two of which are coincident with 3FGL sources (3FGL J1834.6–0659, 3FGL J1837.6–0717 respectively). The power-law spectral indices of the three 2FHL point sources and 2FHL J1836.5–0655e are all consistent with each other. The concentration of sources around HESS J1837–069 combined with the spectral compatibility of the sources is suggestive of a common origin to the γ -ray emission in this region. However, the surrounding γ rays could arise from other sources in the region (Gotthelf & Halpern 2008); further analysis is necessary to determine the nature of the sources in this region.

A brief description of the five new 2FHL extended sources is given below with residual TS maps for the region surrounding each source shown in Figure 6.6. Detailed analyses of these new extended sources will be reported in separate papers.

2FHL J1443.2–6221e overlaps with the young, radio-detected SNR RCW 86 (G315.42.3). RCW 86 is a 42' diameter SNR that lies at a distance of 2.3–2.8 kpc and is likely associated with the first recorded supernova, SN 185 AD (Rosado et al. 1996b; Sollerman et al. 2003b). With more than 40 months of data and using the P7SOURCE dataset, the LAT did not significantly detect the SNR, but upper limits on detection at GeV energies combined with detection of significant extension in the TeV (Aharonian et al. 2009) were sufficient to strongly favor a leptonic origin for the emission (Lemoine-Goumard et al. 2012).

An updated LAT analysis of RCW 86 using 76 months of data, as well as the Pass 8 event-level analysis, resulted in detection of the SNR by the LAT as well as significant extension measurement (Ajello et al. 2016; Hewitt & Fermi-LAT Collab-

oration 2015, the former published after Ackermann et al. (2016)). In this paper, we report the results derived for 2FHL J1443.2–6221e from the `pointlike` analysis described in Chapter 6.3.1.

2FHL J1419.2–6048e is a newly detected extended sources with size $\sigma_{\text{disk}} = 0.36^\circ \pm 0.03^\circ$, that overlaps two nearby PWN/PSR complexes in the Kookaburra region. In the southwest of Kookaburra, HESS J1418–609 (Aharonian et al. 2006a) is coincident with both the extended non-thermal X-ray “Rabbit” PWN (G313.3+0.1, Roberts et al. 1999), and the γ -ray detected pulsar PSR J1418–6058 (Abdo et al. 2009). The northeast region, called “K3”, contains HESS J1420–607, coincident with PWN G313.5+0.3 and PSR J1420–6048. Acero et al. (2013) detected, with LAT, emission from both HESS J1418–609 (with a soft spectral index, pulsar-like spectrum) and HESS J1420–607 (with a hard power-law index) above 10 GeV, but only HESS J1420–607 was significantly detected above 30 GeV. Neither showed significant extension. Our result for the fitted power-law spectral index of 2FHL J1419.2–6048e is in agreement with the previous GeV and TeV results, yet our measured radius is considerably larger than the TeV extension. To compare the extensions of the uniform disk model used for 2FHL J1419.2–6048e in this paper to the Gaussian model of Aharonian et al. (2006a), we defined the radius which contains 68% of the source’s intensity as r_{68} , with $r_{68,\text{Gaussian}} = 1.51\sigma$, and $r_{68,\text{disk}} = 0.82\sigma$ (Lande et al. 2012). We find that $r_{68} \simeq 0.30^\circ$ for 2FHL J1419.2–6048e, and $r_{68} \simeq 0.09^\circ$ for HESS J1420–607.

2FHL J1355.2–6430e, coincident with the VHE source HESS J1356–645, is detected as extended ($\sigma_{\text{disk}} = 0.57^\circ \pm 0.02^\circ$) for the first time by the LAT in this work. The source HESS J1356–645 (Abramowski et al. 2011a) is associated with the pulsar PSR J1357–6429, which was determined to be powering a surrounding extended radio and X-ray PWN (Lemoine-Goumard et al. 2011). Acero et al.

(2013) detected faint emission from the nebula, and derived a 99% confidence limit, Bayesian upper limit on extension ($\sigma_{\text{Gauss}} < 0.39^\circ$) in the absence of significant extension. The fitted spectral index for 2FHL J1355.2–6430e is compatible with the GeV and TeV results (Abramowski et al. 2011a; Acero et al. 2013), however, the fitted disk extension is larger than that of the TeV detection, with $r_{68} \simeq 0.47^\circ$ for 2FHL J1355.2–6430e and $r_{68} \simeq 0.30^\circ$ for HESS J1356–645.

2FHL J1112.4–6059e is an extended source ($\sigma_{\text{disk}} = 0.53^\circ \pm 0.03^\circ$) newly detected by the LAT that encircles two 3FGL sources, 3FGL J1111.9–6058 and 3FGL J1111.9–6038, and has another, 3FGL J1112.0–6135, just outside its boundary (Acero et al. 2015b). The extended source also partially overlaps the massive star forming region NGC 3603.

Finally, **2FHL J0431.2+5553e** is a large extended source ($\sigma_{\text{disk}} = 1.27^\circ \pm 0.04^\circ$), with a hard spectrum, that has not been previously detected at γ -ray energies. It overlaps the recently discovered radio SNR G150.3+4.5 (Gao & Han 2014). G150.3+4.5 is a $2.5^\circ \times 3^\circ$ (Galactic coordinates) elliptical shell type SNR that has a steep radio synchrotron spectrum ($\alpha = -0.6$), indicative of radio SNRs. An in depth LAT analysis of this source extending the energy down to $E > 1$ GeV is presented in Chapter 7

6.5 Summary

We have presented an all-sky analysis at ≥ 50 GeV of 80 months of LAT data relying on the new Pass 8 event-level analysis. Pass 8 delivers improvements in the acceptance and the PSF, reduces background of misclassified charged particles and extends the energy range at which the LAT is sensitive. All this allowed the LAT to detect 360 sources in the 50 GeV–2 TeV range, performing an unbiased census of

Table 6.1. 2FHL extended sources previously detected by the *Fermi*-LAT

2FHL Name	<i>l</i> [deg]	<i>b</i> [deg]	TS	Association	Class	Spatial model	Radius [deg]
J0526.6–6825e	278.843	-32.850	49.80	LMC	gal	2D Gaussian	1.87
J0617.2+2234e	189.048	3.033	398.64	IC 443	snr	2D Gaussian	0.27
J0822.6–4250e	260.317	-3.277	63.87	Puppis A	snr	Disk	0.37
J0833.1–4511e	263.333	-3.104	49.70	Vela X	pwn	Disk	0.91
J0852.8–4631e	266.491	-1.233	437.21	Vela Jr	snr	Disk	1.12
J1303.4–6312e	304.235	-0.358	56.06	HESS J1303–631	pwn	2D Gaussian	0.24
J1514.0–5915e	320.269	-1.276	165.51	MSH 15–52	pwn	Disk	0.25
J1615.3–5146e	331.659	-0.659	128.15	HESS J1614–518	spp	Disk	0.42
J1616.2–5054e	332.365	-0.131	87.18	HESS J1616–508	pwn	Disk	0.32
J1633.5–4746e	336.517	0.121	114.17	HESS J1632–478	pwn	Disk	0.35
J1713.5–3945e	347.336	-0.473	60.98	RX J1713.7–3946	snr	Map	0.56
J1801.3–2326e	6.527	-0.251	50.20	W 28	snr	Disk	0.39
J1805.6–2136e	8.606	-0.211	160.43	W 30	snr	Disk	0.37
J1824.5–1350e	17.569	-0.452	266.09	HESS J1825–137	pwn	2D Gaussian	0.75
J1834.9–0848e	23.216	-0.373	67.30	W 41	spp	2D Gaussian	0.23
J1836.5–0655e	25.081	0.136	62.72	HESS J1837–069	pwn	Disk	0.33
J1840.9–0532e	26.796	-0.198	163.15	HESS J1841–055	pwn	Elliptical 2D Gaussian	0.62, 0.38, 39
J1923.2+1408e	49.112	-0.466	44.60	W 51C	snr	Elliptical Disk	0.38, 0.26, 90
J2021.0+4031e	78.241	2.197	115.97	Gamma Cygni	snr	Disk	0.63
J2028.6+4110e	79.601	1.396	28.09	Cygnus Cocoon	sfr	2D Gaussian	3.0

Note. — List of the 20 extended sources in 2FHL that were previously detected as extended by the *Fermi*-LAT. All these sources are in 3FGL except W41, which is studied by Abramowski et al. (2015b). The Galactic coordinates *l* and *b* are given in degrees. The extension of the disk templates is given by the radius. The extension of the 2D Gaussian templates is given by the 1σ radius, and the elliptical templates are given by the semi-major axis, semi-minor axis, and position angle (East of North). Association, Class, and Spatial model are as given in the Third *Fermi*-LAT source catalog (3FGL).

Table 6.2. New 2FHL extended sources

2FHL Name	<i>l</i> [deg]	<i>b</i> [deg]	TS	TS _{ext}	TS _{2pts}	<i>F</i> ₅₀	Δ <i>F</i> ₅₀	Γ	ΔΓ	Association	Class	Radius [deg]
J0431.2+5553e	150.384	5.216	87.9	83.4	26.2	11.70	2.11	1.66	0.20	G 150.3+4.5	snr	1.27 ± 0.04
J1112.4–6059e	291.222	-0.388	80.9	68.3	22.5	12.80	2.36	2.15	0.28	PSR J1112–6103	pwn	0.53 ± 0.03
J1355.2–6430e	309.730	-2.484	82.3	31.8	12.9	9.59	1.95	1.56	0.22	PSR J1357–6429	pwn	0.57 ± 0.02
J1419.2–6048e	313.432	0.260	109.3	49.1	15.6	17.60	2.80	1.87	0.19	PSR J1420–6048	pwn	0.36 ± 0.03
J1443.2–6221e	315.505	-2.239	75.6	29.9	19.2	7.23	1.70	2.07	0.30	SNR G315.4–2.3	snr	0.27 ± 0.03

Note. — List of the 5 new extended sources in 2FHL. All sources are characterized by a uniform disk template whose radius and uncertainty therein is given in the last column. *l* and *b* are Galactic coordinates. All coordinates are shown in degrees. TS is the test statistic. TS_{ext} is the significance of extension (6.3.2). TS_{2pts} is the TS of two simultaneously fit point sources (6.3.2). *F*₅₀ and Δ*F*₅₀ are the integrated photon flux between 50 GeV and 2 TeV and its uncertainty in units of 10^{-11} photon cm⁻² s⁻¹. Γ and ΔΓ are the photon index and its uncertainty from a power-law fit. Association lists the primary overlapping source and Class the suspected source type. All uncertainties are 1σ uncertainties.

the >50 GeV sky for the first time. This catalog of sources (dubbed 2FHL) provides a bridge between the traditional 0.1–100 GeV band of LAT catalogs (Acero et al. 2015b) and the $\gtrsim 100$ GeV band probed by IACTs from the ground. The 2FHL catalog has the potential to improve the efficiency with which new sources are detected at TeV energies since only about 25 % of the 2FHL sources were previously detected by IACTs.

2FHL includes 103 sources in the direction of the Galactic plane ($|b| < 10^\circ$). While a fraction of the sources ($\sim 39\%$) are associated with blazars, the rest are Galactic and unassociated sources. Galactic sources generally display much harder photon indices than blazars (median of ~ 2 versus ~ 3) and copious TeV emission, both signs of efficient particle acceleration. Most Galactic sources are associated with PWNe and SNRs, systems at the end of the stellar evolution cycle, and are detected as spatially extended. All the hard (spectral index < 2) unassociated sources within the plane of our Galaxy are likely of Galactic origin, since very few blazars have spectra as hard.

The Pass 8 event-level analysis and accumulated exposure allow the LAT to extend its reach to higher energy and to open a new window on the sub-TeV sky. Sensitivity improves linearly with time in the photon-limited regime, thus further observations by the LAT in the coming years will probe the > 50 GeV sky even more deeply, providing important targets for current and future Cherenkov telescopes.

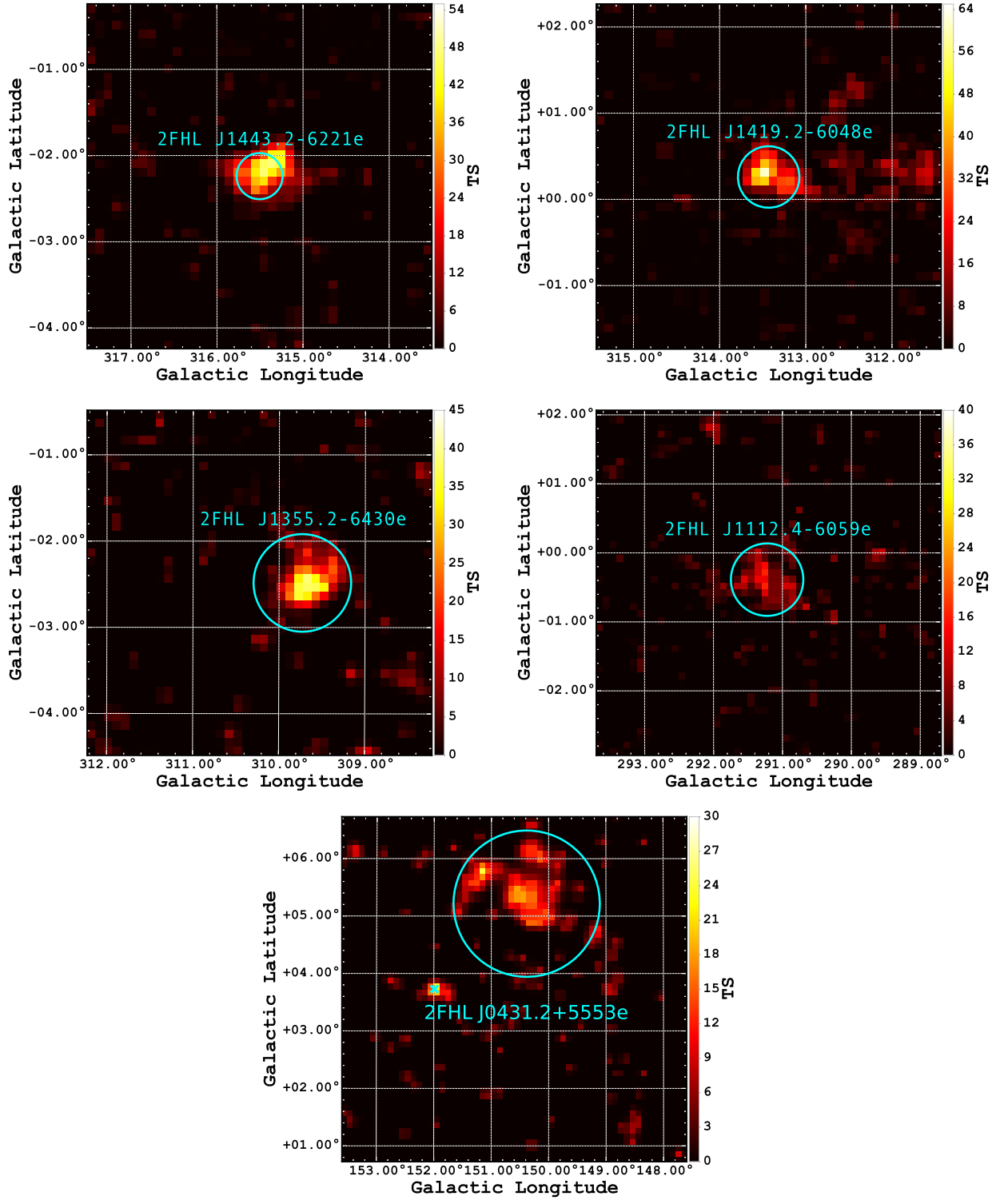


Figure 6.6: Residual TS maps for the five new extended sources described in Chapter 6.4.4. Only the Galactic diffuse and isotropic emission are included in the model to highlight the location of emission not associated with the diffuse background. Circles indicate the extents of the fit disks. The x marker in the bottom panel (2FHL J0431.2+5553e) shows the location of a point source in the ROI.

Chapter 7

Fermi-LAT Observations of Extended Gamma-Ray Emission in the Direction of SNR **G150.3+4.5.**

7.1 Introduction

SNRs have long been thought to be the most-likely accelerators of CRs up to the knee of the CR energy spectrum, with diffusive shock acceleration being the primary mechanism accelerating the charged particles to γ -ray emitting energies (see Reynolds (2008) for a review of SNRs from X-rays to γ -rays). *Fermi*-LAT was instrumental in demonstrating that CR protons can indeed be accelerated by SNR shock fronts (through detection of the characteristic "pion bump" feature), and are capable of generating the observed γ -ray emission in SNRs (Ackermann et al. 2013a; Jogler & Funk 2016). In addition, observations of SNRs with the LAT have proven

to be vital in uncovering a large swath of the γ -ray SNR population; both evolved SNRs interacting with dense surrounding material, as well as dynamically young remnants useful for probing acceleration directly at the shock (Acero et al. 2016).

The recently updated Pass 8 LAT event reconstruction provides a significantly improved angular resolution, acceptance, and background event rejection (Atwood et al. 2013a,b, and Chapter 3.4), all of which lead to an increase in the effective energy range and sensitivity of the LAT. Leveraging the increased sensitivity afforded by Pass 8 data, Ackermann et al. (2016) performed an all-sky analysis from 50 GeV to 2 TeV (referred to as the second catalog of hard *Fermi*-LAT sources, or 2FHL. See Chapter 6), directly connecting GeV LAT observations with those of ground-based Cherenkov telescopes at higher energies. While it is troublesome for Cherenkov telescopes operating under pointed observations to detect broadly extended sources on the sky (i.e. sources larger than the telescopes FoV), the LAT, with its all-sky survey mode and wide FOV, is well suited for this task. The 2FHL catalog detected significant spatial extension from 31 sources above 50 GeV, 5 of which had not previously been detected as extended.

Of particular interest, one of the 5 blindly detected sources, 2FHL J0431.2+5553e, was a large extended source (modeled as a uniform disk with radius, $\sigma = 1.27^\circ \pm 0.04^\circ$), exhibiting a hard power-law spectral index ($\Gamma = 1.66 \pm 0.20$). This 2FHL source was found to be coincident with a recently detected radio SNR, G150.3+4.5. Faint emission from the eastern portion of the shell of G150.3+4.5 was first reported in Gerbrandt et al. (2014) (called G150.8+3.8), and considered a strong SNR candidate due to the semi-circular shape of the emission, clearly non-thermal spectrum, and the presence of red optical filamentary structures. Gao & Han (2014) performed follow-up observations of the region using Urumqi 6 cm survey data (as well as Effelsberg 11cm and 21cm data and CGPS 1420 MHz and 408 MHz observations), taking

advantage of the survey's extended Galactic latitude range, up to $b=20^\circ$. They reported clear detection of a 2.5° wide by 3° high, synchrotron emitting, shell-like object (G150.3+4.5), bolstering an SNR origin for the radio emission.

2FHL J0431.2+5553e only partially overlaps the northern region of G150.3+4.5, so the nature of the extended source is uncertain. In this chapter, we present an in depth study of the γ -ray emission in the direction of SNR G150.3+4.5, extending the energy from 50 GeV in 2FHL, down to 1 GeV. We report here detection of a significantly extended source whose extent matches well with that of G150.3+4.5. We describe the LAT observations and explore the spectral and spatial properties of the extended γ -ray source in Chapter 7.2. In Chapter 7.3 we employ archival HI and X-ray observations to assess the properties of the environment G150.3+4.5 resides in. Finally, in Chapter 7.4 we discuss potential γ -ray emission scenarios and model the broadband emission from the source to constrain the origin of the GeV emission and understand the connection between the radio detected source G150.3+4.5 and the γ -ray one.

7.2 *Fermi*-LAT Observations and Analysis

7.2.1 Data Set and Reduction

Fermi-LAT is a pair conversion telescope sensitive to high energy γ -rays from 20 MeV to greater than 1 TeV (Ackermann et al. 2016), operating primarily in a sky-survey mode which views the entire sky every 3 hours. The LAT has a wide field of view (~ 2.4 sr), a large effective area of ~ 8200 cm 2 at 1 GeV for on axis events and a 68% containment radius angular resolution of $\sim 0.8^\circ$ at 1 GeV. For further details on the instrument and its performance see Atwood et al. (2009), Ackermann et al. (2012c), and Chapter 3.

In this study, we analyzed 7 years of Pass 8 data, from August 2nd 2008 to August 2nd 2015. Source class events were analyzed within a $14^\circ \times 14^\circ$ region centered on G150.3+4.5 using the P8R2_SOURCE_V6 instrument response functions, with a pixel size of 0.1° . To reduce contamination from earth limb γ -rays, only events with zenith angle less than 100° were included.

For spectral and spatial analysis we utilized both the standard *Fermi* Science Tools (version 10-01-01)¹, and the binned maximum likelihood package **pointlike** (Kerr 2010). **pointlike** provides methods for simultaneously fitting the spectrum, position, and spatial extension of a source, and was extensively validated in Lande et al. (2012). Both packages fit a source model, the Galactic diffuse emission, and an isotropic component (which accounts for the background of misclassified charged particles and the extragalactic diffuse γ -ray background, see Chapter ??) to the observations. In this analysis, we used the standard Galactic diffuse ring-hybrid model scaled for Pass 8 analysis, gll_iem_v06.fits (modulated by a power law function with free index and normalization), and for the isotropic emission, we used iso_P8R2_SOURCE_V6_v06.txt, extrapolated to 2 TeV as in Ackermann et al. (2016).

In our source model for the region, we included sources from the third *Fermi*-LAT catalog (Acero et al. 2015b, 3FGL) within 15° of the center of our region of interest (RoI). We replaced the position and spectrum of any 3FGL pulsars in the region with their corresponding counterpart from the LAT 2nd pulsar catalog (Abdo et al. 2013). Residual emission unaccounted for by 3FGL sources is present in the RoI due to the increased time range and different energy selection with respect to that in 3FGL. We added to the RoI several significant ($TS \geq 16$) point sources to account for this unmodeled emission and minimize the global residuals. The closest

¹<http://fermi.gsfc.nasa.gov/ssc/>

of these sources added was over 1° away from the edge of the best fit GeV disk. Considering the size of the PSF at 1 GeV, the affect of these sources on the disk fit was assumed to be negligible and we do not discuss them further. The normalization and spectral index of sources within 5° of the center of the RoI were free to vary, whereas all other source parameters were fixed. A preliminary maximum likelihood fit of the RoI was performed, and sources with a test statistic ($TS < 9$ (TS is defined as, $TS = 2 \log(\mathcal{L}_1/\mathcal{L}_0)$ where \mathcal{L}_1 is the likelihood of source plus background and \mathcal{L}_0 that of just the background) were removed from the model.

7.2.2 Morphological Analysis

Studying the spatial extension of sources with the LAT is non-trivial due to the energy-dependent PSF and strong diffuse emission present in the Galactic plane. Soft spectrum point sources and uncertainties in the diffuse model can act as sources of systematic error when not accurately modeling extended emission as such, particularly at low energies where the PSF is broad. To strike a balance between the best angular resolution and minimal source and diffuse contamination, we restrict our morphological analysis to energies between 1 GeV and 1 TeV. We divide this energy range into 12 logarithmically spaced bins for both `pointlike` and `gtlike` binned likelihood analyses.

Three unidentified 3FGL sources are located within the extent of G150.3+4.5. 3FGL J0425.8+5600, located approximately 0.6° from the center of the SNR, is the closest of the three sources and is described with a power law spectrum of index $\Gamma = 2.35 \pm 0.17$ in the 3FGL catalog. The closest radio source to 3FGL J0425.8+5600 is NVSS J042719+560823, at 0.25 away (Condon et al. 1998). 3FGL J0423.5+5442, exhibits a power law spectral index, $\Gamma = 2.63 \pm 0.15$, with no clear multiwavelength source association. Finally, 3FGL J0426.7+5437 has a pulsar-like

spectrum, yet in a timing survey performed with the 100-m Effelsberg radio telescope, Barr et al. (2013) were unable to detect pulsations from the source down to a limiting flux density of ~ 0.1 mJy. This source is located about 0.84° from the center of the SNR. We discuss 3FGL J0426.7+5437 and potential association with G150.3+4.5 further in Chapter 7.4.2. Figure 7.1 is a counts map of the region, showing the location of the 3FGL sources.

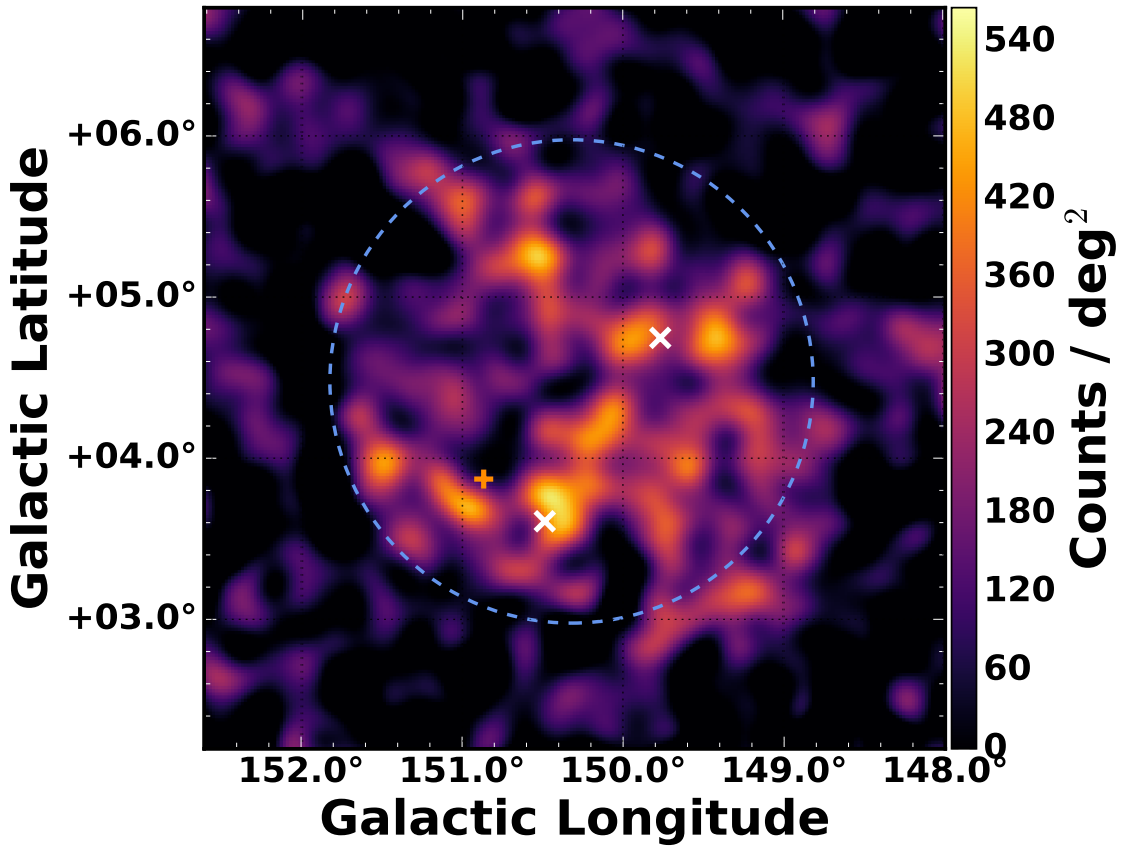


Figure 7.1: Smoothed background subtracted residual counts map above 1 GeV where $0.1^\circ \times 0.1^\circ$ pixels were smoothed with a Gaussian kernel of 0.1° , centered on SNR G150.3+4.5. 3FGL J0426.7+5437 and the diffuse backgrounds are included in the region model, 3FGL J0425.8+5600 and 3FGL J0423.5+5442 are not (but their locations are shown as white crosses).

In our analysis, we removed 3FGL J0425.8+5600 and 3FGL J0423.5+5442 from the ROI, but kept 3FGL J0426.7+5437 in the model since preliminary analyses showed clear positive residual emission at the position of the source if it was re-

moved from the RoI. Figure 7.2 shows a residual TS map for the region around G150.3+4.5. This point source detection-significance map was created by placing a point source modeled with a power law of photon index $\Gamma = 2$ at each pixel and gives the significance of detecting a point source at each location above the background.

We modeled the excess emission in the direction of G150.3+4.5 with a uniform intensity, radially-symmetric disk, simultaneously fitting the spatial and spectral components of the model via `pointlike`. The extension of the disk was initialized with a seed radius of $\sigma = 0.1^\circ$ and position centered on the radio position of G150.3+4.5. We define the significance of extension as in Lande et al. (2012); $TS_{\text{ext}} = 2 \log(\mathcal{L}_{\text{ext}}/\mathcal{L}_{\text{ps}})$, with \mathcal{L}_{ext} being the likelihood of the model with the extended source and \mathcal{L}_{ps} that of a point source located at the peak of emission interior to the extended source. For the disk model we found that $TS_{\text{ext}} = 298$, for the best fit radius, $\sigma = 1.40^\circ \pm 0.03^\circ$, and position, R.A. = $55.46^\circ \pm 0.03^\circ$, DEC. = $66.91^\circ \pm 0.03^\circ$, all in excellent agreement with the radio SNR size and centroid determined in Gao & Han (2014). Figure 7.3 shows radially integrated counts for the region as a function of angular radius squared. It is clear from this figure that there is significant excess of counts above the Galactic diffuse radiation in this region that is adequately modeled by a symmetric disk. We tried adding back in to our model the two removed 3FGL sources but both were insignificant when fit on top of the best fit disk. The bottom map in Figure 7.2 is a residual TS map of the same region as the top map, but with the disk source included in the background model, demonstrating that the disk can account well for the emission in the region and justifying the exclusion of the two aforementioned 3FGL sources.

The morphology of the radio emission is suggestive of an elliptical or ring morphology, so both of these spatial models were tested as well. For the ring model, the fit reduced to a disk with parameters matching those stated above. Using the

elliptical model showed a weak improvement over the radially symmetric model at the 2.6σ level ($\Delta\text{TS} = 9$ with two additional degrees of freedom), which we did not consider significant enough to say the GeV emission had an elliptical morphology. For the remainder of this study, we only considered the disk spatial model.

2FHL J0431.2+5553e is the extended source detected in the 2FHL catalog found to be overlapping the northern region of G150.3+4.5 Ackermann et al. (2016). The source has a power law spectral index $\Gamma = 1.66 \pm 0.2$, and disk radius $\sigma = 1.27^\circ \pm 0.04^\circ$ (see Figure 7.2). When comparing the best fit extension of the 2FHL source with the result from this paper, factoring in the uncertainty in both extension and position, we see that the > 50 GeV and > 1 GeV results are not incompatible. It is likely that the paucity of events above 50 GeV is the cause of the smaller fit radius, as opposed to the difference arising from the effects of an energy dependent morphology. To explore the connection between the 2FHL and above 1 GeV emission, we tested a few other spatial hypotheses.

First, we replaced the $\sigma = 1.40^\circ$ disk with another disk matching the spectral and spatial parameters of 2FHL J0431.2+5553e and calculated the likelihood with this new source's position and extension fixed. For this hypothesis, we find $\text{TS}_{\text{ext}} = 165$, and $\text{TS} = 226$, demonstrating that the fixed disk matching the 2FHL source is clearly disfavored over the previously determined best fit disk at this energy. Our next test consisted of placing a second extended source on top of the best fit disk detected above 1 GeV. We added a source, initially matching the spatial and spectral parameters of 2FHL J0431.2+5553e, to our source model of the region (in addition to the $\sigma = 1.40^\circ$ disk), and fit its spectrum and extension. Fitting a second extended source in this region serves two purposes: 1. it acts as a check on whether there was residual emission unaccounted for by the previously best-fit disk, and 2. it allows us to determine if the best fit disk can be split into two spectrally distinct,

components. This fit resulted in the source wandering north (but still partially overlapping G150.3+4.5) and having an insignificant extension, $\text{TS}_{\text{ext}} = 4$.

7.2.3 Spectral Analysis

After determining the best fit morphology with `pointlike` for the GeV emission coincident with G150.3+4.5, we used those results as a starting point for our `gtlike` maximum-likelihood fit of the region to estimate the best spectral parameters for our model. The LAT data is well described by a power law from 1 GeV to 1 TeV with a photon index, $\Gamma = 1.82 \pm 0.04$, and energy flux above 1 GeV of $(7.3 \pm 0.72) \times 10^{-11} \text{ erg cm}^{-2} \text{ s}^{-1}$ and $\text{TS} = 389$. We tested the γ -ray spectrum of the extended disk for spectral curvature using a log-normal model (Log Parabola), and find no significant deviation from a power law ($\Delta\text{TS} \sim 1$). Figure 7.4 shows the best-fit power law spectral energy distribution for the GeV source whose morphology was described in Section 7.2.2. Spectral data points were obtained by dividing the energy range into 12 logarithmically spaced bins and modeling the source with a power law of fixed spectra index, $\Gamma = 2$. We over plotted the SED of 3FGL J0426.7+5437 to demonstrate how the spectra of the two sources are comparable in the lowest energy bin and would grow more confused at energies below 1 GeV.

7.3 Multiwavelength Observations and Analysis

7.3.1 HI Observations and Distance Estimate

Using data from the Leiden/Argentine/Bonn survey of Galactic HI, we obtained the HI spectrum in the direction of G150.3+4.5. The spectrum shown in Figure 7.5 displays clear velocity peaks at $-44.7, -35.9, -6.9$ and $+2.9 \text{ km s}^{-1}$. The widths of all peaks are 5 km s^{-1} or less, thus there is no evidence of shock-broadening from

the SNR shock, where broadening is an indicator of the shock of an SNR overtaking nearby molecular clouds Wootten (1981, 1977).

Knowing the distance to G150.3+4.5 is integral in determining the physical size of the SNR and in turn understanding the origin of the γ -ray emission. We calculate the kinematic distance to G150.3+4.5 as in Reid et al. (2014), assuming a flat Galactic rotation curve with Galactocentric distance, $R_0 = 8.34$ kpc, and circular rotation speed at the sun, $\Theta = 240$ km s $^{-1}$. For the three negative velocities noted above (the positive velocity is not permitted at this Galactic longitude), we determine distances of 5.6, 3.9, and 0.38 kpc respectively. For an angular radius of, $\sigma = 1.40^\circ$ (as determined in Chapter 7.2.2), these distances correspond to physical diameters of 135.8, 96.3, and 9.4 pc. The two further distances, and hence larger diameters are indicative of an SNR in the radiative phase of evolution. However, at this late stage of evolution, the shock front of an SNR will have expanded, loosing much of its initial energy, and is not expected to be capable of accelerating CRs to γ -ray energies. Thus, the only feasible distance, derived from the HI velocities, is the nearest distance, $d_{\text{near}} \approx 0.38$ kpc.

There are two HII regions known to lie at the edge of the SNR shell, so it is reasonable to think there may be a physical association between the clouds and the SNR. Lying at a distance (in projection) of 4 kpc (Gao & Han 2014), the physical radius of the SNR, if it was at the same distance, would be ≈ 98 pc. Aside from the proximity (in projection), there is no evidence to suggest that the clouds are physically associated with the SNR. In fact, the lack of ROSAT X-ray emission in the vicinity of the G150.3+4.5 (see the following section), suggests that the SNR is not associated with the cloud at all.. Another potential scenario is that the SNR lies in the Perseus spiral arm of the Galaxy at a distance of 2 kpc (Xu et al. 2006). At that distance, the physical extent of the SNR would be ≈ 49 pc. Again, an SNR

of this size is not expected to emit γ -rays.

A final note on possible distances for G150.3+4.5; Badenes et al. (2010) observed a cutoff in the size distribution of SNRs of ≈ 60 pc in the small and large Magellanic clouds as well as M33. This suggested that there may be a universal cutoff in size for SNRs. If the physical diameter of G150.3+4.5 was 60 pc, this would place the SNR at a distance $d_{\max} = 1.2$ kpc. While there is no physical reason to suggest that the SNR is at this distance, it is a reasonable distance/size combination for the SNR to still be emitting γ -rays. We consider this a maximum distance for the SNR.

7.3.2 X-ray Observations

We used archival observations from the ROSAT all-sky survey (Voges et al. 1999) to determine if there was significant X-ray emission (0.4 keV – 2.4 keV) in the direction of G150.3+4.5. The ROSAT data was extracted within a 1.3° radius centered on the SNR with a total exposure of 5.37 hr. To determine an upper limit on the X-ray emitting density, we modeled the emission (via XSPEC) as an absorbed thermal NEI plasma with $kT = 0.5$ keV. The derived maximum emitting density was found to be $n_H < 0.02(D/1 \text{ kpc})^{-1/2} \text{ cm}^{-3}$, with a maximum photon flux of $0.04 \text{ ph cm}^{-2} \text{ s}^{-1}$, and corresponding maximum energy flux of $4 \times 10^{-11} \text{ erg cm}^{-2} \text{ s}^{-1}$ between 0.5 and 2 keV . We also simulated the emission from the region with an absorbed non-thermal PL model to assess any potential synchrotron flux from the SNR. Using a PL with spectral index $\Gamma = 2$, we find a maximum flux of $0.03 \text{ ph cm}^{-2} \text{ s}^{-1}$, and corresponding maximum energy flux of $5 \times 10^{-11} \text{ erg cm}^{-2} \text{ s}^{-1}$.

Assuming the near distance calculated in Chapter 7.3.1, the maximum emitting density is $n_H < 0.02(D/1 \text{ kpc})^{-1/2} \text{ cm}^{-3} = 0.03 \text{ cm}^{-3}$. Under standard shock conditions, the shock compression ratio is 4, and the corresponding ambient density (that of the unshocked medium), rarefied by a factor of 4, is $n_0 = 0.008 \text{ cm}^{-3}$.

7.4 Discussion and Results

7.4.1 G150: Supernova Remnant or Pulsar Wind Nebula?

The follow-up observations of the γ -ray emission in the direction of G150.3+4.5, presented here, of the source detected above 50 GeV in 2FHL have led to the detection of an extended γ -ray source whose centroid and radius match extremely well with those of the radio detected SNR. The broad size of the extended source and correlation with the radio shell leave few plausible scenarios for the nature of the GeV emission. Namely, the GeV emission can arise from the wind nebula of the putative pulsar of G150.3+4.5 or the GeV emission corresponds to γ -rays produced in the SNR. We argue here that the SNR is favored over a pulsar wind nebulae (PWN) as the generator of the observed γ -rays.

The first problem with the PWN hypothesis is that there is no pulsar candidate detected near the centroid of the SNR to power a PWN. While 3FGL J0425.8+5600 is the closest γ -ray source to the center of the remnant, it does not have a pulsar-esque spectrum, it lies about 0.25° away, and we showed in Chapter 7.2.2 that with the best-fit disk hypothesis, neither 3FGL J0425.8+5600 nor 3FGL J0423.5+5442 are significant in the likelihood model of the region. 3FGL J0426.7+5437, with a spectrum reminiscent of a pulsar, may actually be one, but as discussed previously, Barr et al. (2013) detect no pulsations from the source). Furthermore, the source is 0.84° away from the centroid of G150.3+4.5. Typical pulsar ballistic velocities range from $V_{\text{PSR}} \sim 400 - 500 \text{ km s}^{-1}$, with extreme velocities exceeding 1000 km s^{-1} (Gaensler & Slane 2006). If 3FGL J0426.7+5437 was the compact remnant of the progenitor star that birthed G150.3+4.5, it would have to be traveling with a velocity, $V_{\text{PSR}} = 1125 \text{ km s}^{-1}$ (assuming an age of 5 kyr, which we derive in

the following section, Chapter 7.4.2), and would make it one of the fastest known pulsars (Chatterjee et al. 2005). While possible, this scenario is unlikely without further evidence to support such a high velocity.

Another argument disfavoring the PWN scenario is that, despite the hard γ -ray spectral index extending to TeV energies, ROSAT X-ray observations detect no significant emission suggestive of a PWN in the direction of G150.3+4.5 (see Typical PWNe spectral indices range from about $-0.3 \lesssim \alpha \lesssim 0$ (Gaensler & Slane 2006). The radio spectral index as determined in Gao & Han (2014) ($\alpha = 0.4 \pm 0.17$ for part of the eastern shell, $\alpha = 0.69 \pm 0.24$ for a region in western shell) suggests that the radio object is likely not a PWN.

Many of the arguments disfavoring the PWN hypothesis in fact bolster that of SNR. First and foremost in favor of an SNR origin for the γ -ray emission is the excellent agreement between the GeV best-fit disk radius and centroid with that of the radio shell. The radio shell-like appearance, non-thermal radio spectrum, and strands of red optical filamentary structures led both Gao & Han (2014) and Gerbrandt et al. (2014) to regard the radio source an SNR as opposed to a PWN. The radio spectral index, while not quite in line with typical PWN spectra, is actually common of SNRs.

While the above factors lend credence to an SNR origin for the GeV γ -rays the PWN scenario can not be ruled out due to the lack of an associated pulsar. Regardless, for the remainder of this study, we assumed the observed γ -rays were produced in the shock front of SNR G150.3+4.5

7.4.2 G150.3+4.5 in a Supernova Remnant Context

Having associated the γ -ray emission with G150.3+4.5, next, we assessed the evolutionary state of the remnant to place it in context within the current population of LAT SNRs. Using the most viable HI kinematic distance, $d \approx 0.38$ kpc derived in Chapter 7.3.1, we showed that the projected radius of G150.3+4.5 is $R \approx 9.4$ pc. Employing a standard Sedov-Taylor solution for the expansion of a blast wave, we estimated the age of G150.3+4.5. In the Sedov phase, the radius of the shock front is given by,

$$R_{ST} = 0.314 \left(\frac{E_{51}}{n_0} \right)^{1/5} t_{\text{yr}}^{2/5} \text{pc} \quad (7.1)$$

Where E_{51} is the kinetic energy output of the supernova in units of 10^{51} erg, and n_0 the ambient density the shock is expanding into in units of cm^{-3} . Assuming standard values of 1 for E_{51} and n_0 we solved equation 7.1 for t_{yr} (the current age of the remnant in years) and used the value of R derived for G150.3+4.5 to estimate the age of the SNR as $t \approx 4.9$ kyr.

Figure 7.6 shows the SED of G150.3+4.5 overlaid on the spectra of a selection of other LAT observed SNRs with ages ranging from $\sim 10^3 - 10^4$ yr. G150.3+4.5 exhibits a hard spectrum extending to TeV energies with no spectral break (breaks are commonly seen in LAT SNRs interacting with nearby molecular material (Hewitt & Lemoine-Goumard 2015)) and appears spectrally similar to the younger SNRs like RX J1713.7-3946 and RX J0852.0-4622. In figure 7.7, we plotted the luminosity of several LAT SNRs against their squared diameters (a proxy for age, as evident from equation 7.1). Similarly, with its low luminosity, G150.3+4.5 appears to correlate well with the younger sect of LAT SNRs. Our age estimate alone does not unambiguously determine the evolutionary state of G150.3+4.5. However, when

combined with the results of Figures 7.6 and 7.7 comparing G150.3+4.5 to the population of other LAT SNRs, it indicates that G150.3+4.5 is more compatible with a dynamically unevolved, non-interacting (with the surrounding interstellar medium) stage of expansion.

7.4.3 Nonthermal Modeling

SNR shock fronts are known accelerators of cosmic rays to very high energies. There are potentially multiple radiation mechanisms operating at the shock that produce GeV γ -rays. Accelerated electrons can give rise to inverse Compton (IC) emission via upscattering of ambient cosmic microwave background (CMB), stellar, and IR photon fields, as well as non-thermal bremsstrahlung radiation. Energetic protons can collide with ambient protons in the surrounding, producing neutral pions which decay into γ -ray photons.

To infer the properties of the underlying relativistic particle populations in the SNR environment, it is vital to understand the origin of the observed γ -ray emission detected from G150.3+4.5. To do so, we employ the `naima` Python package. `naima` is an open-source code base that computes the non-thermal radiation from a relativistic particle population (Zabalza 2015). It utilizes known parameterizations and analytic approximations to the various non-thermal processes (i.e., synchrotron, IC, bremsstrahlung, and pion decay emission), which results in the calculations being computationally inexpensive. `naima` also makes use of `emcee`, a Markov chain Monte Carlo (MCMC) ensemble sampler for Bayesian parameter estimation (Foreman-Mackey et al. 2013). The sampler is used to find the best-fit parameters of the radiative models to the observed photon SED for a given particle distribution function.

To determine the best fit parameters, `naima` calls `emcee` to sample the log-

likelihood function (i.e., the likelihood of the observed data given the assumed spectrum) of the radiative model. The radiative models require as input a particle distribution function to model the present-age electron or proton spectrum. We used a one-zone, homogeneous particle distribution model (which `naima` inherently assumes) and scaled the likelihood function by a uniform prior probability distribution. For this work, we model the separate proton and electron and spectra as power laws with an exponential cut off,

$$\frac{dN}{dE_{(e,p)}} = A_{(e,p)}(E/E_0)^{-s} \exp\left(\frac{-E}{E_{\text{cutoff (e,p)}}}\right) \quad (7.2)$$

where E is the particle energy, E_0 the reference energy, s the spectral index, and E_{cutoff} the cutoff energy. The electron distribution's normalization is related to the proton normalization through the electron-to-proton ratio scaling factor, $A_e = K_{ep}A_p$. We also assumed that the electron and proton distributions have the same spectral shape. For our radiation models, we assumed a gas density, $n_0 = 1 \text{ cm}^{-3}$ for proton-proton interactions. For IC emission, we include a CMB, FIR, and NIR component.

7.5 Conclusions

We analyzed 7 years of *Fermi*-LAT data in the direction of SNR G150.3+4.5, lowering the energy threshold from that previously reported in the 2FHL catalog, and report detection of significantly extended γ -ray emission coincident with the entirety of the radio remnant's shell. We find the emission from 1 GeV to 1 TeV to be well described by a power law of spectral index $\Gamma = 1.82 \pm 0.04$, with morphology consistent with a uniform disk with best-fit radius, $\sigma = 1.40^\circ \pm 0.03^\circ$. Based on radio and γ -ray properties of emission in the direction of G150.3+4.5, within the con-

text of the current LAT SNR population, we argued that the GeV emission likely originates in the shock of G150.3+4.5, and disfavor a PWN origin. To estimate the distance to the SNR, we obtained an HI spectrum toward G150.3+4.5 from the Leiden/Argentine/Bonn survey of Galactic HI. Calculating distances from the derived HI velocity peaks, we showed that the most reasonable distance estimate places G150.3+4.5 at a distance of $d = 0.4$ kpc, making it one of the closest known SNRs detected by the LAT. Using this distance and a standard Sedov-Taylor SNR evolution model, we estimate the age of the G150.3+4.5 to be $t \sim 5$ kyr. To assess the underlying particle population acting in G150.3+4.5 we use the `naima` Python package to fit the observed radio and γ -ray SED to non-thermal electron and proton radiation models.

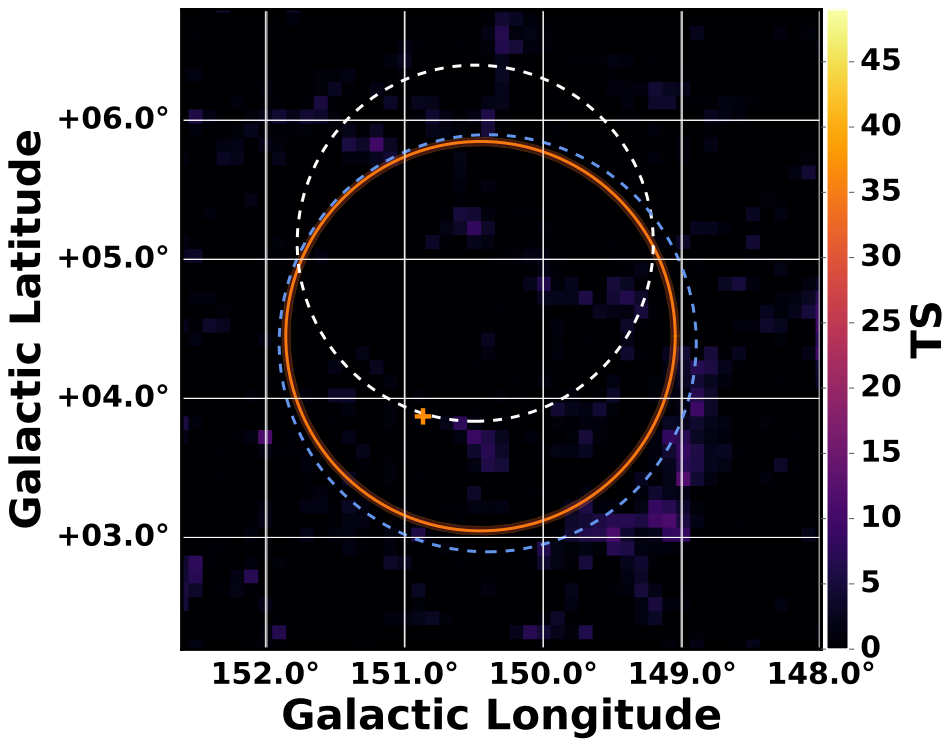
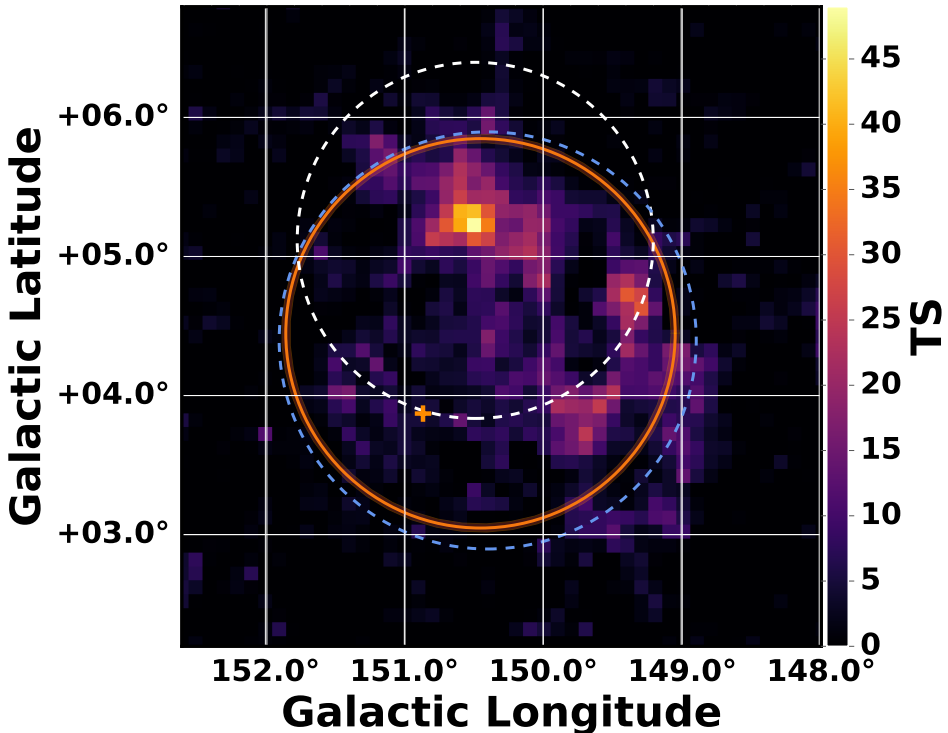


Figure 7.2: Background subtracted residual TS map above 1 GeV with $0.1^\circ \times 0.1^\circ$ pixels, centered on SNR G150.3+4.5. The orange circle and translucent shading show the fit disk radius and 1σ errors, respectively, for the extended source, the orange cross shows the position of 3FGL J0426.7+5437 (included in the background model), blue dashed circle is the extent of the radio SNR, and white dashed circle depicts 2FHL J0431.2+5553e. Bottom map includes G150.3+4.5 in the background model, top does not.

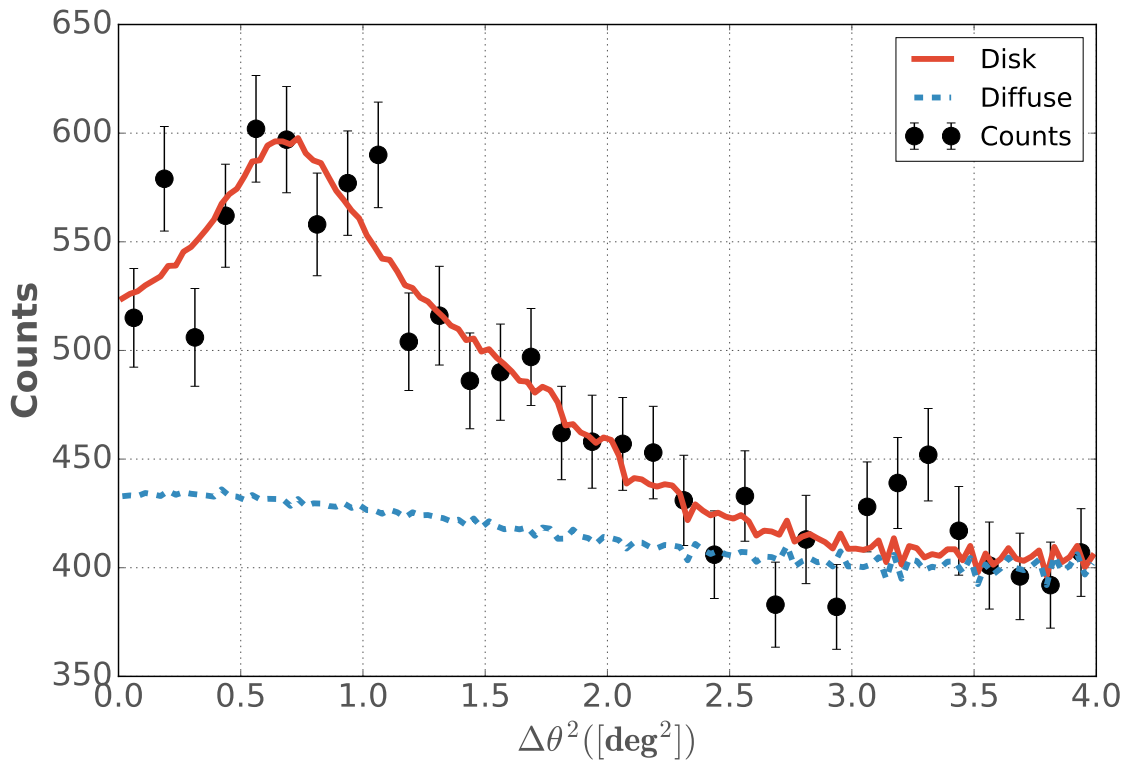


Figure 7.3: Radially integrated counts map centered on the GeV emission coincident with G150.3+4.5. Red line shows the expected counts for a uniform intensity disk with radius, $\sigma = 1.40^\circ$, blue line is that of the Galactic diffuse background.

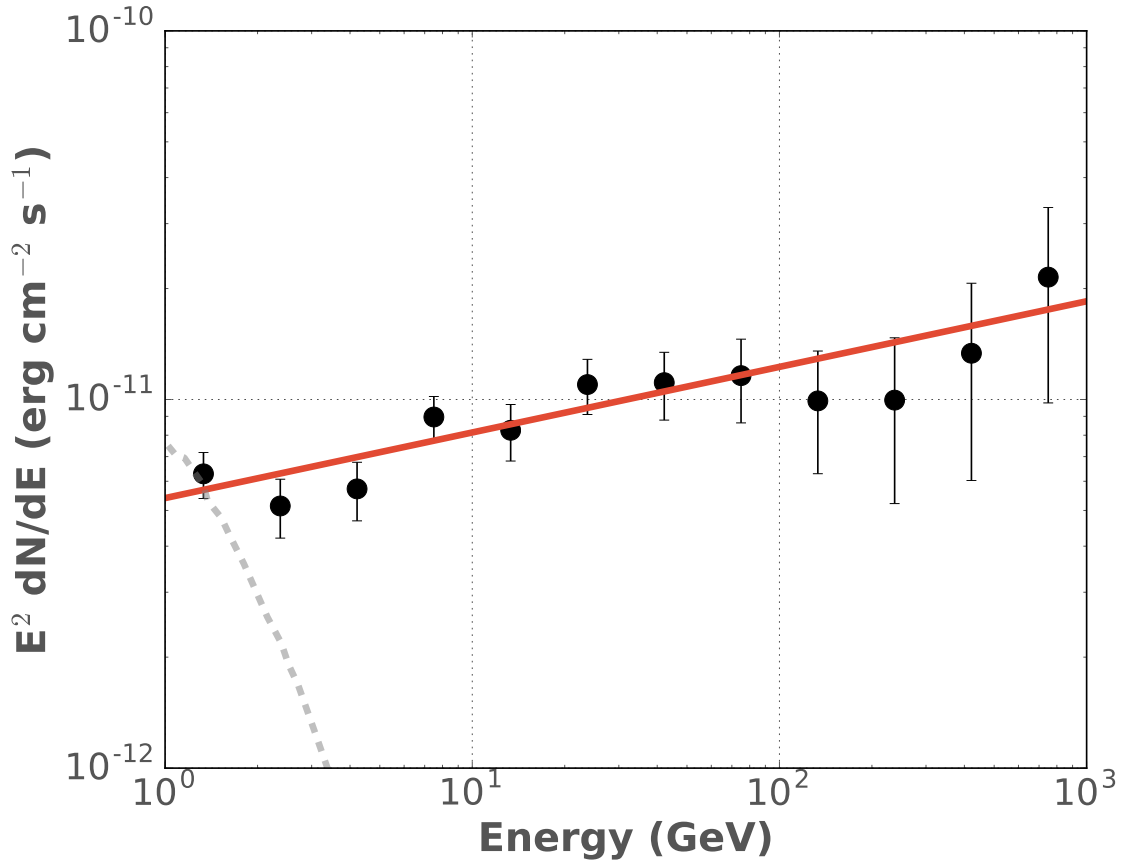


Figure 7.4: Spectral energy distribution for the extended source coincident with SNR G150.3+4.5 from 1 GeV to 1 TeV. Red line corresponds to the best-fit power law model. Points are shown with statistical error bars. Grey dashed line is the SED of 3FGL J0426.7+5437, modeled with an exponential cut-off power law.

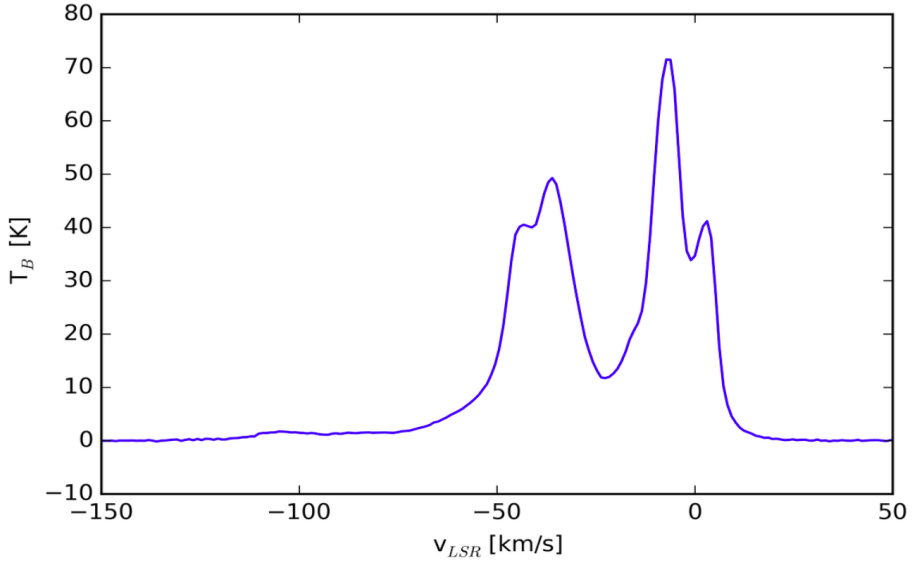


Figure 7.5: G150.3+4.5 HI spectrum.

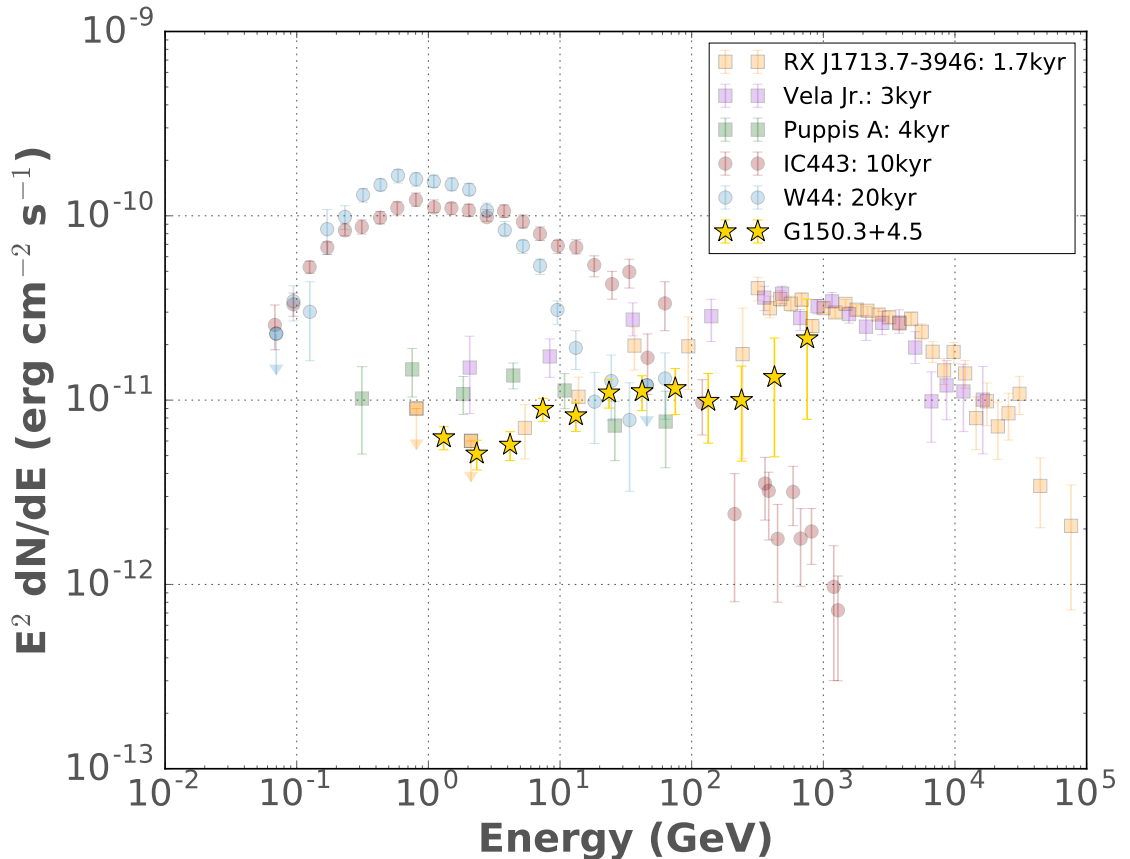


Figure 7.6: SEDs for several LAT observed SNRs with ages spanning $\sim 10^3 - 10^4$ yr. SNRs less than 10 kyr are plotted as squares, older plotted as circles. The GeV spectrum of G150.3+4.5 is shown as stars.

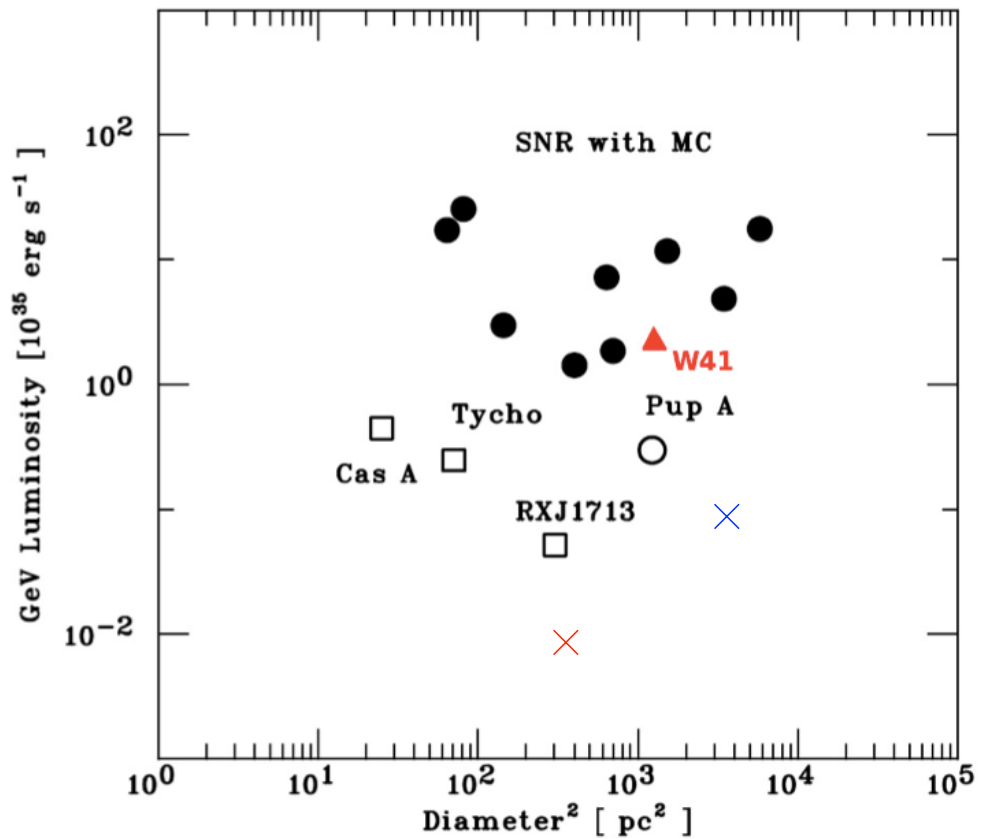


Figure 7.7: Luminosity of several LAT SNRs plotted against their diameter squared. Red cross corresponds to our best HI velocity of 0.38 kpc, blue cross corresponds to the maximal distance assuming a size of 60 pc for the remnant.

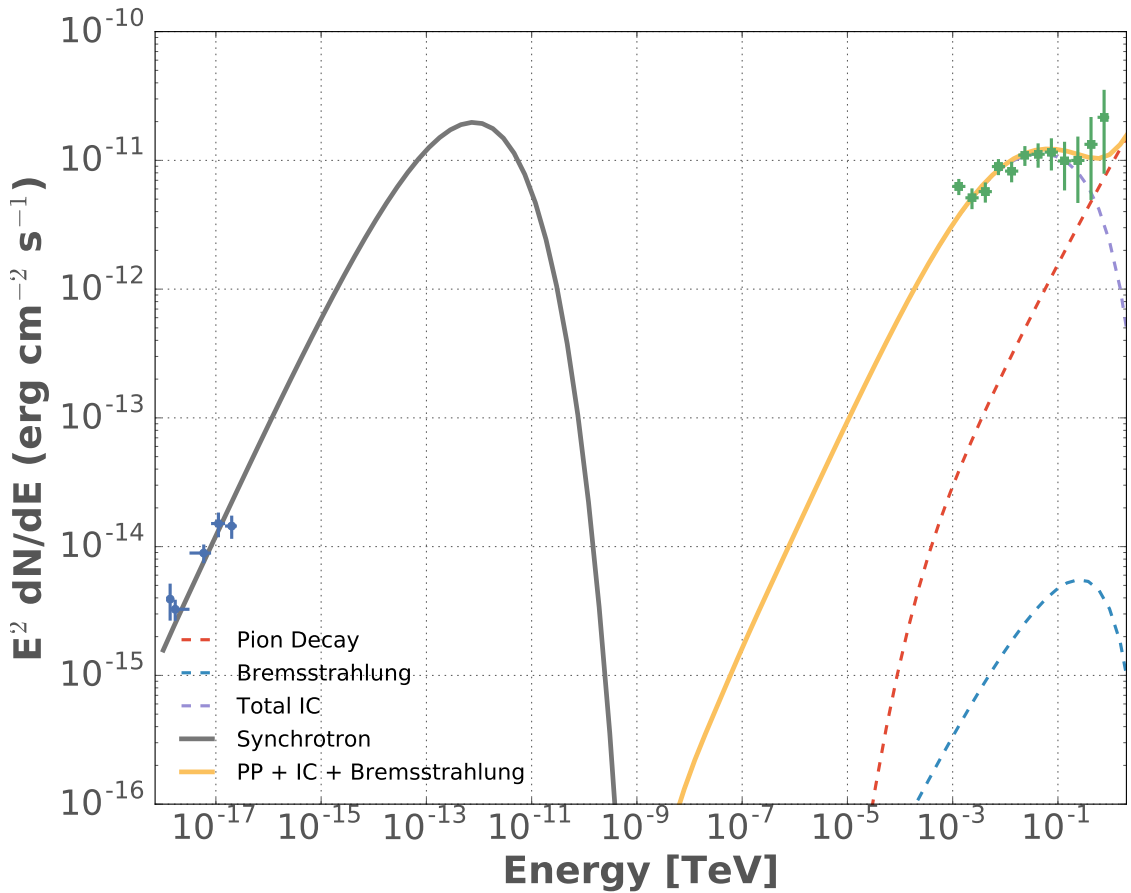


Figure 7.8: Non-thermal emission model for G150.3+4.5.

List of Symbols and Acronyms

2FGL Second *Fermi*-LAT source catalog.

2FHL Second Catalog of Hard *Fermi*-LAT Sources.

2PC Second *Fermi*-LAT catalog of Gamma-ray Pulsars.

3FGL Third *Fermi*-LAT source catalog.

ACD anti-coincidence detector.

AGN active galactic nuclei.

CAL Calorimeter.

CGRO Compton Gamma-Ray Observatory.

CMB Cosmic Microwave Background.

CR cosmic ray.

DSA diffusive shock acceleration.

EGRET Energetic Gamma-Ray Experiment Telescope.

FIR far infrared.

FoV field of view.

GBM Gamma-Ray Burst Monitor.

H.E.S.S. the High Energy Stereoscopic System.

HEP highest-energy photon.

IACT Imaging Air Cherenkov Telescopes.

IC inverse Compton.

IEM interstellar emission model.

IRFs instrument response functions.

ISM interstellar medium.

LAT Large Area Telescope.

LRT likelihood ratio test.

MAGIC the Major Atmospheric Gamma-ray Imaging Cherenkov telescopes.

MC molecular cloud.

NIR near infrared.

PL power law.

PSF point spread function.

PWN pulsar wind nebula.

RoI region of interest.

SED spectral energy distribution.

SNR supernova remnant.

SNRcat First *Fermi*-LAT Supernova Remnant Catalog.

ST Sedov-Taylor.

TKR tracker.

TS test statistic.

VERITAS the Very Energetic Radiation Imaging Telescope Array System.

VHE very high energy.

Bibliography

- Abdo, A. A. 2009, ArXiv:0902.1340, arXiv:0902.1340:0902.1340
- Abdo, A. A., Ackermann, M., Ajello, M., et al. 2009, Science, 325, 840
- . 2010a, ApJS, 188, 405
- . 2010b, ApJ, 708, 1254
- . 2010c, ApJ, 722, 1303
- . 2010d, Science, 327, 1103
- . 2011, ApJ, 734, 28
- Abdo, A. A., Ajello, M., Allafort, A., et al. 2013, ApJS, 208, 17
- Abramowski, A., Acero, F., Aharonian, F., et al. 2011a, A&A, 533, A103
- . 2011b, A&A, 525, A46
- Abramowski, A., Aharonian, F., Ait Benkhali, F., et al. 2015a, A&A, 574, A27
- . 2015b, A&A, 574, A27
- Acero, F., Lemoine-Goumard, M., Renaud, M., et al. 2015a, A&A, 580, A74
- Acero, F., Aharonian, F., Akhperjanian, A. G., et al. 2011, A&A, 525, A45
- Acero, F., Ackermann, M., Ajello, M., et al. 2013, ApJ, 773, 77
- . 2015b, ApJS, 218, 23
- . 2016, ApJS, 224, 8
- Ackermann, M., Ajello, M., Allafort, A., et al. 2011, Science, 334, 1103
- . 2012a, ApJ, 753, 83

- . 2012b, A&A, 538, A71
- Ackermann, M., Ajello, M., Albert, A., et al. 2012c, ApJS, 203, 4
- Ackermann, M., Ajello, M., Allafort, A., et al. 2013a, Science, 339, 807
- Ackermann, M., Ajello, M., Albert, A., et al. 2013b, ApJ, 771, 57
- Ackermann, M., Ajello, M., Allafort, A., et al. 2013c, ApJS, 209, 34
- Ackermann, M., Albert, A., Atwood, W. B., et al. 2014, ApJ, 793, 64
- Ackermann, M., Ajello, M., Atwood, W. B., et al. 2016, ApJS, 222, 5
- Aharonian, F., Akhperjanian, A. G., Bazer-Bachi, A. R., et al. 2006a, A&A, 456, 245
- . 2006b, ApJ, 636, 777
- Aharonian, F., Akhperjanian, A. G., Barres de Almeida, U., et al. 2008a, A&A, 483, 509
- . 2008b, A&A, 488, 219
- . 2008c, A&A, 477, 353
- . 2008d, A&A, 477, 353
- Aharonian, F., Akhperjanian, A. G., de Almeida, U. B., et al. 2009, ApJ, 692, 1500
- Aharonian, F. A., & Atoyan, A. M. 1996, A&A, 309, 917
- . 2000, A&A, 362, 937
- Aharonian, F. A., Akhperjanian, A. G., Aye, K.-M., et al. 2004, Nature, 432, 75
- Ajello, M., Baldini, L., Barbiellini, G., et al. 2016, ApJ, 819, 98
- Alfvén, H., & Herlofson, N. 1950, Physical Review, 78, 616
- Arzoumanian, Z., Gotthelf, E. V., Ransom, S. M., et al. 2011, ApJ, 739, 39
- Atwood, W., Albert, A., Baldini, L., et al. 2013a, ArXiv:1303.3514, arXiv:1303.3514
- Atwood, W. B., Abdo, A. A., Ackermann, M., et al. 2009, ApJ, 697, 1071
- Atwood, W. B., Baldini, L., Bregeon, J., et al. 2013b, ApJ, 774, 76
- Baade, W., & Zwicky, F. 1934, Physical Review, 46, 76

- Badenes, C., Maoz, D., & Draine, B. T. 2010, MNRAS, 407, 1301
- Bamba, A., Ueno, M., Koyama, K., & Yamauchi, S. 2001, PASJ, 53, L21
- Barr, E. D., Guillemot, L., Champion, D. J., et al. 2013, MNRAS, 429, 1633
- Becker, R. H., Markert, T., & Donahue, M. 1985, ApJ, 296, 461
- Bell, A. R. 1978, MNRAS, 182, 147
- Beringer, J., Arguin, J.-F., Barnett, R. M., et al. 2012, Phys. Rev. D, 86, 010001
- Blair, W. P., Sankrit, R., Torres, S. I., Chayer, P., & Danforth, C. W. 2009, ApJ, 692, 335
- Blandford, R. D., & Ostriker, J. P. 1978, ApJ, 221, L29
- Blasi, P. 2013, A&A Rev., 21, 70
- Blumenthal, G. R., & Gould, R. J. 1970, Reviews of Modern Physics, 42, 237
- Boumis, P., Alikakos, J., Christopoulou, P. E., et al. 2008, A&A, 481, 705
- Brogan, C. L., Gelfand, J. D., Gaensler, B. M., Kassim, N. E., & Lazio, T. J. W. 2006, ApJ, 639, L25
- Brogan, C. L., & Troland, T. H. 2001, ApJ, 550, 799
- Bruel, P., & Fermi-LAT Collaboration. 2012, Journal of Physics Conference Series, 404, 012033
- Byun, D.-Y., Koo, B.-C., Tatematsu, K., & Sunada, K. 2006, ApJ, 637, 283
- Camilo, F., Kaspi, V. M., Lyne, A. G., et al. 2000, ApJ, 541, 367
- Camilo, F., Ng, C.-Y., Gaensler, B. M., et al. 2009a, ApJ, 703, L55
- Camilo, F., Ransom, S. M., Gaensler, B. M., & Lorimer, D. R. 2009b, ApJ, 700, L34
- Camilo, F., Ransom, S. M., Gaensler, B. M., et al. 2006, ApJ, 637, 456
- Caraveo, P. A., De Luca, A., Mignani, R. P., & Bignami, G. F. 2001, ApJ, 561, 930
- Carrigan, S., Brun, F., Chaves, R. C. G., et al. 2013, ArXiv:1307.4868, arXiv:1307.4868

- Cash, W. 1979, *ApJ*, 228, 939
- Castelletti, G., Supan, L., Dubner, G., Joshi, B. C., & Surnis, M. P. 2013, *A&A*, 557, L15
- Caswell, J. L. 1985, *AJ*, 90, 1224
- Caswell, J. L., McClure-Griffiths, N. M., & Cheung, M. C. M. 2004, *MNRAS*, 352, 1405
- Caswell, J. L., Murray, J. D., Roger, R. S., Cole, D. J., & Cooke, D. J. 1975, *A&A*, 45, 239
- Chatterjee, S., Vlemmings, W. H. T., Brisken, W. F., et al. 2005, *ApJ*, 630, L61
- Chatterjee, S., Brisken, W. F., Vlemmings, W. H. T., et al. 2009, *ApJ*, 698, 250
- Chevalier, R. A. 1974, *ApJ*, 188, 501
- . 1982, *ApJ*, 258, 790
- Combi, J. A., Albacete Colombo, J. F., Romero, G. E., & Benaglia, P. 2006, *ApJ*, 653, L41
- Combi, J. A., Benaglia, P., Romero, G. E., & Sugizaki, M. 2005, *A&A*, 431, L9
- Condon, J. J., Cotton, W. D., Greisen, E. W., et al. 1998, *AJ*, 115, 1693
- Dermer, C. D. 1986, *A&A*, 157, 223
- Dermer, C. D., Finke, J. D., Murphy, R. J., et al. 2013, ArXiv e-prints, arXiv:1303.6482
- Dodson, R., Legge, D., Reynolds, J. E., & McCulloch, P. M. 2003, *ApJ*, 596, 1137
- Domainko, W., & Ohm, S. 2012, *A&A*, 545, A94
- Dubner, G. M., & Arnal, E. M. 1988, *A&AS*, 75, 363
- Eger, P., Rowell, G., Kawamura, A., et al. 2011, *A&A*, 526, A82
- Esposito, J. A., Hunter, S. D., Kanbach, G., & Sreekumar, P. 1996, *ApJ*, 461, 820
- Federici, S., Pohl, M., Telezhinsky, I., Wilhelm, A., & Dwarkadas, V. V. 2015, *A&A*, 577, A12

- Fermi, E. 1949, Physical Review, 75, 1169
- Ferrand, G., & Safi-Harb, S. 2012, Advances in Space Research, 49, 1313
- Fesen, R. A., Blair, W. P., & Kirshner, R. P. 1985, ApJ, 292, 29
- Foreman-Mackey, D., Hogg, D. W., Lang, D., & Goodman, J. 2013, PASP, 125, 306
- Frail, D. A., & Clifton, T. R. 1989, ApJ, 336, 854
- Frail, D. A., Goss, W. M., Reynoso, E. M., et al. 1996, AJ, 111, 1651
- Funk, S., Reimer, O., Torres, D. F., & Hinton, J. A. 2008, ApJ, 679, 1299
- Gabici, S., Aharonian, F. A., & Casanova, S. 2009, MNRAS, 396, 1629
- Gaensler, B. M., Brazier, K. T. S., Manchester, R. N., Johnston, S., & Green, A. J. 1999, MNRAS, 305, 724
- Gaensler, B. M., Fogel, J. K. J., Slane, P. O., et al. 2003, ApJ, 594, L35
- Gaensler, B. M., & Slane, P. O. 2006, ARA&A, 44, 17
- Gaensler, B. M., & Wallace, B. J. 2003, ApJ, 594, 326
- Gaensler, B. M., Tanna, A., Slane, P. O., et al. 2008, ApJ, 680, L37
- Gaisser, T. K. 1990, Cosmic rays and particle physics
- Gao, X. Y., & Han, J. L. 2014, A&A, 567, A59
- Gerardy, C. L., & Fesen, R. A. 2007, MNRAS, 376, 929
- Gerbrandt, S., Foster, T. J., Kothes, R., Geisbüsch, J., & Tung, A. 2014, A&A, 566, A76
- Giacani, E., Smith, M. J. S., Dubner, G., & Loiseau, N. 2011, A&A, 531, A138
- Giacani, E., Smith, M. J. S., Dubner, G., et al. 2009, A&A, 507, 841
- Giacani, E. B., Dubner, G. M., Green, A. J., Goss, W. M., & Gaensler, B. M. 2000, AJ, 119, 281
- Ginzburg, V. L., & Syrovatskii, S. I. 1964, The Origin of Cosmic Rays
- Górski, K. M., Hivon, E., Banday, A. J., et al. 2005, ApJ, 622, 759
- Gotthelf, E. V., & Halpern, J. P. 2008, ApJ, 681, 515

- Green, D. A. 2004, Bulletin of the Astronomical Society of India, 32, 335
- . 2009, Bulletin of the Astronomical Society of India, 37, 45
- Green, D. A. 2012, in American Institute of Physics Conference Series, Vol. 1505, American Institute of Physics Conference Series, ed. F. A. Aharonian, W. Hofmann, & F. M. Rieger, 5–12
- . 2014, Bulletin of the Astronomical Society of India, 42, 47
- Green, D. A., Gull, S. F., Tan, S. M., & Simon, A. J. B. 1988, MNRAS, 231, 735
- Grondin, M.-H., Funk, S., Lemoine-Goumard, M., et al. 2011, ApJ, 738, 42
- Hailey, C. J., & Craig, W. W. 1994, ApJ, 434, 635
- Halpern, J. P., Gotthelf, E. V., & Camilo, F. 2012, ApJ, 753, L14
- Hanabata, Y., Katagiri, H., Hewitt, J. W., et al. 2014, ApJ, 786, 145
- Harrus, I. M., Hughes, J. P., & Slane, P. O. 1998, ApJ, 499, 273
- Hartman, R. C., Bertsch, D. L., Bloom, S. D., et al. 1999, ApJS, 123, 79
- Haug, E. 1975, Zeitschrift Naturforschung Teil A, 30, 1099
- Hayakawa, S. 1969, Cosmic ray physics. Nuclear and astrophysical aspects
- Hayato, A., Yamaguchi, H., Tamagawa, T., et al. 2010, ApJ, 725, 894
- Helene, O. 1983, Nuclear Instruments and Methods in Physics Research, 212, 319
- Hess, V. F. 1912, Physikalische Zeitschrift, 13, 1084
- Hewitt, J. W., & Fermi-LAT Collaboration. 2015, in American Astronomical Society Meeting Abstracts, Vol. 225, American Astronomical Society Meeting Abstracts, 140.31
- Hewitt, J. W., & Lemoine-Goumard, M. 2015, Comptes Rendus Physique, 16, 674
- Hewitt, J. W., Rho, J., Andersen, M., & Reach, W. T. 2009a, ApJ, 694, 1266
- Hewitt, J. W., & Yusef-Zadeh, F. 2009, ApJ, 694, L16
- Hewitt, J. W., Yusef-Zadeh, F., & Wardle, M. 2008, ApJ, 683, 189
- . 2009b, ApJ, 706, L270

- Hewitt, J. W., Yusef-Zadeh, F., Wardle, M., Roberts, D. A., & Kassim, N. E. 2006,
ApJ, 652, 1288
- Hillier, R. 1984, Gamma ray astronomy
- Hinton, J. 2004, New Astron.Rev., 48, 331
- Hofverberg, P., Chaves, R. C. G., Fiasson, A., et al. 2010, in 25th Texas Symposium
on Relativistic Astrophysics, 196
- Holder, J., Acciari, V., Aliu, E., et al. 2009, AIP Conf.Proc., 1085, 657
- Hörandel, J. R. 2008, Advances in Space Research, 41, 442
- Houck, J. C., & Allen, G. E. 2006, ApJS, 167, 26
- Inoue, T., Yamazaki, R., & Inutsuka, S.-i. 2010, ApJ, 723, L108
- James, F., & Roos, M. 1975, Computer Physics Communications, 10, 343
- Jiang, B., Chen, Y., Wang, J., et al. 2010, ApJ, 712, 1147
- Jogler, T., & Funk, S. 2016, ApJ, 816, 100
- Johanson, A. K., & Kerton, C. R. 2009, AJ, 138, 1615
- Junkes, N., Fuerst, E., & Reich, W. 1992, A&AS, 96, 1
- Kassim, N. E., Hertz, P., & Weiler, K. W. 1993, ApJ, 419, 733
- Kassim, N. E., & Weiler, K. W. 1990, Nature, 343, 146
- Katsuda, S., Tsunemi, H., & Mori, K. 2008, ApJ, 678, L35
- Kerr, F. J., & Lynden-Bell, D. 1986, MNRAS, 221, 1023
- Kerr, M. 2010, PhD thesis, University of Washington, arXiv:1101.6072
- Kiepenheuer, K. O. 1950, Physical Review, 79, 738
- Kim, I.-J., Min, K.-W., Seon, K.-I., Han, W., & Edelstein, J. 2010, ApJ, 709, 823
- Koch, H. W., & Motz, J. W. 1959, Reviews of Modern Physics, 31, 920
- Koo, B.-C., & Moon, D.-S. 1997, ApJ, 475, 194
- Koralesky, B., Frail, D. A., Goss, W. M., Claussen, M. J., & Green, A. J. 1998, AJ,
116, 1323

- Kothes, R., & Foster, T. 2012, ApJ, 746, L4
- Kothes, R., Reich, W., Foster, T., & Byun, D.-Y. 2003, ApJ, 588, 852
- Kothes, R., Uyaniker, B., & Pineault, S. 2001, ApJ, 560, 236
- Koyama, K., Petre, R., Gotthelf, E. V., et al. 1995, Nature, 378, 255
- Krause, O., Tanaka, M., Usuda, T., et al. 2008, Nature, 456, 617
- Ladouceur, Y., & Pineault, S. 2008, A&A, 490, 197
- Lande, J., Ackermann, M., Allafort, A., et al. 2012, ApJ, 756, 5
- Landecker, T. L., Pineault, S., Routledge, D., & Vaneldik, J. F. 1989, MNRAS, 237, 277
- Lang, C. C., Goss, W. M., Cyganowski, C., & Clubb, K. I. 2010, ApJS, 191, 275
- Lazendic, J. S., Wardle, M., Burton, M. G., et al. 2004, MNRAS, 354, 393
- Leahy, D., Green, K., & Tian, W. 2014, MNRAS, 438, 1813
- Leahy, D., & Tian, W. 2006, A&A, 451, 251
- Leahy, D. A., Green, K., & Ranasinghe, S. 2013, MNRAS, 436, 968
- Leahy, D. A., & Ranasinghe, S. 2012, MNRAS, 423, 718
- Leahy, D. A., & Roger, R. S. 1991, AJ, 101, 1033
- Leahy, D. A., Tian, W., & Wang, Q. D. 2008, AJ, 136, 1477
- Leahy, D. A., & Tian, W. W. 2007, A&A, 461, 1013
- . 2008a, A&A, 480, L25
- . 2008b, AJ, 135, 167
- Lemiere, A., Slane, P., Gaensler, B. M., & Murray, S. 2009, ApJ, 706, 1269
- Lemoine-Goumard, M., Renaud, M., Vink, J., et al. 2012, A&A, 545, A28
- Lemoine-Goumard, M., Zavlin, V. E., Grondin, M.-H., et al. 2011, A&A, 533, A102
- Longair, M. S. 2011, High Energy Astrophysics
- Lopez, L. A., Ramirez-Ruiz, E., Huppenkothen, D., Badenes, C., & Pooley, D. A. 2011, ApJ, 732, 114

- Lorenz, E. 2004, New Astron.Rev., 48, 339
- Lozinskaya, T. A., Sitnik, T. G., & Pravdikova, V. V. 1993, Astronomy Reports, 37, 240
- Malkov, M. A., Diamond, P. H., & Sagdeev, R. Z. 2011, Nature Communications, 2, 194
- Malkov, M. A., & Drury, L. O. 2001, Reports on Progress in Physics, 64, 429
- Massaro, E., Perri, M., Giommi, P., & Nesci, R. 2004, A&A, 413, 489
- Mattox, J. R., Bertsch, D. L., Chiang, J., et al. 1996, ApJ, 461, 396
- McClure-Griffiths, N. M., Green, A. J., Dickey, J. M., et al. 2001, ApJ, 551, 394
- Misanovic, Z., Kargaltsev, O., & Pavlov, G. G. 2010, ApJ, 725, 931
- Moiseev, A. A., Hartman, R. C., Johnson, T. E., Ormes, J. F., & Thompson, D. J. 2005, International Cosmic Ray Conference, 5, 419
- Moriguchi, Y., Tamura, K., Tawara, Y., et al. 2005, ApJ, 631, 947
- Moriguchi, Y., Yamaguchi, N., Onishi, T., Mizuno, A., & Fukui, Y. 2001, PASJ, 53, 1025
- Ng, C.-Y., Romani, R. W., Brisken, W. F., Chatterjee, S., & Kramer, M. 2007, ApJ, 654, 487
- Nikolić, S., van de Ven, G., Heng, K., et al. 2013, Science, 340, 45
- Nolan, P. L., Abdo, A. A., Ackermann, M., et al. 2012, ApJS, 199, 31
- Odegard, N. 1986, ApJ, 301, 813
- Ohira, Y., Murase, K., & Yamazaki, R. 2011, MNRAS, 410, 1577
- Ong, R. A. 2013, ArXiv:1307.5003, arXiv:1307.5003
- Pacholczyk, A. G. 1970, Radio astrophysics. Nonthermal processes in galactic and extragalactic sources
- Paron, S., Dubner, G., Reynoso, E., & Rubio, M. 2008, A&A, 480, 439
- Paron, S., Ortega, M. E., Rubio, M., & Dubner, G. 2009, A&A, 498, 445

- Paron, S. A., Reynoso, E. M., Purcell, C., Dubner, G. M., & Green, A. 2006, PASA, 23, 69
- Pauls, T. 1977, A&A, 59, L13
- Pfeffermann, E., Aschenbach, B., & Predehl, P. 1991, A&A, 246, L28
- Pineault, S., Landecker, T. L., Madore, B., & Gaumont-Guay, S. 1993, AJ, 105, 1060
- Prinz, T., & Becker, W. 2012, A&A, 544, A7
- Radhakrishnan, V., Goss, W. M., Murray, J. D., & Brooks, J. W. 1972, ApJS, 24, 49
- Rakowski, C. E., Badenes, C., Gaensler, B. M., et al. 2006, ApJ, 646, 982
- Rakowski, C. E., Hughes, J. P., & Slane, P. 2001, ApJ, 548, 258
- Reed, J. E., Hester, J. J., Fabian, A. C., & Winkler, P. F. 1995, ApJ, 440, 706
- Reid, M. J., Menten, K. M., Brunthaler, A., et al. 2014, ApJ, 783, 130
- Renaud, M., Goret, P., & Chaves, R. C. G. 2008, in American Institute of Physics Conference Series, Vol. 1085, American Institute of Physics Conference Series, ed. F. A. Aharonian, W. Hofmann, & F. Rieger, 281–284
- Reynolds, S. P. 2008, ARA&A, 46, 89
- Reynoso, E. M., & Goss, W. M. 1999, AJ, 118, 926
- Reynoso, E. M., Green, A. J., Johnston, S., et al. 2004, PASA, 21, 82
- Reynoso, E. M., Johnston, S., Green, A. J., & Koribalski, B. S. 2006, MNRAS, 369, 416
- Reynoso, E. M., & Mangum, J. G. 2000, ApJ, 545, 874
- Rho, J., & Petre, R. 1998, ApJ, 503, L167
- Roberts, M. S. E., Romani, R. W., Johnston, S., & Green, A. J. 1999, ApJ, 515, 712
- Romero, G. E., Benaglia, P., & Torres, D. F. 1999, A&A, 348, 868

- Rosado, M., Ambrocio-Cruz, P., Le Coarer, E., & Marcelin, M. 1996a, A&A, 315, 243
- . 1996b, A&A, 315, 243
- Rousseau, R., Grondin, M.-H., Van Etten, A., et al. 2012, A&A, 544, A3
- Routledge, D., Dewdney, P. E., Landecker, T. L., & Vaneldik, J. F. 1991, A&A, 247, 529
- Ruiz, M. T., & May, J. 1986, ApJ, 309, 667
- Rybicki, G. B., & Lightman, A. P. 1986, Radiative Processes in Astrophysics, 400
- Ryle, M., & Smith, F. G. 1948, Nature, 162, 462
- Sallmen, S., & Welsh, B. Y. 2004, A&A, 426, 555
- Sankrit, R., Blair, W. P., Delaney, T., et al. 2005, Advances in Space Research, 35, 1027
- Schwentker, O. 1994, A&A, 286, L47
- Sedov, L. I. 1959, Similarity and Dimensional Methods in Mechanics
- Seward, F. D., Dame, T. M., Fesen, R. A., & Aschenbach, B. 1995, ApJ, 449, 681
- Shklovskii, I. S. 1953, Radioastronomiia.
- Slane, P., Smith, R. K., Hughes, J. P., & Petre, R. 2002, ApJ, 564, 284
- Sollerman, J., Ghavamian, P., Lundqvist, P., & Smith, R. C. 2003a, A&A, 407, 249
- . 2003b, A&A, 407, 249
- Stecker, F. W. 1971, NASA Special Publication, 249
- Stewart, R. T., Caswell, J. L., Haynes, R. F., & Nelson, G. J. 1993, MNRAS, 261, 593
- Stupar, M., Parker, Q. A., & Filipović, M. D. 2007, MNRAS, 374, 1441
- Sturner, S. J., & Dermer, C. D. 1995, A&A, 293, astro-ph/9409047
- Su, M., Slatyer, T. R., & Finkbeiner, D. P. 2010, ApJ, 724, 1044
- Su, Y., Chen, Y., Yang, J., et al. 2011, ApJ, 727, 43

- Sun, M., Wang, Z.-r., & Chen, Y. 1999, *ApJ*, 511, 274
- Sun, X. H., Reich, P., Reich, W., et al. 2011, *A&A*, 536, A83
- Tam, P. H. T., Wagner, S. J., Tibolla, O., & Chaves, R. C. G. 2010, *A&A*, 518, A8
- Tanimori, T., Hayami, Y., Kamei, S., et al. 1998, *ApJ*, 497, L25
- Taylor, G. 1950a, *Proceedings of the Royal Society of London Series A*, 201, 159
- . 1950b, *Royal Society of London Proceedings Series A*, 201, 159
- Thompson, D. J., Baldini, L., & Uchiyama, Y. 2012, *Astroparticle Physics*, 39, 22
- Thompson, D. J., Bertsch, D. L., Fichtel, C. E., et al. 1993, *ApJS*, 86, 629
- Tian, W. W., Havercorn, M., & Zhang, H. Y. 2007a, *MNRAS*, 378, 1283
- Tian, W. W., & Leahy, D. A. 2008a, *ApJ*, 677, 292
- . 2008b, *MNRAS*, 391, L54
- . 2011, *ApJ*, 729, L15
- . 2012, *MNRAS*, 421, 2593
- . 2013, *ApJ*, 769, L17
- . 2014, *ApJ*, 783, L2
- Tian, W. W., Leahy, D. A., Havercorn, M., & Jiang, B. 2008, *ApJ*, 679, L85
- Tian, W. W., Leahy, D. A., & Wang, Q. D. 2007b, *A&A*, 474, 541
- Tian, W. W., Li, Z., Leahy, D. A., & Wang, Q. D. 2007c, *ApJ*, 657, L25
- Tibolla, O. 2009, in *American Institute of Physics Conference Series*, Vol. 1112, American Institute of Physics Conference Series, ed. D. Bastieri & R. Rando, 211–222
- Torres, D. F., Romero, G. E., Dame, T. M., Combi, J. A., & Butt, Y. M. 2003, *Phys. Rep.*, 382, 303
- Trimble, V. 1973, *PASP*, 85, 579
- Truelove, J. K., & McKee, C. F. 1999, *ApJS*, 120, 299
- Uchiyama, Y., Blandford, R. D., Funk, S., Tajima, H., & Tanaka, T. 2010, *ApJ*,

723, L122

- Uchiyama, Y., Funk, S., Katagiri, H., et al. 2012, *ApJ*, 749, L35
- Urošević, D. 2014, *Ap&SS*, 354, 541
- Velázquez, P. F., Dubner, G. M., Goss, W. M., & Green, A. J. 2002, *AJ*, 124, 2145
- Vink, J. 2004, *ApJ*, 604, 693
- . 2012, *A&A Rev.*, 20, 49
- Voges, W., Aschenbach, B., Boller, T., et al. 1999, *A&A*, 349, 389
- Walker, A. J., & Zealey, W. J. 2001, *MNRAS*, 325, 287
- Welsh, B. Y., Sallmen, S., Jelinsky, S., & Lallement, R. 2003, *A&A*, 403, 605
- Woltjer, L. 1972, *ARA&A*, 10, 129
- Wootten, A. 1981, *ApJ*, 245, 105
- Wootten, H. A. 1977, *ApJ*, 216, 440
- Xiao, L., & Zhu, M. 2012, *A&A*, 545, A86
- Xilouris, K. M., Papamastorakis, J., Paleologou, E. V., Andredakis, Y., & Haerendel, G. 1993, *A&A*, 270, 393
- Xu, Y., Reid, M. J., Zheng, X. W., & Menten, K. M. 2006, *Science*, 311, 54
- Yamaguchi, H., Ueno, M., Koyama, K., Bamba, A., & Yamauchi, S. 2004, *PASJ*, 56, 1059
- Yar-Uyaniker, A., Uyaniker, B., & Kothes, R. 2004, *ApJ*, 616, 247
- Yusef-Zadeh, F., Goss, W. M., Roberts, D. A., Robinson, B., & Frail, D. A. 1999, *ApJ*, 527, 172
- Yusef-Zadeh, F., Arendt, R. G., Heinke, C. O., et al. 2007, in IAU Symposium, Vol. 242, IAU Symposium, ed. J. M. Chapman & W. A. Baan, 366–373
- Zabalza, V. 2015, ArXiv e-prints, arXiv:1509.03319
- Zhou, P., & Chen, Y. 2011, *ApJ*, 743, 4
- Zhou, X., Chen, Y., Su, Y., & Yang, J. 2009, *ApJ*, 691, 516

Zhu, H., Tian, W. W., Torres, D. F., Pedaletti, G., & Su, H. Q. 2013, ApJ, 775, 95